

Biret

Hubble Space Telescope

Wide Field and Planetary Camera 2

Instrument Handbook

Version 1.0
March 1993

Revision History

Instrument	Version	Date	Editor
WF/PC-1	1.0	October 1985	Richard Griffiths
WF/PC-1	2.0	May 1989	Richard Griffiths
WF/PC-1	2.1	May 1990	Richard Griffiths
WF/PC-1	3.0	April 1992	John W. MacKenty
WFPC2	1.0	March 1993	Christopher J. Burrows

Authors

WFPC2:	Christopher J. Burrows, Mark Clampin, John Krist
WF/PC-1:	John W. MacKenty, Richard E. Griffiths, William B. Sparks, Keith Horne, Roberto Gilmozzi, Shawn P. Ewald, Christine E. Ritchie, Sylvia M. Baggett, Lisa E. Walter, and Glenn Schneider.
WFPC2 IDT:	John T. Trauger, Christopher J. Burrows, John Clarke, David Crisp, John Gallagher, Richard E. Griffiths, J. Jeff Hester, John Hoessel, John Holtzman, Jeremy Mould, and James A. Westphal.

Table of Contents

1. Introduction	1
1.1. Background to the WFPC2	1
1.2. Science Performance	1
1.3. Calibration Plans.....	2
1.4. Major Changes in WFPC2	2
1.4.1. Single Field Format.....	3
1.4.2. Optical Alignment Mechanisms.....	3
1.4.3. CCD Technology.....	4
1.4.4. UV Imaging.....	5
1.4.5. Calibration Channel.....	5
1.4.6. Spectral Elements	5
1.5. Organization of this Handbook.....	6
1.6. References	6
2. Instrument Description.....	7
2.1. Science Objectives	7
2.2. WFPC2 Configuration, Field of View and Resolution	7
2.3. Overall Instrument Description	8
2.4. Shutter.....	12
2.5. Overhead Time	13
2.6. CCD Orientation and Readout	13
3. Optical Filters.....	15
3.1. Linear Ramp Filters.....	19
3.1.1. Spectral Response.....	19
3.2. Redshifted [OII] Quad Filters	25
3.3. Polarizer Quad Filter.....	25
3.4. Methane Quad	27
3.5. Wood's Filters	29
3.6. Apertures.....	30
4. CCD Performance.....	32
4.1. Introduction.....	32
4.2. CCD Characteristics	33
4.2.1. Quantum Efficiency.....	33
4.2.2. Dynamic Range	34
4.2.3. Blooming.....	34
4.2.4. Residual Image.....	35

4.2.5. Quantum Efficiency Hysteresis	35
4.2.6. Flat Field	35
4.2.7. Dark Noise.....	36
4.2.8. Cosmic Rays.....	37
4.2.9. Radiation Damage	38
4.2.10. Charge Transfer Efficiency.....	38
4.2.11. Read Noise and Gain Settings.....	39
4.2.12. CCD Electronics	39
4.3. References	39
5. Point Spread Function.....	40
5.1. Effects of OTA Spherical Aberration.....	40
5.2. Model PSFs	41
5.3. Aberration Correction.....	44
6. Exposure Time Estimation	45
6.1. Preliminary System Throughput	45
6.2. Sky Background.....	49
6.3. Point Sources	49
6.4. Extended Sources.....	50
6.5. Red Leaks in UV Filters	51
7. Calibration and Data Reduction	53
7.1. Calibration Observations and Reference Data	53
7.2. Instrument Calibration.....	53
7.3. Flat Fields	53
7.4. Dark Frames.....	54
7.5. Bias Frames	54
7.6. Data Reduction and Data Products	54
7.7. Pipeline Processing.....	54
7.8. Data Formats	55
8. Appendix.....	56
8.1. Passbands For Each Filter In Isolation	56
8.2. Passbands Including the System Response	65
8.3. Normalized Passbands Including the System Response.....	74

Figures

Figure 1.1	WFPC2 Field of View	3
Figure 2.1	Wide Field Planetary Camera Concept Illustration	8
Figure 2.2	WFPC2 Optical Configuration	9
Figure 2.3	Cooled Sensor Assembly	10
Figure 2.4	WFPC2 + OTA System Throughput.	11
Figure 3.1	Summary of Normalized Filter Curves.....	18
Figure 3.2	Ramp Filter Peak Transmission	19
Figure 3.3	Ramp Filter Dimensionless Widths	20
Figure 3.4	Ramp Filter Wavelength Mapping	24
Figure 3.5	Redshifted [OII] and Polarizer Quads	26
Figure 3.6	Polarizer Transmission	26
Figure 3.7	Methane Quad Filter	28
Figure 3.8	Wood's Filters	29
Figure 4.1	MPP Operating Principle (schematic).....	32
Figure 4.2	WFPC2 Flight CCD DQE.....	34
Figure 4.3	WFPC2 CCD Flat Field.....	36
Figure 4.4	Comparison of PSF and Cosmic Ray Events (schematic).....	38
Figure 5.1	PSF Surface Brightness	40
Figure 5.2	Encircled Energy	41
Figure 6.1	Johnson UBV Regression to WFPC2 Passbands	46
Figure 6.2	Johnson Cousins VRI Regression to WFPC2 Passbands.....	47
Figure 6.3	Giant Elliptical Galaxy	50
Figure 6.4	UV Filter Red Leaks.....	51

Tables

Table 2.1	Summary of Camera Format.....	7
Table 2.2	WFPC2 Dynamic Range in a Single Exposure	12
Table 2.3	Quantized Exposure Times (Seconds).....	13
Table 2.4	Nominal Inner Field Edges.	14
Table 3.1	WFPC2 Simple ('F') Filter Set.....	16
Table 3.2	WFPC2 Quad and Ramp Filters	17
Table 3.3	Ramp Filter FR418N Parameters.....	21
Table 3.4	Ramp Filter FR533N Parameters.....	21
Table 3.5	Ramp Filter FR680N Parameters.....	22
Table 3.6	Ramp Filter FR868N Parameters.....	22
Table 3.7	Aperture Locations and Wavelengths for Ramp Filters.....	23
Table 3.8	Redshifted [OII] Quad Filter Elements.....	25
Table 3.9	Polarizer Quad Filter.....	25
Table 3.10	Methane Band Quad Filter.....	27
Table 3.11	Wood's Filters	30
Table 3.12	Summary of Preliminary Aperture Definitions.....	31
Table 4.1	Comparison Between WF/PC-I and WFPC2 CCDs.....	33
Table 4.2	CCD Dark Count Rates.....	37
Table 4.3	Signal Chain Gains	39
Table 5.1	PC Point Spread Functions	42
Table 5.2	WF Point Spread Functions.....	43
Table 5.3	Wavefront Error Budget	44
Table 6.1	Preliminary System Throughputs	48
Table 6.2	AB As a Function of Spectral Type and Wavelength.....	49
Table 6.3	Sky Brightness.....	49
Table 6.4	Signal to Noise Corrections.....	49
Table 6.5	Red Leak in UV Filters	52

1. INTRODUCTION

1.1. BACKGROUND TO THE WFPC2

The original Wide Field and Planetary Camera (WF/PC-1) is a two-dimensional spectrophotometer with rudimentary polarimetric and transmission-grating capabilities. It images the center of the field of the Hubble Space Telescope (HST). The instrument was designed to operate from 1150Å to 11000Å with a resolution of 0.1 arcseconds per pixel (Wide Field camera, F/12.9) or 0.043 arcseconds per pixel (Planetary Camera, F/30), each camera mode using an array of four 800×800 CCD detectors.

The development and construction of the WF/PC-1 was led by Prof. J. A. Westphal, Principal Investigator (PI), of the California Institute of Technology. The Investigation Definition Team (IDT) also included J. E. Gunn (deputy PI), W. A. Baum, A. D. Code, D. G. Currie, G. E. Danielson, T. F. Kelsall, J. A. Kristian, C. R. Lynds, P. K. Seidelmann, and B. A. Smith. The instrument was built at the Jet Propulsion Laboratory, Caltech (JPL).

NASA decided to build a second Wide Field and Planetary Camera (WFPC2) at JPL as a backup clone of the WF/PC-1 because of its important role in the overall HST mission. This second version of the WF/PC was in the early stages of construction at JPL at the time of HST launch. The Principal Investigator for WFPC2 is Dr J. T. Trauger of JPL. The IDT is C. J. Burrows, J. Clarke, D. Crisp, J. Gallagher, R. E. Griffiths, J. J. Hester, J. Hoessel, J. Holtzman, J. Mould, and J. A. Westphal.

WF/PC-1 was launched aboard the HST in April 1990 and was central to the discovery and characterization of the spherical aberration in HST. The aberration severely compromises the expected capabilities of WF/PC-1. A modification of the internal WF/PC optics can correct for the spherical aberration and restore most of the originally expected performance. As a result, it was decided to incorporate the correction within WFPC2 and to accelerate its development. WF/PC-1 is expected to be replaced by WFPC2 during the first Maintenance and Refurbishment Mission scheduled for December 1993.

In December 1990, the WF/PC-1 detectors were conditioned (UV flood procedure) in preparation for the scientific observing program. During 1991 Science Verification (SV) tests and calibration data were obtained by the IDT concurrent with the Cycle 0 GTO science observations. Starting in mid-1991, GO science observations also became a significant part of the usage of WF/PC-1. The engineering hand-over of the WF/PC-1 from JPL to the STScI was completed in November 1991. Observations for the IDT's SV program were completed in January 1992 and the formal SV Report delivered in February 1992. The ongoing STScI calibration program began during the fall of 1991.

With the commencement of Cycle 4 observations, the General Observer community will have access to WFPC2. WFPC2 is a wide-field photometric camera which covers the spectrum from 1150 to 11000Å. As well as optical correction for the aberrated HST primary mirror, the WFPC2 incorporates evolutionary improvements in photometric imaging capabilities. The CCD sensors, signal chain electronics, filter set, UV performance, internal calibrations, and operational efficiency have all been improved through new technologies and lessons learned from WF/PC-1 operations and the HST experience since launch.

1.2. SCIENCE PERFORMANCE

The WFPC2 is now in the final stages of assembly and will be completed before the system level thermal vacuum (SLTV) testing at JPL in April and May 1993. Between

June and November there will be payload compatibility checks at Goddard Space Flight Center (GSFC), and payload integration at Kennedy space center (KSC). We can predict with some confidence that the WFPC2 will meet its engineering performance requirements on the basis of component and sub-assembly tests to date. Formally, these instrument performance requirements are set forth in a document called the Contract End Item Specification (CEIS). In brief, the WFPC2 CEIS calls for accurate correction of the HST spherical aberration, a scientifically capable camera configured for reliable operation in space without maintenance, an instrument which can be calibrated and maintained without excessive operational overhead, and comprehensive ground testing and generation of a viable calibration database prior to instrument delivery. The WFPC2 has the same scientific goals as WF/PC-1, hence the WF/PC-1 and WFPC2 instrument specifications are substantially similar.

In evaluating the science performance of WFPC2 we consider not only its basic capabilities, but also the ability of the instrument to meet performance requirements in normal day-to-day operations. The years of experience with WF/PC-1, both in laboratory testing and in science operations on-orbit, have given us insights into the practical aspects of operating a CCD camera in the HST environment, and have allowed us to improve science capabilities and efficiency in many areas.

Observers are cautioned that this manual was written before the system level testing. Therefore all calibrations and performance projections, while necessary for planning observations, must be regarded as preliminary.

1.3. CALIBRATION PLANS

WFPC2 science verification requirements are being developed by the science team, GSFC, and the STScI to include: verification of the baseline instrument performance; an optical adjustment by focussing and aligning to minimize coma; the estimation of residual wavefront errors from the analysis of star images; a photometric calibration with a core minimum set of filters (including both visible and UV wavelengths, and consistent with anticipated early science observation requirements); the evaluation of photometric accuracy over the full field with the core minimum filter set; and measurement of the photometric stability.

Following the early alignment and calibrations, further instrument calibration will be interspersed with science observations. Calibrations of new modes and filters will be coordinated with GTO and GO science program planning. Initial calibrations of new filters will be merged into the routine STScI maintenance and calibration time to support an increasing diversity of science programs. We expect that the nominal 10% of spacecraft time devoted to instrument maintenance and calibration will be increased in cycle 4 following the servicing mission, in order to accommodate the timely calibration of all the WFPC2 filters that are used in scientific observations.

1.4. MAJOR CHANGES IN WFPC2

The WFPC2 objectives are to allow us to recover HST's expected wide field imaging capabilities with the first HST servicing mission and to build on the WF/PC-1 experience to provide improved science capability and operational efficiency while employing the flight proven WF/PC-1 design. As a result, although substantially similar, WFPC2 differs from WF/PC-1 in several important respects. The following subsections outline these differences. There is a full description of the instrument in Chapter 2.

1.4.1. Single Field Format

A reduction in scope of the WFPC2 instrument was mandated in August 1991 due to budget and schedule constraints. The result was a reduction in the number of relay channels and CCDs. The WFPC2 field of view is now divided and distributed into four cameras by a fixed four-faceted pyramid mirror near the HST focal plane. Three of these are F/12.9 Wide Field cameras (WF), and the remaining one is an F/28.3 Planetary camera (PC). There are thus four sets of relay optics and CCD sensors in WFPC2, rather than the eight in WF/PC-1, which has two independent field formats. The pyramid rotation mechanism has been eliminated, and all four cameras are now in locations occupied in WF/PC-1 by the wide field camera relays. These positions are denoted PC1, WF2, WF3, and WF4, and the projection of their fields of view onto the sky is illustrated in Figure 1.1. Each image is a mosaic of three F/12.9 images and one F/28.3 image.

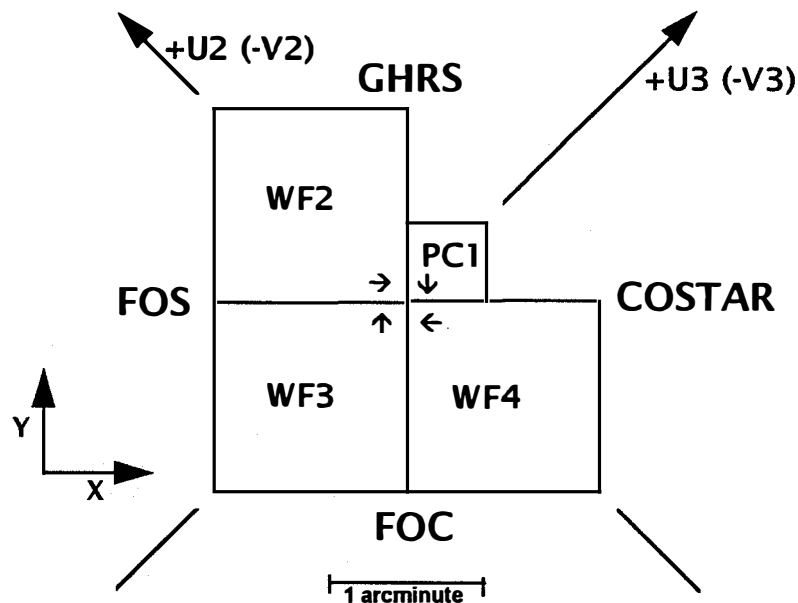


Figure 1.1 WFPC2 Field of View on the sky. The readout direction is marked with arrows near the start of the first row in each CCD. The XY coordinate directions are for POSTARG commands.

1.4.2. Optical Alignment Mechanisms

Two entirely new mechanism types have been introduced in WFPC2 to allow optical alignment on-orbit. The 47° pickoff mirror has two-axis tilt capabilities provided by stepper motors and flexure linkages, to compensate for uncertainties in our knowledge of HST's latch positions, i.e. instrument tilt with respect to the HST optical axis. These latch uncertainties would be insignificant in an unaberrated telescope, but must be compensated in a corrective optical system. In addition, three of the four fold mirrors, internal to the WFPC2 optical bench, have limited two-axis tilt motions provided by electrostrictive ceramic actuators and invar flexure mountings. Fold mirrors for the PC1, WF3, and WF4 cameras are articulated, while the WF2 fold mirror has a fixed invar mounting identical to those in WF/PC-1. A combination of the pickoff mirror and fold mirror actuators allows us to correct for potential pupil image

misalignments in all four cameras. Mirror adjustments should be infrequent following the initial alignment. The mechanisms are not available for GO use.

1.4.3. CCD Technology

The WFPC2 CCDs are thick, front-side illuminated devices made by Loral with a Lumogen phosphor coating, while WF/PC-1 CCDs are thinned, backside illuminated devices with a coronene phosphor. They support multi-pinned phase (MPP) operation. Based on the results of CCD screening tests at JPL the main differences may be summarized as follows:

- Read noise: WFPC2 CCDs have lower read noise (about $7e^-$ rms) than WF/PC-1 CCDs ($13e^-$ rms) which improves their faint object and UV imaging capabilities.
- Dark noise: Inverted phase operation yields lower dark noise for WFPC2 CCDs. It is expected that they can be operated at -70°C , which is warmer than the WF/PC-1 devices and should help in reducing the build-up of contaminants on the CCD windows.
- Flat field: WFPC2 CCDs have a more uniform pixel to pixel response ($<2\%$ pixel to pixel non-uniformity) which will improve the photometric calibration of science images.
- Pre-Flash: Deferred charge is negligible for WFPC2 CCDs. Pre-flash exposures will therefore not be required. This avoids the increase in background noise, and decrease in operational efficiency that results from a preflash.
- Gain switch: Two CCD gains are available with WFPC2, a $7e^-/\text{DN}$ channel which saturates at about $30000e^-$ (4096 DN) and a $14e^-/\text{DN}$ channel which saturates at about $60000e^-$ (4096 DN). This takes advantage of the greater full well available on the Loral devices, which are linear up to the saturation level in the $14e^-/\text{DN}$ channel.
- DQE: The Loral devices are thick, frontside illuminated devices with intrinsically lower QE above 4800\AA (and up to about 6500\AA) than thinned, backside illuminated wafers which have no attenuation by frontside electrode structures. On the other hand, the improved phosphorescent coating leads to higher DQE below 4800\AA . The peak DQE in the optical is 40% at 7000\AA while in the UV ($1100\text{-}4000\text{\AA}$) the DQE is 10-15%.
- Image Purge: The residual image resulting from a $100\times$ (or more) full-well over-exposure is well below the read noise within 30 minutes, removing the need for CCD image purging procedures after observations of particularly bright objects. The Loral devices bleed almost exclusively along the columns.
- Quantization: The systematic Analog to Digital converter errors present in the low order bits on WF/PC-1 have been eliminated, resulting in lower effective read noise.
- QEH: Quantum Efficiency Hysteresis (QEH) is not a significant problem in the Loral CCDs because they are frontside illuminated and incorporate MPP operation. The absence of any significant QEH also means that the devices do not need to be UV-flooded and so decontamination procedures can be planned without the constraint of maintaining the UV-flood.

1.4.4. UV Imaging

The contamination control issues for WFPC2 may be best understood in terms of the problems experienced with WF/PC-1. Since launch, WF/PC-1 has suffered from the accumulation of molecular contaminants on the cold (-87°C) CCD windows. This molecular accumulation results in the loss of FUV (1150-2000Å) throughput and attenuation at wavelengths as long as 5000Å. Another feature of the contamination is the "measles" - multiple isolated patches of low volatility contamination on the CCD window. Measles are present even after decontamination cycles, where most of the accumulated molecular contaminants are boiled off by warming the CCDs. In addition to the loss of a UV imaging capability, these molecular contamination layers scatter light and seriously impact both the long and short term calibration of the instrument. WFPC2 requires a factor of 10^4 - 10^5 reduction in material deposited on the cold CCD window, compared to WF/PC-1, to meet the project's goal of achieving 1% photometry at 1470Å over any 30 day period. This goal corresponds to the collection of a uniform layer of no more than 47 ng/cm² on the CCD window in that time. The changes involved are:

1. The venting and baffling particularly of the electronics have been redesigned to isolate the optical cavity.
2. There has been an extensive component selection and bake-out program, and changes in cleaning procedures.
3. The CCDs operate at a higher temperature, which reduces the rate of build-up of contaminants.
4. Molecular absorbers (Zeolite) are incorporated in the WFPC2.

1.4.5. Calibration Channel

An internal flat-field system provides reference flat-field images over the spectral range of WFPC2. The system contains tungsten incandescent lamps with spectrum shaping glass filters and a deuterium lamp. The flat-field illumination pattern will be uniform for wavelengths beyond about 1600Å, and differences between the flat-field source and the OTA will be handled in terms of calibrated ratio images that are not expected to have strong wavelength dependence. Short of 1600Å the flat-field is distorted due to refractive MgF₂ optics, and at these wavelengths the channel will primarily serve as a monitor of changes in QE. This system physically takes the place of the WF/PC-1 solar UV flood channel, which is unnecessary for WFPC2 and has been eliminated.

1.4.6. Spectral Elements

Revisions have been made to the set of 48 scientific filters, based on considerations of the scientific effectiveness of the WF/PC-1 filter set, and as discussed in a number of science workshops and technical reviews. WFPC2 preserves the WF/PC-1 'UBVRI' and 'Wide UBVRI' sequences, while extending the sequence of wide filters into the far UV. The photometric filter set also now includes an approximation to the Strömgren sequence. Wide-band UV filters will provide better performance below 2000Å, working together with the reductions in UV absorbing molecular contamination, the capability to remove UV-absorbing accumulations on cold CCD windows without disrupting the CCD quantum efficiencies and flat-field calibrations, and an internal source of UV reference flat-field images. We expect substantial improvements in narrow-band emission line photometry. All narrow-band filters are specified to have the same dimensionless bandpass profile. Center wavelengths and profiles are uniformly

accurate over the filter clear apertures, and laboratory calibrations include profiles, blocking, and temperature shift coefficients. The narrow-band set now includes a linear ramp filter which provides a dimensionless bandpass FWHM of 1% over the 3700-9800Å range.

1.5. ORGANIZATION OF THIS HANDBOOK

A description of the instrument is contained in Chapter 2. The filter set is described in Chapter 3. CCD performance is discussed in Chapter 4. A brief description of the expected Point Spread Function is given in Chapter 5. The details necessary to estimate exposure times are described in Chapter 6. Data products and standard calibration methods are summarized in Chapter 7.

This document summarizes the expected performance of the WFPC2 as known in March 1993 prior to its Thermal Vacuum testing (scheduled for early May 1993) and on-orbit calibration. Obviously, more information will become available as a result of these tests, and the information presented here has to be seen as preliminary. Observers are encouraged to contact the STScI Instrument Scientists for the latest information.

1.6. REFERENCES

The material contained in this Handbook is derived primarily from ground tests and design information obtained by the IDT and the engineering team at JPL. Other sources of information include:

1. "HST Phase 2 Proposal Instructions", (Version 4.0 January 1993).*
2. "Wide Field/Planetary Camera Final Orbital/Science Verification Report" S.M. Faber, editor, (1992). [IDT OV/SV Report]*
3. "STSDAS Calibration Guide ", (November 1991).*
4. "The Reduction of WF/PC Camera Images", Lauer, T., P.A.S.P. 101, 445 (1989).
5. "The Imaging Performance of the Hubble Space Telescope", Burrows, C. J., et al., Ap. J. Lett. 369, L21 (1991).
6. Interface Control Document (ICD) 19, "PODPS to STSDAS"
7. Interface Control Document (ICD) 47, "PODPS to CDBS"
8. "The Wide Field/Planetary Camera in The Space Telescope Observatory", J. Westphal and the WF/PC-1 IDT. IAU 18th General Assembly, Patras, NASA CP-2244 (1982).
9. "The WF/PC-1 Instrument Handbook", J. MacKenty, editor, STScI publication. (1992)*.
10. "Diagnosing the Optical State of the Hubble Space Telescope". Vaughan, A., J.B.I.S. 44, 487 (1991).
11. "White Paper for WFPC2 Far-Ultraviolet Science". J. T. Clarke and the WFPC2 IDT (1992)*.

* These documents may be obtained from the STScI User Support Branch (USB).

The STScI Science Programs Division (SPD) produces technical reports on the calibration and performance of the Science Instruments. Announcements of these reports appear on the STEIS electronic bulletin board system and they can be obtained by writing to the STScI WFPC2 Instrument Scientist. Questions relating to the scientific use and calibration of the WFPC2 may also be directed to the Instrument Scientists.

2. INSTRUMENT DESCRIPTION

2.1. SCIENCE OBJECTIVES

The scientific objectives of the WFPC2 are to provide photometrically and geometrically accurate, multi-band images of astronomical objects over a relatively wide field-of-view (FOV), with high angular resolution across a broad range of wavelengths.

WFPC2 will meet or exceed the photometric performance requirements for WF/PC-1. Nominally, this requirement is 1% photometric accuracy in all filters, which is essentially a requirement that the relative response in all 800×800 pixels per CCD be known to a precision of 1% in flat-field images taken through each of the 48 science filters. Success in this area is dependent on the stability of all elements in the optical train particularly the CCDs, filters and calibration channel.

Recovery of the point spread function is essential to all science programs to be conducted with the WFPC2, because it is recovery of the PSF that allows HST to both go deeper than ground based imagery and to resolve smaller scale structure with higher reliability and dynamic range. In addition, accomplishing the scientific goals which originally justified the HST requires that good quality images be obtained across as wide a field of view as possible. The Cepheid distance scale program, for example, cannot be accomplished without a relatively wide field of view.

A unique capability of the WFPC2 is that it provides a sustained, high resolution, wide field imaging capability in the vacuum ultraviolet. Considerable effort has been expended to assure that this capability is maintained. Broad passband far-UV filters, including a Sodium Woods filter, are planned for the filter set. The Woods filter has superb red blocking characteristics. Photometry at wavelengths short of 3000Å is improved through the control of internal molecular contamination sources and the ability to put the CCDs through warm-up decontamination cycles without loss of prior calibrations.

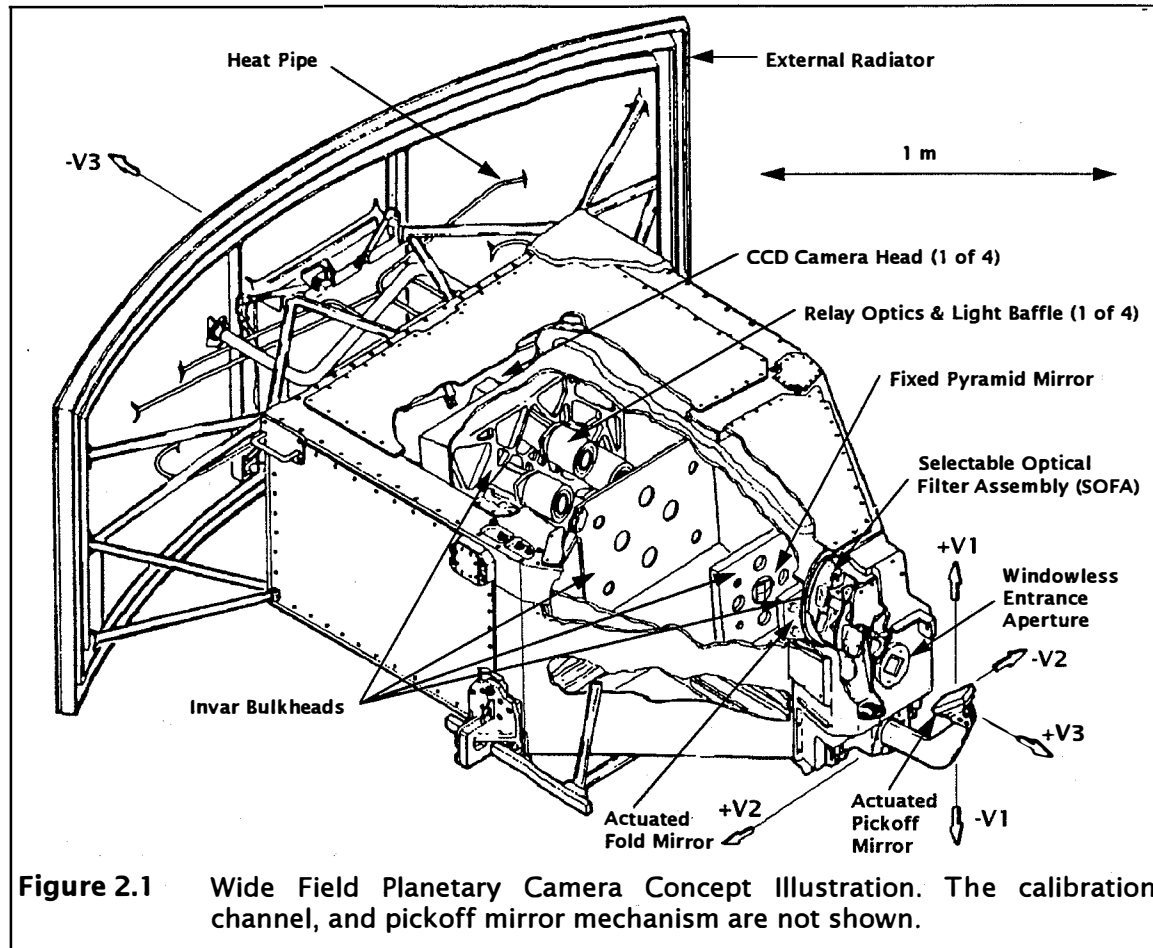
While the WFPC2 CCDs have lower V-band quantum efficiency than the WF/PC-1 chips, for most applications this is more than made up for by the lower read noise, improved charge transfer efficiency, and intrinsically uniform flat field. These characteristics are expected to increase the accuracy of stellar photometry, where uncertainty in the flat field is a major contributor to the uncertainties in photometry with WF/PC-1. They will also enhance the quality of low light level exposures where read noise and deferred charge limit sensitivity in WF/PC-1.

2.2. WFPC2 CONFIGURATION, FIELD OF VIEW AND RESOLUTION

The field of view and angular resolution of the wide field and planetary camera is split up as follows:

Field	Pixel and CCD Format	Field of View	Pixel Scale	F/ratio
Wide Field	800 × 800 × 3 CCDs	2.5 × 2.5 arcminutes (L-shaped)	100 milli- arcseconds	12.9
Planetary	800 × 800 × 1 CCD	35 × 35 arcseconds	46 milli- arcseconds	28.3

Table 2.1 Summary of Camera Format



2.3. OVERALL INSTRUMENT DESCRIPTION

The Wide-Field and Planetary Camera, illustrated in Figure 2.1, occupies the only radial bay allocated to a scientific instrument. Its field of view is centered on the optical axis of the telescope and it therefore receives the highest quality images. The three Wide-Field Cameras (WFC) at F/12.9 provide an "L" shaped field-of-view of 2.5×2.5 arcminutes with each $15 \mu\text{m}$ detector pixel subtending 0.10 arcseconds on the sky. In the Planetary Camera (PC) at F/28.3, the field-of-view is 35×35 arcseconds, and each pixel subtends 0.046 arcseconds. The three WFCs undersample the point spread function of the optical telescope assembly (OTA) by a factor of 4 at 5800\AA in order to provide an adequate field-of-view for studying galaxies, clusters of galaxies, etc. The PC resolution is over two times higher. The PC field of view is adequate to provide full-disk images of all the planets except Jupiter (which is 47 arcseconds in maximum diameter). It has numerous extra-solar applications, including studies of galactic and extra-galactic objects in which both high angular resolution and excellent red-light sensitivity are needed. The WFPC2 can be used as the prime instrument, for target acquisition, and for parallel observations.

Figure 2.2 shows the optical arrangement (not to scale) of the WFPC2. The central portion of the OTA F/24 beam is intercepted by a steerable pick-off mirror that is attached to the WFPC2 and is diverted through an entry port into the instrument. Unlike WF/PC-1, the entry port is not sealed with an afocal MgF₂ window. The beam

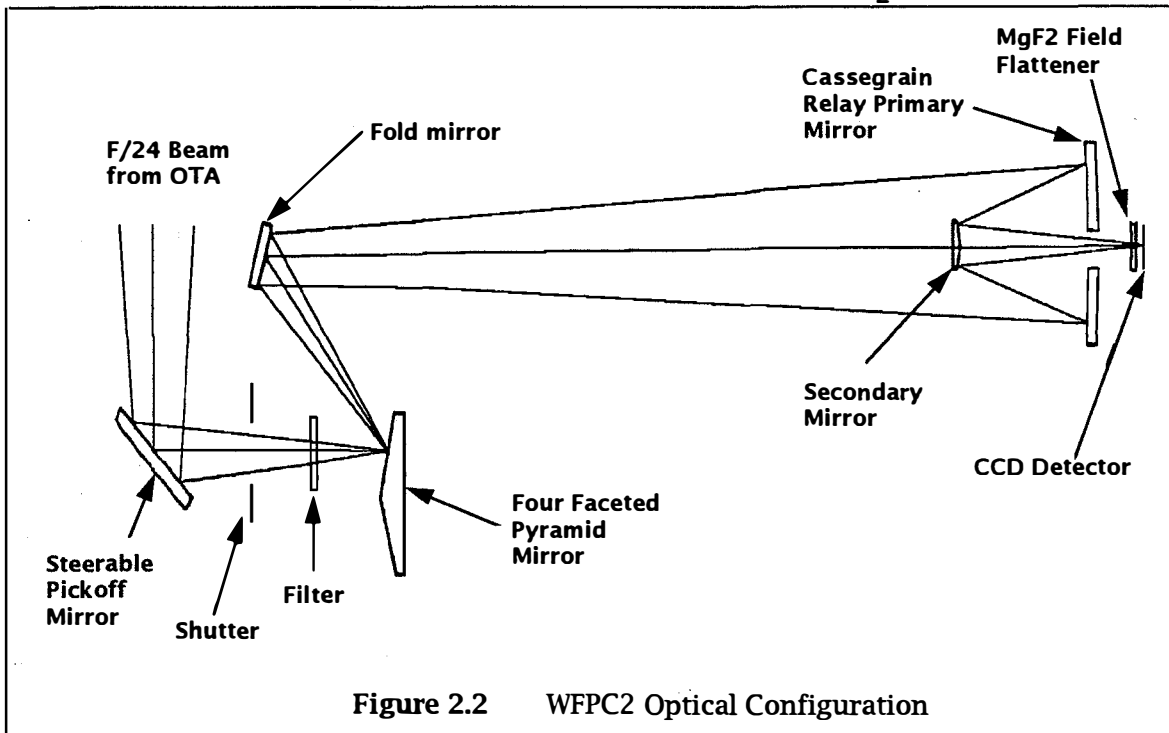


Figure 2.2 WFPC2 Optical Configuration

passes through a shutter and is analysed in spectral content by a filter. A total of 48 spectral elements and polarizers are contained in an assembly of 12 filter wheels. The beam then falls on a shallow-angle, four-faceted pyramid located at the aberrated OTA focus, each face of the pyramid being a concave spherical surface. The pyramid divides the OTA image of the sky into four parts. After leaving the pyramid, each quarter of the full field-of-view is relayed by an optical flat to a cassegrain relay that forms a second field image on a charge-coupled device (CCD) of 800×800 pixels. Each detector is housed in a cell that is sealed by a MgF₂ window. This window is figured to serve as a field flattener.

The aberrated HST wavefront is corrected by introducing an equal but opposite error in each of the four cassegrain relays. The convergence of fossil and on-orbit data on a value for the HST aberration provides confidence that the optical prescription for this correction is well understood. An image of the HST primary mirror is formed on the secondary mirrors in the cassegrain relays. The previously flat fold mirror in the PC channel has a small curvature to ensure this, and this is why the magnification is changed from F/30 to F/28.3 in WFPC2. The spherical aberration from the telescope's primary mirror is corrected on these secondary mirrors, which are extremely aspheric. The point spread function is then close to that originally expected for WF/PC-1.

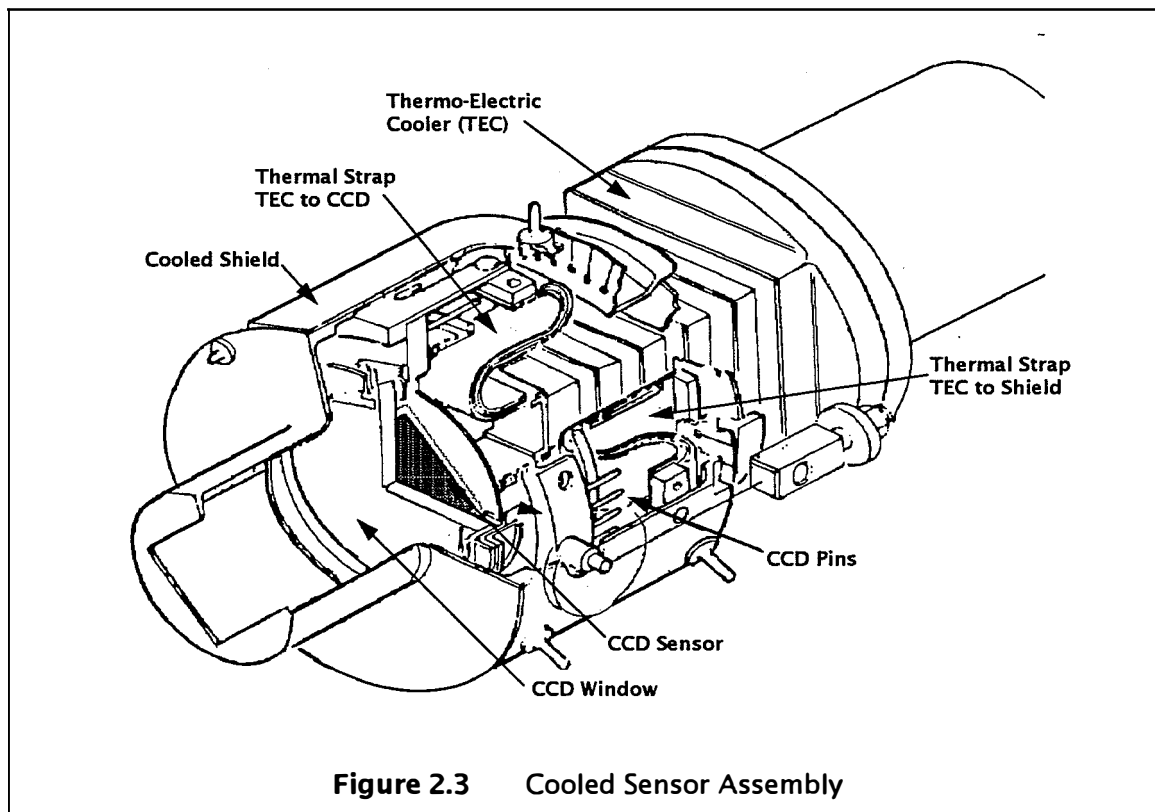
The single most critical and challenging technical aspect of applying a correction is assuring exact alignment of the WFPC2 pupils with the pupil of the HST. If the image of the HST primary does not align exactly with the repeater secondary, the aberrations no longer cancel, leading to a wavefront error and comatic images. An error of only 2% of the pupil diameter produces a wavefront error of 1/6 wave, leading to degraded spatial resolution and a loss of about 1 magnitude in sensitivity to faint point sources. This error corresponds to mechanical tolerances of only a few microns in the tip/tilt motion of the pickoff mirror, the pyramid, and the fold mirrors. The mechanical

tolerances required to passively maintain WFPC2 alignment far exceed the original requirements for WF/PC-1. Actuated optics are being incorporated into WFPC2 to assure that accurate alignment, and hence good images, can be achieved and maintained on orbit. The beam alignment is set with a combination of the steerable pickoff mirror and actuated fold mirrors in cameras PC1, WF3 and WF4.

The WFPC2 pyramid cannot be focussed or rotated. The pyramid motor mechanism has been eliminated because of stability and contamination concerns. WFPC2 will be focussed by moving the OTA secondary mirror, and then COSTAR and any future science instruments will be adjusted in focus to ensure to a common focus for all the HST Instruments.

The OTA spherical aberration greatly reduces the utility of the low reflectance 'Baum' spot on the pyramid in the WF/PC-1 design, which has therefore been eliminated.

After a selected integration time (≥ 0.11 seconds), the camera shutter is closed, and the full 1600×1600 pixel field-format may be recovered by reading out and assembling the outputs from the four CCDs. The CCDs are physically oriented and clocked so that the pixel read-out direction is rotated approximately 90° in succession (see Figure 1.1). The (1,1) pixel of each CCD array is thereby located near the apex of the pyramid. As a registration aid in assembling the four frames into a single picture, a light can be turned on at the pyramid to form a series of eleven fixed artificial "stars" (known as Kelsall spots or K-spots) along the boundaries of each of the quadrants. This calibration is normally done in a separate exposure. In WFPC2 the K-spot images will be aberrated and similar in appearance to the uncorrected HST PSF. The relative alignment of the four channels will be more accurately determined from star fields, which can be used if, as expected, the alignment is stable over long periods.



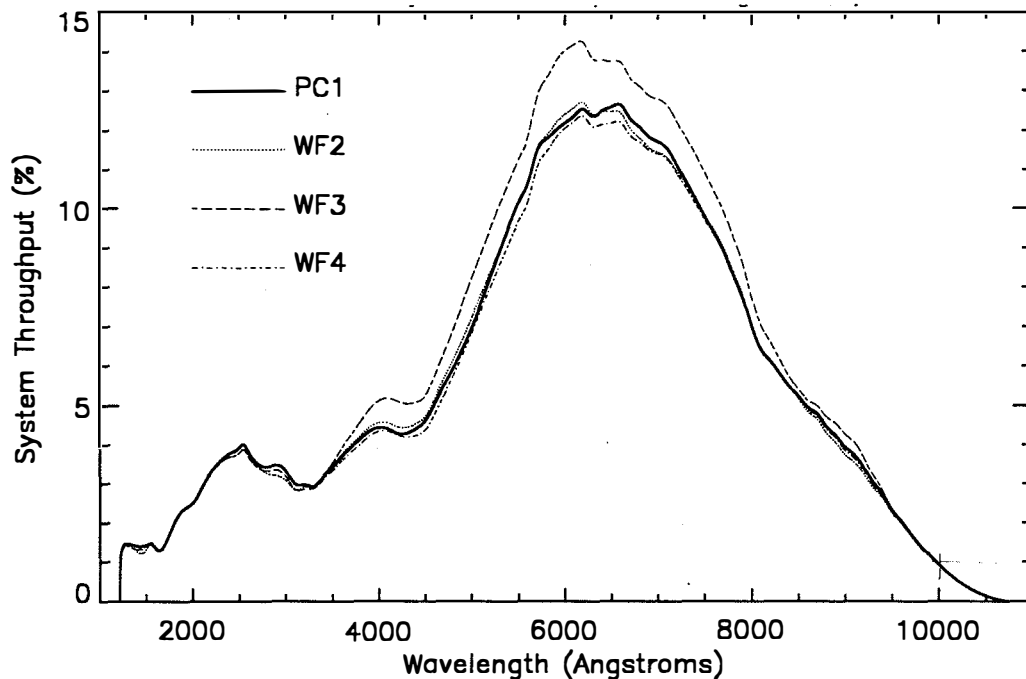


Figure 2.4 WFPC2 + OTA System Throughput. WF3 is not believed to be intrinsically more sensitive. Instead, the spread in the curves should be understood to come from uncertainties in these preliminary measurements.

Each CCD is a thick frontside-illuminated silicon sensor, fabricated by Loral Aerospace. A CCD, mounted on its header, is hermetically packaged in a ceramic-tube body that is filled with 1.1 atmosphere of Argon to prevent degradation of the UV sensitive phosphor and sealed with the MgF_2 field flattener. This complete cell is connected with compliant silver straps to the cold junction of a thermo-electric cooler (TEC). The hot junction of the TEC is connected to the radial bay external radiator by an Ammonia heat pipe. This sensor-head assembly is shown in Figure 2.3. During operation, each TEC cools its sensor package to suppress dark current in the CCD.

The WFPC2 provides a useful sensitivity from 1150Å to 11000Å in each detector. The overall spectral response of the system is shown in Figure 2.4 (not including filter transmissions). The curves represent the probability that a photon that enters the 2.4m diameter HST aperture at a field position near the center of one of the detectors will pass all the aperture obscurations, reflect from all the mirrors, and eventually be detected as an electron in the CCD. The throughput of the system combined with each filter is tabulated in Table 6.1 on page 54 and also shown in the Appendix.

The visible and red sensitivity of the WFPC2 is a property of the silicon from which the CCDs are fabricated. To achieve good ultraviolet response each CCD is coated with a thin film of lumogen, a phosphor. Lumogen converts photons with wavelengths <4800Å into visible photons with wavelengths between 5100Å and 5800Å. The CCD detects these visible photons with good sensitivity. Beyond 4800Å, the lumogen becomes transparent and acts to some degree as an anti-reflection coating. Thus, the full wavelength response is determined by the MgF_2 field flattener cutoff on the short-wavelength end, and the silicon band-gap in the infrared at 1.1 eV (~11000Å).

With the WFPC2 CCD sensors, images may be obtained in any spectral region defined by the chosen filter with high photometric quality, wide dynamic range, and excellent spatial resolution. The bright end of the dynamic range is limited by the 0.11

seconds minimum exposure time, and by the saturation level of the selected analog to digital converter, which is roughly 60000 or 30000e⁻ per pixel. The maximum signal-to-noise ratio corresponding to a fully exposed pixel will be about 250. The faint end of the dynamic range is limited by photon noise, instrument read noise and, for the wide-band visible and infra-red filters, the sky background.

Table 2.2 gives characteristic values of the expected dynamic range in visual magnitudes for point sources. The minimum brightness is given for an integrated S/N ratio of 3, and the maximum corresponds to full well (selected as 60000e⁻). The quoted values assume an effective bandwidth of 1000Å at about 5700Å (the F569W filter). The Planets, like many other resolved sources, will be observable with short exposure times even if their integrated brightness exceeds the 8.6 magnitude limit.

Configuration	Exposure (seconds)	Min. V Magnitude	Max. V. Magnitude
Wide Field	0.11	9.2	17.9
Wide Field	3000.	20.3	28.5
Planetary	0.11	8.6	17.3
Planetary	3000.	19.7	28.2

Table 2.2 *WFPC2 Dynamic Range in a Single Exposure*

2.4. SHUTTER

The shutter is a two-blade mechanism used to control the duration of the exposure. A listing of the possible exposure times is contained in Table 2.3. These are the only exposure times which can be commanded. Current policy is to round down non-valid exposure times to the next valid value. An exposure time of less than 0.11 seconds will therefore only result in a bias frame being taken.

Some exposures should be split into two (CR-SPLIT) in order to allow cosmic ray events to be removed in post-processing. By default, exposures of more than 10 minutes are CR-SPLIT. If an exposure is CR-SPLIT then the exposure time is halved (unless the user specifies a different fraction), and then rounded down. Note that some exposure times in the table do not correspond to commandable values when halved. In preparing a proposal that is to be CR-SPLIT, the simplest procedure to use in order to be sure of a given exposure time is to enter double a legal value.

For the shortest exposure times, it is possible to reconstruct the actual time of flight of the shutter blades. Encoder disks, attached to the shutter blade arms, are timed by means of a photo-transistor. The maximum error is 5 milliseconds. The necessary information is contained in the WFPC2 engineering data stream. However, this information is not in the processed science header.

When obtaining very short exposures, diffraction effects from the edges of the shutter blades affect the point spread function. Especially when using short exposures to obtain point spread functions in support of long exposure observations, it is advisable to use exposure times greater than 0.2s (see the WF/PC-1 IDT OV/SV Report, Chapter 9 for further discussion in the spherically aberrated case).

The control of the initial opening of the WFPC2 shutter during an observation is held by the internal WFPC2 microprocessor in all cases. However, control over when the shutter is closed is held by the microprocessor only for exposures less than 180 seconds in duration. For longer exposures the control over when the shutter is closed resides with the Application Processor (AP-17) in the NSSC-1 Spacecraft computer. The consequence of this arrangement is that loss of guide star lock will result in the WFPC2 shutter being closed only for those observations with planned durations longer than 180 seconds. The AP-17 always controls the shutter closing if the serial clocks are selected on during the exposure (CLOCKS=YES), which then has a minimum planned

duration of 1 second. If guide star lock is reacquired prior to the end of the planned observation time, the shutter will reopen to obtain a portion of the planned integration.

<u>0.11</u>	<u>0.4</u>	2.0	10.	40.	200.	900.	1900.	2900.	3900.	4900.	6200.	15000
<u>0.12</u>	<u>0.5</u>	2.3	12.	50.	230.	1000.	2000.	3000.	4000.	5000.	6400.	20000
<u>0.14</u>	<u>0.6</u>	2.6	14.	60.	260.	1100.	2100.	3100.	4100.	5100.	6600.	25000
<u>0.16</u>	<u>0.7</u>	3.0	16.	70.	300.	1200.	2200.	3200.	4200.	5200.	6800.	30000
<u>0.18</u>	<u>0.8</u>	3.5	18.	80.	350.	1300.	2300.	3300.	4300.	5300.	7000.	40000
<u>0.20</u>	1.0	4.0	20.	100.	400.	1400.	2400.	3400.	4400.	5400.	7500.	50000
<u>0.23</u>	1.2	5.0	23.	120.	500.	1500.	2500.	3500.	4500.	5500.	8000.	75000
<u>0.26</u>	1.4	6.0	26.	140.	600.	1600.	2600.	3600.	4600.	5600.	8500.	100000
<u>0.30</u>	1.6	7.0	30.	160.	700.	1700.	2700.	3700.	4700.	5800.	9000.	
<u>0.35</u>	1.8	8.0	35.	180.	800.	1800.	2800.	3800.	4800.	6000.	10000	

Table 2.3 Quantized Exposure Times (Seconds). Exposure times where the PSF is affected by shutter flight time are underlined; Exposures normally without loss of lock checking are in *italics*; Exposures that are CR-Split by default are in **boldface**. Exposures that take more than one orbit even when CR-split are not normally accessible to GOs and are ~~crossed~~. Exposure times that are unavailable when CLOCKS=YES are shaded.

2.5. OVERHEAD TIME

It is not generally possible to schedule exposures less than 3 minutes apart. Commands to the WFPC2 are processed at spacecraft "major frame" intervals of one minute. A filter wheel may be returned to its "clear" position and another filter selected in one minute. An exposure takes a minimum of one minute, and a readout of the CCDs takes one minute. There is no overhead time advantage in reading out a subset of the CCDs except when the WFPC2 readout occurs in parallel with the operation of a second instrument (where 2 minutes may be required to readout all 4 CCDs). Preflash overhead is eliminated because preflash is not necessary in WFPC2 to avoid deferred charge. The RPSS Resource Estimator should be used in developing Phase 2 proposals.

2.6. CCD ORIENTATION AND READOUT

The relation between the rows and columns for the four CCDs is shown in Figure 1.1. Note that each CCD is similarly sequenced, so that their axes are defined by a 90° rotation from the adjacent CCD. If an image were taken of the same field with each of the CCDs and then displayed with rows in the "X" direction and columns in the "Y" direction, each successive display would appear rotated by 90° from its predecessor.

The aberrated image of the pyramid edge is 40±20 pixels from the edge of the format along the two edges of each CCD which butt against the fields of view of neighboring CCDs. Figure 1.1 illustrates the projected orientation of the WFPC2 CCDs onto the sky. Because the beam is aberrated at the pyramid, there is a vignetted area at the inner edge of each field with a width of 4 arcseconds. The vignetted light ends up focussed in the corresponding position in the adjacent channel (with complementary vignetting). The inner edges of the field projected onto the CCDs are given in Table 2.4.

The WFPC2 has two readout formats, namely full single pixel resolution (FULL Mode), and 2×2 pixel summation (AREA Mode). Each line of science data is started with two words of engineering data, followed by 800 (FULL) or 400 (AREA) 16-bit positive numbers as read from the CCDs. In FULL Mode the CCD pixels are followed by 11 "bias" words ("overclocked" pixels), making a total of 813 words per line for 800 lines. In AREA Mode, there are 14 bias words giving a total of 416 words per line for 400 lines. Either pixel format may be used to read out the WFC or PC. These outputs are reformatted into the science image and extracted engineering data files during processing in the HST ground system prior to delivery to the observer.

Camera	Start Vignetted Field	Contiguous field	Start Unvignetted Field
PC1	X>-4 and Y>-4	X>40 and Y>40	X>84 and Y>84
WF2	X>20 and Y>20	X>40 and Y>40	X>60 and Y>60
WF3	X>20 and Y>20	X>40 and Y>40	X>60 and Y>60
WF4	X>20 and Y>20	X>40 and Y>40	X>60 and Y>60

Table 2.4 *Nominal Inner Field Edges. The CCD X,Y (Column,Row) numbers given are uncertain at the 20 pixel level.*

The advantage of the AREA Mode (2x2) on-chip pixel summation is that readout noise is maintained at 7 electrons rms for the summed (i.e., larger) pixels. This pixel summation is useful for some photometric observations of extended sources particularly in the UV. Cosmic ray removal is more difficult in AREA Mode.

The readout direction along the columns of each CCD is indicated by the small arrows near the center of each camera field in Figure 1.1. Columns and rows are parallel and orthogonal to the arrow, respectively. Each CCD is read out from the corner nearest the center of the diagram, with column (pixel) and row (line) numbers increasing from the diagram center. In a saturated exposure, blooming will occur almost exclusively along the columns because of the MPP operating mode of the CCDs. Diffraction spikes caused by the Optical Telescope Assembly and by the internal Cassegrain optics of the WFPC2 are at 45° to the edges of the CCDs. The default pointing position when all 4 CCDs are used is on WF3, approximately 10 arcseconds along each axis from the origin.

Observations which require only the field of view of a single CCD are best made with the target placed near the center of a single CCD rather than near the center of the 4 CCD mosaic. This will result in a marginally better point spread function, and avoid photometric, astrometric and cosmetic problems in the vicinity of the target caused by the overlap of the cameras.

While for such observations, only the field of view of a single CCD detector is actually required, the default operational mode is to read out all four CCDs. In the case of WF/PC-1, this policy has resulted in serendipitous discoveries, and the recovery of useful observations in the case of small pointing or coordinate errors.

On the other hand any combination of 1, 2 or 3 CCDs may be read out in numerical order. This partial readout capability is not generally available to GOs although it can be used if certain constraints mandate it, after discussion with the WFPC2 instrument scientists. It does not result in a decrease in the readout overhead time but does conserve limited space on the HST on-board science tape recorder. The capacity of this tape recorder is slightly over 7 full (4 CCD) WFPC2 observations and 18 single CCD WFPC2 observations on a single side (of two). Switching sides of the tape recorder without a pause will result in the loss of part of a single CCD readout. Since an interval of about 30 minutes must normally be allowed for the tape recorder to be copied to the ground, readout of only a subset of the WFPC2 CCDs can be advantageous when many frames need to be obtained in rapid succession.

Multiple exposures may be obtained with or without spacecraft motion between them followed by a readout with the restriction that the WFPC2 will be read out at least once per orbit.

3. OPTICAL FILTERS

A set of 48 filters are included in WFPC2, with the following features:

1. It approximately replicates the WF/PC-1 "UBVRI" photometry series.
2. The broad-band filter series is extended into the far UV.
3. There is a new Strömgren series.
4. A Wood's' filter is included for far-UV imaging without a red leak.
5. There is a 1% bandpass linear ramp filter series covering 3700--9800Å.
6. The narrow-band series is more uniformly specified and better calibrated.

The filters are mounted in the Selectable Optical Filter Assembly (SOFA) between the shutter and the reflecting pyramid. The SOFA contains 12 filter wheels, each of which has 4 filters and a clear "home" position. A listing of all simple optical elements in the SOFA mechanism and the location of each element (by wheel number 1-12, and position 1-4) is given in Table 3.1. Wheel number 1 is located closest to the shutter. The categories of simple filters (F) are long-pass (LP), wide (W), medium (M), and narrow (N). Most of these filters are either flat single substrates or sandwiches.

The filter complement will almost certainly include two solar blind Wood's filters F160AW and F160BW. However, because there is some technical risk associated with these filters, the filter that they replace, F157W is documented in place of F160AW in Table 3.1, and might be used to replace one of the Wood's filters.

In addition to the above complement of broad and narrowband filters WFPC2 features a set of three specialized quadrant (quad or Q) filters in which each quadrant corresponds to a facet of the pyramid, and therefore to a distinct camera relay. There is one quad containing four narrowband, redshifted [OII] filters with central wavelengths from 3763-3986Å, one quad with four polarizing elements (POL) with polarization angles, 0, 45, 90 and 135 degrees, and one quad with four methane (CH₄) band filters with central wavelengths from 5433-8929Å. The polarizer quad filter, can be crossed with any other filter over the wavelength range from 2800Å to 8000Å, with the exception of the Methane Quad and Redshifted [OII] Quad which share the same wheel. The SOFA also contains four linearly variable narrowband ramp (FR) filters (in the twelfth wheel - closest to the focus). The quad and ramp filters are listed in Table 3.2

In Tables 3.1 and 3.2, each of the Type "A" filters is equivalent to inserting 5mm of quartz in terms of optical path length, with compensation for wavelength such that focus is maintained on the CCDs. A configuration with no filters in the beam results in out-of-focus images and will not generally be used. With the exception of the quad polarizer and blocking (Type "B") filters, all filters are designed to be used alone. All combinations where the number of type "A" filters is not unity will result in out-of-focus images. The image blur resulting from two or zero type "A" filters at visible wavelengths is equivalent to 2.3 mm defocus in the F/24 beam, which corresponds to 1/5 wave rms of defocus at 6328Å, and a geometrical image blur of 0.34 arcseconds. While this is a large defocus, the images are still of very high quality compared for example to seeing limited images. Some such combinations may be scientifically attractive. For example, the Wood's filter may be crossed with another UV filter to provide a solar blind passband (although the efficiency will be low).

Name	Type	Wheel/ Slot	Notes	In WF/PC-1?	$\bar{\lambda}$ (Å)	$\Delta\bar{\lambda}$ (Å)	Peak T (%)	Peak λ (Å)	
F122M	A	1	4	H Ly alpha - Red Leak	Y	1256	184.9	13.8	1247
F130LP	B	2	1	CaF2 Blocker	N	3838	5568.2	94.7	4332
F157W**	A	1	3	Baseline is F160AW here	Y	1506	367.6	17.0	1360
F160BW	A	1	2	Woods B	N	1471	466.5	19.0	1436
F165LP	B	2	2	Suprasil Blocker	N	4357	5532.0	95.4	5788
F170W	A	8	1		N	1675	469.5	26.2	1667
F185W	A	8	2		N	1909	296.6	23.7	1849
F218W	A	8	3	Interstellar Feature	N	2137	353.6	22.2	2091
F255W	A	8	4	Wide U	N	2557	408.0	17.0	2483
F300W	A	9	4		N	2925	727.7	47.9	2760
F336W	A	3	1	U and Strömgren μ	Y	3327	370.7	70.4	3447
F343N	A	5	1	Ne V	N	3404	58.7	19.7	3433
F375N	A	5	2	Redshifted [OII] 3727	Y	3737	26.7	17.2	3736
F380W	A	9	1		N	3934	694.7	65.0	3979
F390N	A	5	3	CN	N	3889	45.3	36.9	3885
F410M	A	3	2	Strömgren nu	N	4089	146.9	72.8	4098
F437N	A	5	2	[OIII]	Y	4369	25.2	49.6	4368
F439W	A	4	4	B	Y	4292	464.4	71.3	4176
F450W	A	10	4	Wide B	N	4445	925.0	91.1	5061
F467M	A	3	3	Stromgren b	N	4682	171.4	80.0	4728
F469N	A	6	1	He II	Y	4694	24.9	56.9	4699
F487N	A	6	2	H beta	Y	4865	25.8	63.0	4863
F502N	A	6	3	[OIII]	Y	5012	26.9	57.9	5009
F547M	A	3	4	Stromgren γ (but wider)	Y	5454	486.6	86.6	5361
F555W	A	9	2		Y	5252	1222.5	94.9	5150
F569W	A	4	2	V	Y	5554	965.7	92.0	5313
F588N	A	6	4	He I & Na I (NaD)	Y	5892	49.1	92.1	5895
F606W	A	10	2	Wide V	Y	5843	1578.7	98.3	6187
F622W	A	9	3		Y	6157	935.4	96.2	6034
F631N	A	7	1	[OI]	Y	6283	30.6	90.2	6281
F656N	A	7	2	H-alpha	Y	6562	21.9	86.2	6561
F658N	A	7	3	[NII]	Y	6590	28.5	83.3	6592
F673N	A	7	4	[SII]	Y	6733	47.2	82.1	6733
F675W	A	4	3	R	Y	6735	889.4	98.6	6796
F702W	A	10	3	Wide R	Y	6997	1480.7	99.0	6539
F785LP	A	2	3		Y	9367	2094.8	98.3	9960
F791W	A	4	1	I	Y	8006	1304.1	99.4	8081
F814W	A	10	1	Wide I	Y	8269	1758.0	98.7	8386
F850LP	A B	2	4		Y	9703	1669.5	94.2	10026
F953N		1	1	[SIII]	N	9542	54.5	90.7	9530
F1042M		A	11	2		Y	10443	610.9	95.2

Table 3.1 WFPC2 Simple (F') Filter Set. The effective wavelength, width and transmission quoted are defined in Chapter 6, but do not include the system (OTA+WFPC2) response.

**F157W is documented as a contingency. The baseline is to use F160AW in this slot.

The mean wavelength $\bar{\lambda}$ is similar to that defined in Schneider, Gunn and Hoessel (Ap. J. 264, 337). The width is the FWHM of a Gaussian filter with the same second moment and is reasonably close to the FWHM. The values tabulated here do not include the CCD DQE or the transmission of the OTA or WFPC2 optics (as given in Figure 2.4). In Chapter 6 the corresponding quantities are given including the effect of the other optical elements and the CCD DQE.

Name	Type	Wheel/ Slot	Notes	In WF/PC-1?	$\bar{\lambda}$ (Å)	$\Delta\bar{\lambda}$ (Å)	Peak T (%)	Peak λ (Å)
FQUVN-A	A	11	3 Redshifted [OII]	N	3766	73.4	24.0	3769
FQUVN-B	A	11	3 Redshifted [OII]	N	3831	57.4	30.5	3827
FQUVN-C	A	11	3 Redshifted [OII]	N	3913	59.3	38.9	3908
FQUVN-D	A	11	3 Redshifted [OII]	N	3993	63.6	43.4	3990
FQCH4N-A	A	11	4 CH4 543	N	5462	72.3	83.8	5442
FQCH4N-B	A	11	4 CH4 619	N	6265	157.7	83.7	6202
FQCH4N-C	A	11	4 CH4 727	N	7324	112.4	89.7	7279
FQCH4N-D	A	11	4 CH4 892	N	8940	59.4	91.2	8930
POLQ	B	11	1 Parallel Quad 0,45,90,135	N	5427	5797.6	90.8	10992
POLQ	B	11	1 Perpendicular Polarization	N	7922	6653.4	89.7	10992
FR418N	A	12	1 Ramp W=3700-4720	N	W	W/100	~20-50	W
FR533N	A	12	2 Ramp W=4720-6022	N	W	W/100	~40-50	W
FR680N	A	12	3 Ramp W=6022-7683	N	W	W/100	~60-80	W
FR868N	A	12	4 Ramp W=7683-9802	N	W	W/100	~70-85	W

Table 3.2 *WFPC2 quad and ramp filters. The quad polarizer is represented for both parallel and perpendicular polarization to its polarization direction, which is different in each quadrant.*

Figure 3.1 summarizes the normalized transmission curves for the simple ("F") filters and narrowband quad filters. It does not include curves for the polarizing quad, or the linear ramp filters which are documented in Sections 3.1 and 3.3 respectively. Individual filter transmission curves are shown in the Appendix in Sections 8.1 (filters alone) and 8.2 (system response included). Figure 3.1 divides the filters into the following groups:

- (1) Long pass filters designed to be used in combination with another filter.
- (2) Wide bandpass filters with FWHM ~25% of the central wavelength.
- (3) Wide bandpass approximations to the UBVRI sequence designed for use on faint sources.
- (4) A photometric set including closer approximations to UBVRI passbands (see Harris et al. 1991, A.J. 101, 677). Note, however, that the WFPC2 UBVRI series is not the Johnson-Cousins photometric series, neither is it identical with the corresponding WF/PC-1 series. See Chapter 6 for detailed comparisons.
- (D) Medium bandpass filters with FWHM ~10% of the central wavelength, including an approximation to the Strömgren photometric series.
- (5) Narrow bandpass filters for isolating individual spectral lines or bands.
- (6) Redshifted [OII] and CH₄ narrow bandpass quad filters.

Note that the UV filters have some degree of "red leak", which is quantified in Chapter 6 where the system response is included.

A passband calibration is maintained in the calibration database system (CDBS). It will be updated following System Level Thermal Vacuum (SLTV) testing, and again following on orbit calibrations. **Until these calibrations are completed, the information given here must be regarded as approximate and preliminary.** In particular, the ground based calibration of the narrowband filters' central wavelengths has not been corrected for temperature effects and is therefore accurate to about 2Å. Because of this, it is not advisable to place narrow emission lines at the half power points of such filters and expect to predict the throughput to high accuracy. Either the standalone software package XCAL or SYNPHOT running under IRAF can be used to access CDBS.

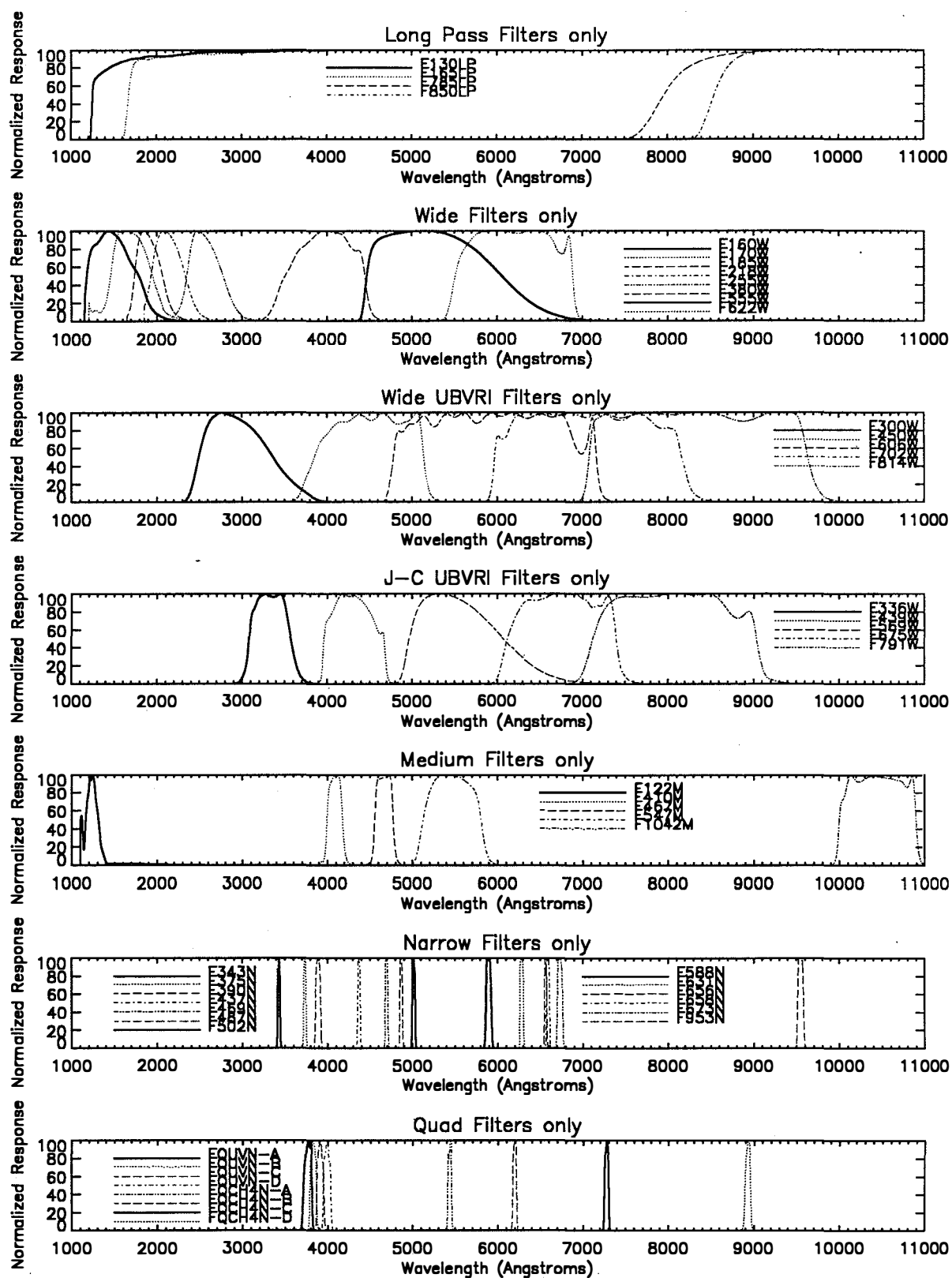


Figure 3.1 Summary of normalized filter curves

3.1. LINEAR RAMP FILTERS

The linear ramp filters are designed for narrowband absorption and emission line imaging of moderately extended objects. Each filter is divided into four parallel strips where the central wavelength across each strip varies by approximately 6%. Each CCD pixel is, thus, mapped to a unique central wavelength with a FWHM band width of approximately 1% of the central wavelength. The maximum size of an object which can be imaged at a given wavelength is approximately 13 arcseconds and is determined by the width of the strips and the image size at the filter. The cumulative wavelength range of the four linear ramp filters is 3700 to 9802 Å. Originally intended for a four WFC configuration, the linear ramp filters require partial rotation of the SOFA wheels to -18 and -33 degrees from their nominal positions, to recover wavelength regions which would fall on the PC camera or otherwise be lost. There will be vignetting at some wavelengths for these partial rotations.

3.1.1. Spectral Response

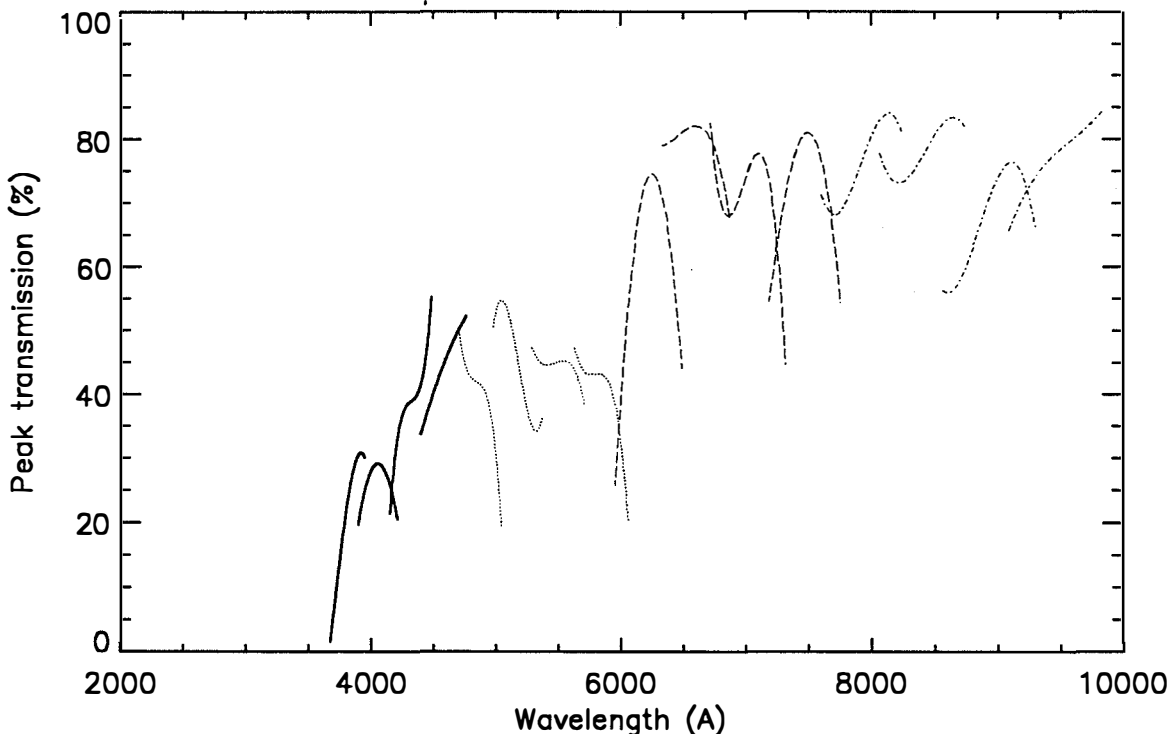


Figure 3.2 Ramp Filter Peak Transmission. The four line types correspond to the four different filters (each containing four ramps)

A JPL Interoffice Memorandum DM # 2031 (December 30, 1992) gives the results of a prediction scheme to locate and quantify the passbands of the four WFPC2 flight ramp filters, RF418n, RF533n, RF680n and RF866n. The results are summarized here.

Laboratory (room temperature) measurements of the passbands of the four ramp filters were made at 5 equally spaced intervals on each of the four ramp stripes on each filter for a total of 80 passband measurements. The laboratory measurements were made with a narrow beam and were then integrated over a "donut" area of the filter to simulate the beam profile at the ramp filter. The radius of the beam is 3.7mm, or 13 arcseconds. The integration was carried out by assuming the nominal linear shift in wavelength with position and that no significant changes in the passband shape occur

across the beam. The integration makes the shape of the passband quite symmetric. The resulting curves can then be fitted to within a few percent with a Munson function:

$$T = T_0 / \{1 + (1-a)x^2 + a(1-b)x^4 + ab(1-c)x^6 + abcx^8\}$$

where a , b and c are shape parameters, and $0 \leq a, b, c \leq 1$; T_0 is the peak transmission of the passband, $T=T_0$ at $x=0$; x is related to wavelength λ by $x=(\lambda-\lambda_0)/H$, $T=T_0/2$ at $x=1$ (so H is the half width at half maximum).

The parameters, $(\lambda_0, T_0, H, a, b, c)$ were then fitted to polynomial functions of position Y (which starts at 0 inches at the lower wavelength edge of each strip) to predict the filter response for areas of the filters between the tested points. Good quadratic fits are in general available for all the parameters except for T_0 which requires a cubic. The results are given in Tables 3.3 through 3.6, which give the polynomial fit coefficients for the ramp filter parameters. The Table entries except for the first line are used as $parameter = A_0 + A_1 Y + A_2 Y^2 (+A_3 Y^3 \text{ for peak transmission})$. The short wavelength side of the filter is opposite for alternate ramps. The first line in each table gives Y position as a function of λ . If the polynomial fit predicts a , b , or $c < 0$ or > 1 then the quantities are set to 0 or 1 respectively.

Use of these fits should be restricted to objects on the center of the ramp ± 7.6 arcseconds or the beam will combine light from adjacent ramps. The fit should also not be used within 13 arcseconds of the end of the ramp. There is enough overlap between ramps that positions inside the measured positions will be used for complete wavelength coverage except at the extreme end of the lowest and highest wavelength ramp. Figure 3.2 shows the fit parameter T_0 as a function of λ_0 for all 16 ramp filter strips. Figure 3.3 shows $2H/\lambda_0$

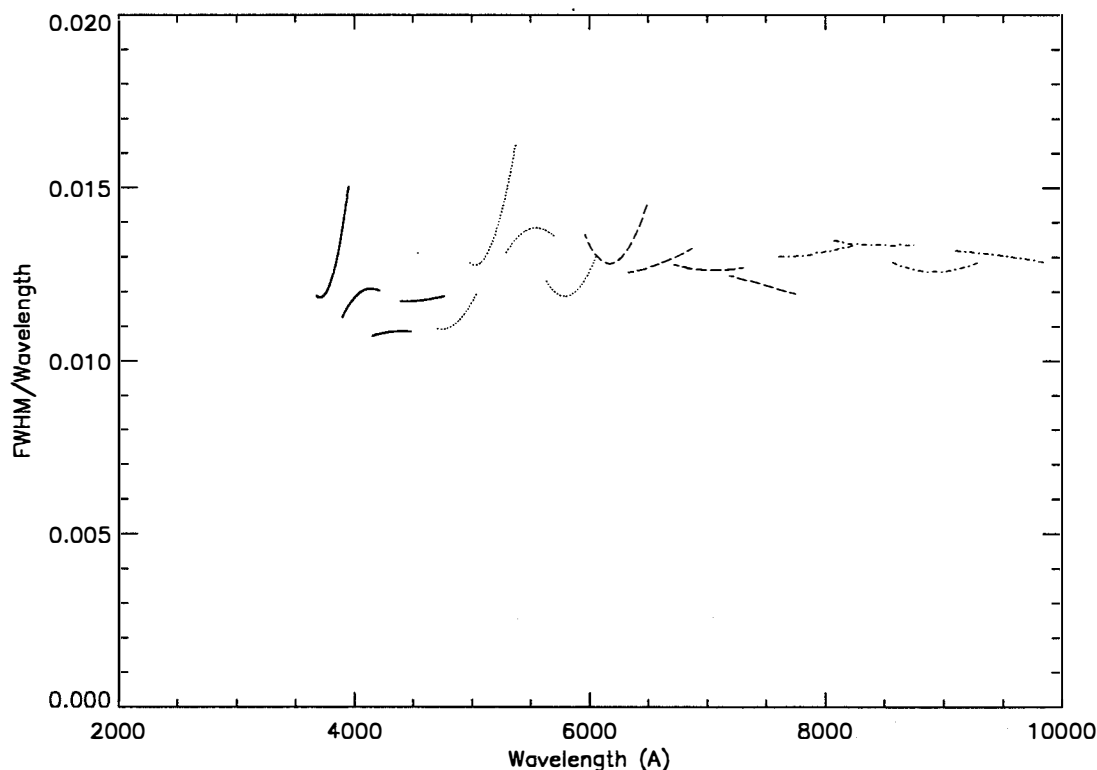


Figure 3.3 Ramp Filter Dimensionless Widths

Quantity	A0	A1	A2	A3
Ramp 1 Position	-29.38	.0089	.0000	
Wavelength	3657.7	138.7	.6178	
Peak transmission	-.01667	.2188	.04138	-.03489
Half width at half max	21.95	-.8347	2.143	
a	.2120	.002857	.002596	
b	1.181	-.8138	.3535	
c	.3301	-.3715	.3825	
Ramp 2 Position	-26.46	.0073	.0000	
Wavelength	3876.9	158.6	.5472	
Peak transmission	.1660	.2288	-.1080	.004005
Half width at half max	21.50	3.315	-.7079	
a	.1592	-.003687	-.0008497	
b	.7938	.2355	-.09124	
c	.9306	.01366	.007458	
Ramp 3 Position	-21.77	.0046	.0000	
Wavelength	4130.5	168.8	-.7389	
Peak transmission	.1352	.6200	-.5226	.1529
Half width at half max	22.09	1.306	-.1181	
a	.2300	.05586	-.03044	
b	1.096	-.3185	.1396	
c	1.276	-1.279	.5721	
Ramp 4 Position	-24.39	.0058	.0000	
Wavelength	4371.3	185.8	.2913	
Peak transmission	.3189	.1287	-.01160	-.001712
Half width at half max	25.62	1.015	.1161	
a	.3123	-.2055	.09535	
b	.9222	.1167	-.04673	
c	1.033	-.1356	.05660	

Table 3.3 Ramp Filter FR418N parameters Note that FR418N is the name of the optical element, but it is used as generic filter LRF together with a specified wavelength in a proposal.

Quantity	A0	A1	A2	A3
Ramp 1 Position	-21.77	.0037	.0000	
Wavelength	4677.7	177.3	-1.125	
Peak transmission	.5450	-.3612	.3623	-.1281
Half width at half max	25.67	.3168	.8873	
a	-.009839	.4644	-.2039	
b	.31511	.9473	-.4516	
c	-.3379	2.788	-1.346	
Ramp 2 Position	-26.79	.0058	.0000	
Wavelength	4948.4	199.2	.6484	
Peak transmission	.4546	.4188	-.5456	0.1548
Half width at half max	32.10	-1.204	3.171	
a	.1678	-.02726	.09521	
b	.9345	.1935	-.1224	
c	.9571	.02919	-.009393	
Ramp 3 Position	-19.98	.0030	.0000	
Wavelength	5257.3	217.9	-1.481	
Peak transmission	.4944	-.1714	.1890	-0.0631
Half width at half max	34.03	5.078	-1.347	
a	.3851	-.06264	.003163	
b	.5605	.6642	-.2751	
c	.9665	.05543	-.03654	
Ramp 4 Position	-23.27	.0038	.0000	
Wavelength	5596.9	220.9	-.6938	
Peak transmission	.5058	-.2715	.3203	-.1230
Half width at half max	35.06	-2.856	2.382	
a	.06553	.2253	-.08275	
b	1.043	-.1190	.02889	
c	1.162	-.4910	.2059	

Table 3.4 Ramp Filter FR533N parameters

Quantity	A0	A1	A2	A3
Ramp 1 Position	-22.57	.0039	.0000	
Wavelength	5916.0	269.4	.3460	
Peak transmission	.1198	1.005	-.4015	-.00162
Half width at half max	41.50	-5.873	4.038	
a	.1743	-.05050	.06481	
b	.8320	.3326	-.1858	
c	.9682	-.09110	.05122	
Ramp 2 Position	-24.16	.0041	.0000	
Wavelength	6290.8	275.6	.7184	
Peak transmission	.7918	-.02034	.1086	-.05945
Half width at half max	39.48	2.120	.3703	
a	.05596	.3034	-.1333	
b	1.017	-.27026	.04560	
c	.7244	.8326	-.5107	
Ramp 3 Position	-22.66	.0035	.0000	
Wavelength	6673.5	301.6	.3321	
Peak transmission	.9494	-1.008	1.161	-.3777
Half width at half max	42.81	.8193	.4269	
a	.1038	.09020	-.02747	
b	.8415	.3045	-.1930	
c	1.017	-.1732	.07463	
Ramp 4 Position	-24.05	.0033	.0000	
Wavelength	7141.9	289.3	-.2999	
Peak transmission	.4823	.4479	-.07484	-.05868
Half width at half max	44.72	.8952	-.0756	
a	.1612	-.01167	.01355	
b	.2708	1.077	-.4757	
c	.9941	-.02694	.01685	

Table 3.5 Ramp Filter FR680N parameters

Quantity	A0	A1	A2	A3
Ramp 1 Position	-26.76	.0040	.0000	
Wavelength	7555.5	320.4	1.906	
Peak transmission	.7524	-.3328	.4543	-.1343
Half width at half max	49.32	1.742	.4914	
a	.2958	-.3877	.2465	
b	1.321	-.9156	.3666	
c	.3762	1.668	-.9499	
Ramp 2 Position	-21.73	.0026	.0000	
Wavelength	8014.3	350.5	-.7500	
Peak transmission	.8204	-.3368	.3815	-.1057
Half width at half max	54.17	1.579	.2196	
a	.05832	.7525	-.3625	
b	.4582	.8433	-.4350	
c	.6422	.3247	-.1593	
Ramp 3 Position	-23.16	.0028	.0000	
Wavelength	8510.7	375.6	.3706	
Peak transmission	.5817	-.1920	.4517	-.1627
Half width at half max	55.19	-.7459	1.433	
a	.5422	-.2444	.03545	
b	1.420	-1.176	.4814	
c	.4257	-.2522	.1777	
Ramp 4 Position	-24.54	.0029	.0000	
Wavelength	9034.3	387.2	.8722	
Peak transmission	.6241	.2403	-.1230	.02829
Half width at half max	59.69	2.167	-.1996	
a	.2376	-.01879	-.00864	
b	.9670	.02456	-.00477	
c	.7829	.03750	.02393	

Table 3.6 Ramp Filter FR868N parameters

In Figure 3.4 we show the correspondence between central wavelength and location in the focal plane for the nominal filter positions. The selection of filter position and aperture for the ramp filters will be transparent to the user who is required merely to specify the ramp filter name LRF and a central wavelength for the observation. Each central wavelength will be assigned a unique aperture and filter wheel position. The provisional camera location of each central wavelength is shown in Table 3.7, which will be updated to reflect the exact coordinates of central wavelengths following the initial filter calibration during SLTV.

Filter Name	Wavelength range	CCD location	Filter Position	Comments
LRF	3700-3816	WF4	nominal	
LRF	3816-3932	WF2/WF3	-33 degrees	vignetting
LRF	3932-4056	WF2/WF3	-18 degrees	vignetting
LRF	4056-4179	WF4	nominal	
LRF	4179-4310	WF3	nominal	
LRF	4310-4441	WF2	nominal	
LRF	4441-4581	WF2	nominal	
LRF	4581-4720	WF3	nominal	
LRF	4720-4868	WF3	nominal	
LRF	4868-5016	WF2	nominal	
LRF	5016-5174	WF2	nominal	
LRF	5174-5331	WF3	nominal	
LRF	5331-5499	WF4	nominal	
LRF	5499-5666	WF2/WF3	-18 degrees	vignetting
LRF	5666-5844	WF2/WF3	-33 degrees	vignetting
LRF	5844-6022	WF4	nominal	
LRF	6022-6211	WF2	nominal	
LRF	6211-6400	WF3	nominal	
LRF	6400-6601	WF3	nominal	
LRF	6601-6802	WF2	nominal	
LRF	6802-7016	WF2/WF3	-18 degrees	vignetting
LRF	7016-7229	WF4	nominal	
LRF	7229-7456	WF4	nominal	
LRF	7456-7683	WF2/WF3	-33 degrees	vignetting
LRF	7683-7924	WF4	nominal	
LRF	7924-8165	WF2/WF3	-33 degrees	vignetting
LRF	8165-8422	WF2/WF3	-18 degrees	vignetting
LRF	8422-8678	WF4	nominal	
LRF	8678-8951	WF3	nominal	
LRF	8951-9223	WF2	nominal	
LRF	9223-9513	WF2	nominal	
LRF	9513-9802	WF3	nominal	

Table 3.7 Aperture Locations and Wavelengths for Ramp Filters.

Note that alternative configurations to those given in Table 3.7 for a given central wavelength are not permitted. The purpose of this constraint is to standardize the calibration requirements for these filters. Consequently, a given central wavelength will always correspond to a single location within the field of view.

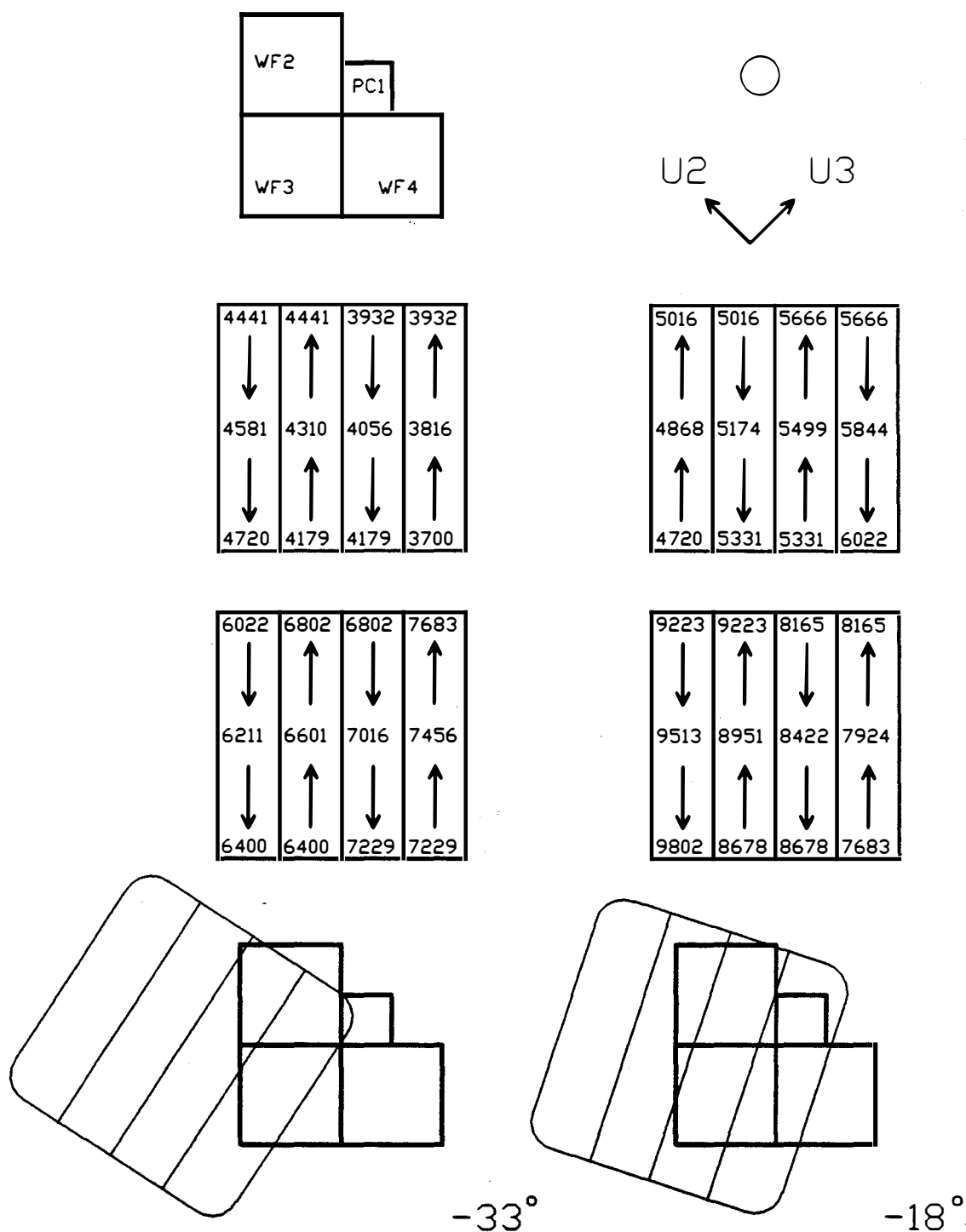


Figure 3.4 Ramp Filter Wavelength Mapping. A schematic showing the correspondence between the central wavelength and location at the focal plane for the nominal and rotated linear ramp filter positions. The circle shows the beam diameter at the filter, and can be used to assess vignetting.

3.2. REDSHIFTED [OII] QUAD FILTERS

The redshifted [OII] quad filter was designed to map onto a four faceted WFC configuration. A partial SOFA wheel rotation of -33 degrees is required to move filter quadrant 1 (3763Å) into WF2 and WF3, with some vignetting of both camera fields. The filter projections associated with the redshifted [OII] quad are shown schematically in Figure 3.5.

The nominal and rotated filter wheel positions for the redshifted [OII] quad filter are each associated with different filter names, in order to allow pipeline calibration and database retrievals to proceed smoothly. The specification for each filter name is summarized in Table 3.8 below.

Filter Name	FOV Location	Aperture name	Mean Wavelength	Effective Width	Comments
FQUVN	WF2	WF2	3986	114	Nominal filter wheel position
FQUVN	WF3	WF3	3916	90	Nominal filter wheel position
FQUVN	WF4	WF4	3839	90	Nominal filter wheel position
FQUVN33	WF2/WF3	FQUVN33	3763	88	Filter rotated -33 degrees

Table 3.8 Redshifted [OII] Quad Filter Elements

The required central wavelength is selected by filter name and aperture location. Filter element FQUVN has three possible apertures, each of which is nominally centered in one of the three WF channels and associated with a unique central wavelength, while the filter element FQUVN33 corresponds to a single central wavelength. In the proposal instructions a central wavelength is also requested, in addition to the filter name and aperture, to provide a consistency check. Aperture names are discussed further in Section 3.6.

3.3. POLARIZER QUAD FILTER

The polarizer quads were also designed to map onto a four faceted WFC configuration and, consequently, also require a partial filter wheel rotation of -33 degrees to move filter quadrant 1 (nominal polarization angle 135 degrees) into WFCs 2 and 3, with some vignetting of both camera fields. In this case, however, rotation changes the polarization angle to 102 degrees and so the 135 degree polarization angle is only available in the PC camera. The filter projections associated with the use of the polarizer quads are shown schematically in Figure 3.5. The nominal and rotated filter wheel positions for the polarizer quad are both associated with unique filter names which are summarized in Table 3.9 below.

Filter Name	FOV Location	Aperture name	Polarization Angle (degrees)	Comments
POLQ	PC1	PC1	135	Nominal filter wheel position
POLQ	WF2	WF2	0	Nominal filter wheel position
POLQ	WF3	WF3	45	Nominal filter wheel position
POLQ	WF4	WF4	90	Nominal filter wheel position
POLQN33	WF2/WF3	POLQN33	102	Filter wheel rotated -33 degrees

Table 3.9 Polarizer Quad Filter. Polarization angle 0 degrees lies along +X axis in Figure 1.1.

The required polarization angle is selected by filter name and aperture location. The transmission of the quad polarizer is shown in Figure 3.6. The polarizer is afocal and must therefore usually be used in combination with another filter which will largely define the shape of the passband.

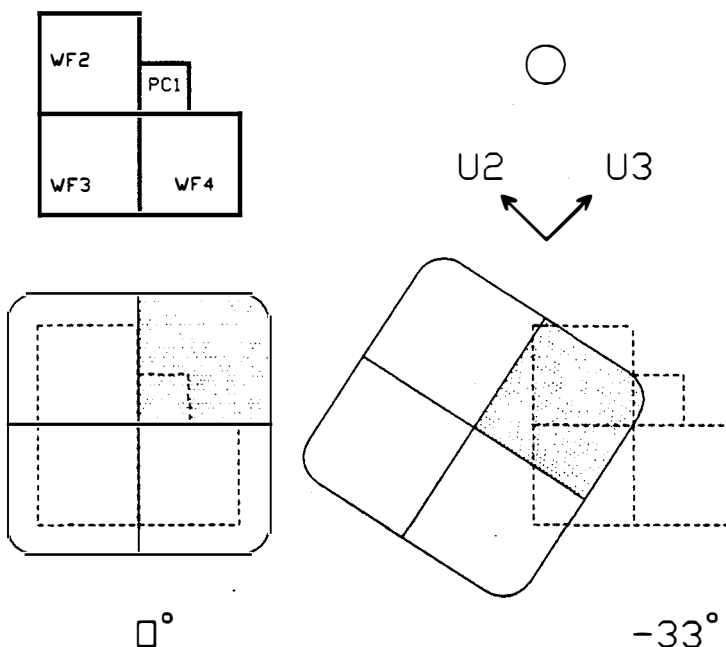


Figure 3.5 Redshifted [OII] and Polarizer Quads. A schematic showing the mapping to the focal plane for nominal and rotated (-33 degrees) SOFA positions. The circle shows the beam diameter at the filter, and can be used to assess the unvignetted field.

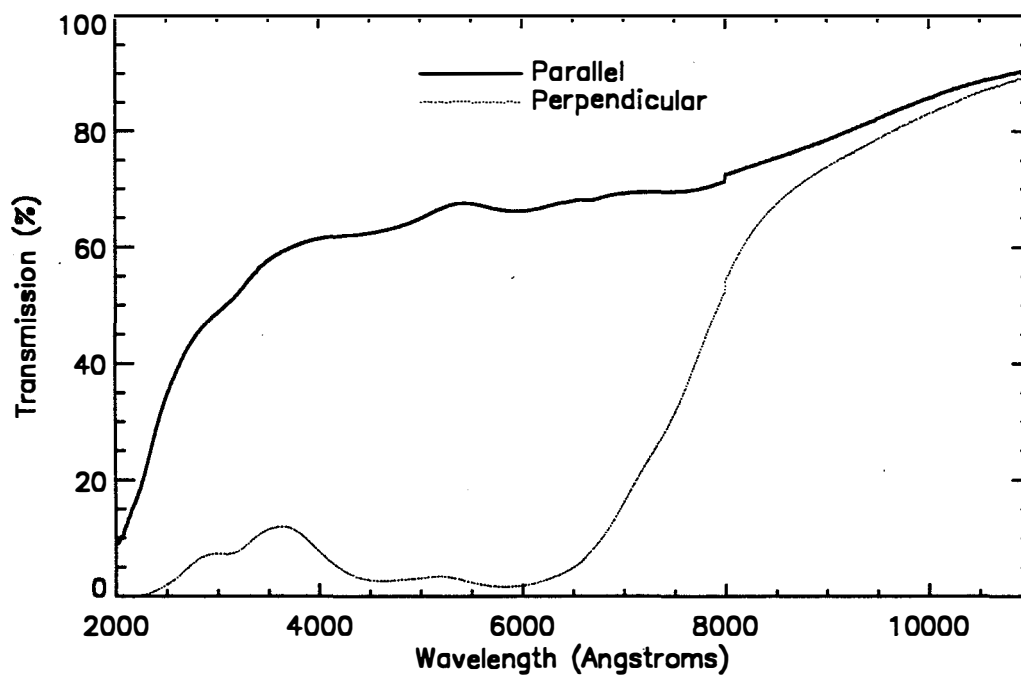


Figure 3.6 Polarizer Transmission for light polarized perpendicular (dotted curve) and parallel (solid curve) to the filter polarization direction.

3.4. METHANE QUAD

The methane band quad, known as the jewel-quad, was designed for a four faceted WF/PC configuration to permit imaging with both the WFCs and PCs. WF imaging is recovered for the first quadrant element of the filter (6193Å) by a partial SOFA wheel rotation of -33 degrees which moves quadrant 1 into WF2 and WF3 with some vignetting of both camera fields. PC imaging with all four elements of the methane band jewel-quad cannot be recovered, but partial SOFA wheel rotations of -15 and +15 degrees will be implemented to recover two of the four methane band filters (8929Å and 6193Å). The +15 degrees rotation of the filter wheel, however, results in some vignetting of PC1's field of view. The filter projections associated with the methane band jewel-quad are shown schematically in Figure 3.7. Each of the four filter wheel positions are associated with unique filter names as summarized in Table 3.10 below.

Filter Name	FOV Location	Aperture name	Mean Wavelength	Effective Width	Comments
FQCH4N	WF2	WF2	5433	38	Nominal filter position
FQCH4N	WF3	WF3	8929	64	Nominal filter position
FQCH4N	WF4	WF4	7274	51	Nominal filter position
FQCH4N33	WF2/WF3	FQCH4N33	6193	44	Filter rotated -33 degrees
FQCH4N15	PC1	FQCH4N15	6193	44	Filter rotated -15 degrees
FQCH4P15	PC1	FQCH4P15	8929	64	Filter rotated +15 degrees

Table 3.10 Methane Band Quad Filter

The required central wavelength is selected by filter name and aperture location. Filter element FQCH4N has three possible apertures, each of which is nominally centered in one of the three WF channels and associated with a unique central wavelength, while FQCH4N33 is associated with one possible central wavelength. FQCH4N15 and FQCH4P15 are both associated with one central wavelength for PC1 observations. In the proposal instructions a central wavelength is requested, in addition to the filter name and aperture, to provide a consistency check.

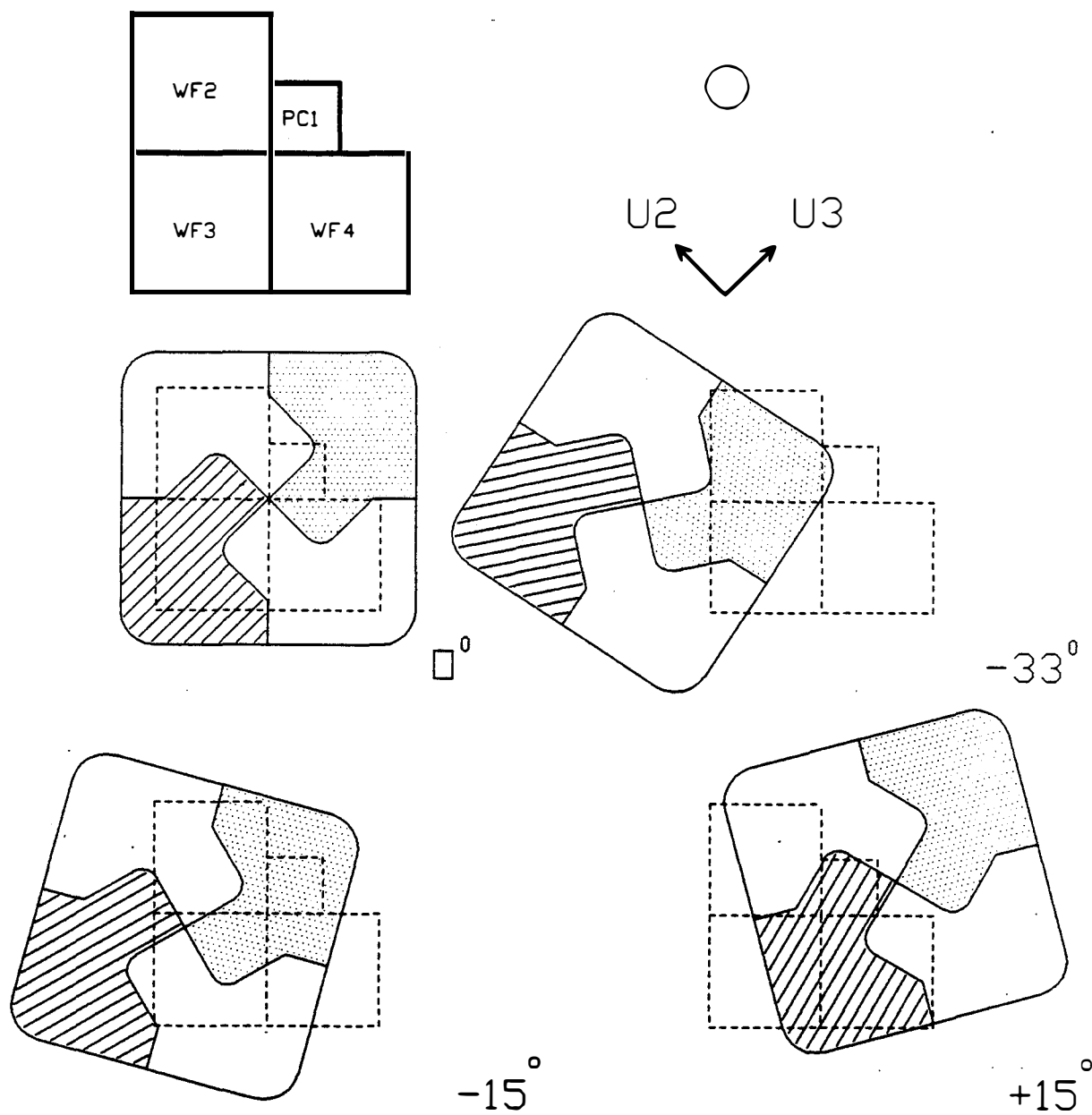


Figure 3.7 Methane Quad Filter. A schematic showing the mapping to the focal plane for nominal and rotated (-33, -15 and +15 degrees) SOFA positions. The circle indicates the beam diameter at the filter and can be used to assess the unvignetted field.

3.5. WOOD'S FILTERS

WFPC2 will feature two solar-blind, or Wood's filters, for FUV ($< 2000\text{\AA}$) imaging. It was shown by Wood in the 1930s (Physical Optics, 1949, R. W. Wood) that thin layers of alkali metals transmit FUV wavelengths while providing very efficient long wavelength blocking due to the plasma frequency of the free electrons. Wood's filters have been built for WFPC2 at JPL using thin (5000\AA) layers of sodium sandwiched between two MgF_2 substrates. These sodium-based Wood's filters have a broad bandpass from $1200\text{-}2100\text{\AA}$ with visible-light transmission lower than 10^{-8} . The best conventional UV filters exhibit visible-light transmission of 10^{-3} to 10^{-4} . Many astronomical objects emit 10^4 to 10^7 visible photons for every FUV photon. In such cases, a Wood's filter is essential for FUV imaging so that the visible light leak does not dominate the observation. The main problem experienced to date with Wood's filters is their long term stability. Sodium is a very reactive metal and attempts to passivate the sodium layer have met with limited success. It is possible that as the Wood's filters age pinholes will form which transmit visible light. This transmitted light will appear as an increase in the background level at the focal plane.

The Wood's filters can be used as a broadband filter or in combination with the CaF_2 longpass filter to suppress geocoronal emission or crossed with one of the other UV filters to define a solar-blind UV photometric system. As discussed at the beginning of this Chapter, the image will be out of focus in the last case. WFPC2's Wood's filters are circular with a clear aperture of 41 mm. The baseline plan is to mount two identical Wood's filters in SOFA wheel 1 to provide some redundancy.

In the nominal filter wheel position PC1 has a clear field of view but, there is significant vignetting in all three WFCs. A partial filter wheel rotation of -15 degrees produces a larger field of view in WF3, although some vignetting remains. The options are illustrated schematically in Figure 3.8. The imaging performance of the Wood's filters will be continually monitored for signs of ageing such as pinhole visible light leaks. Additional partial rotations could be implemented in the future to position an unaffected region of the filter into a WF or PC if necessary. The unvignetted filter projections associated with the two planned filter positions are shown schematically in Figure 3.8. Each filter position is associated with a unique name as summarized in

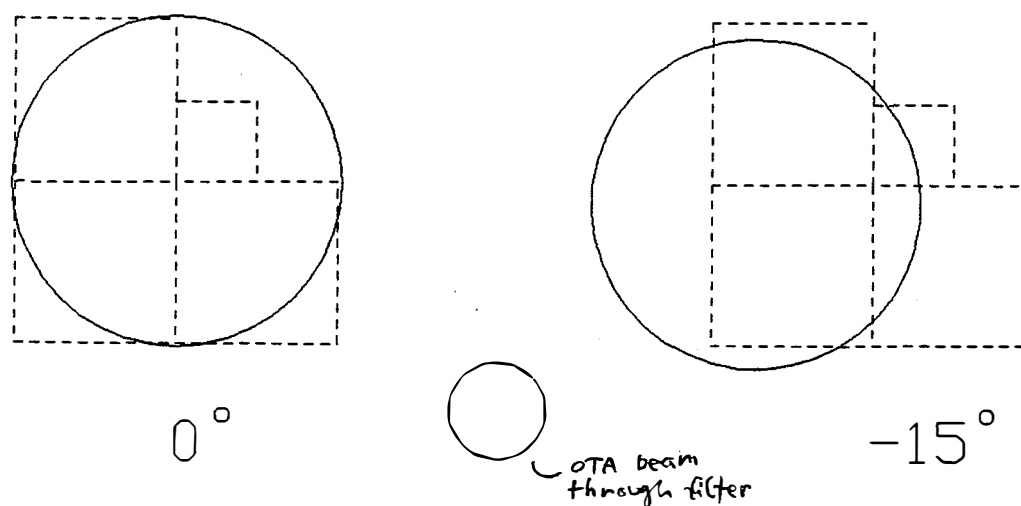


Figure 3.8 Wood's Filters. A schematic showing the mapping to the focal plane for nominal and rotated SOFA positions. The circle shows the beam diameter at the filter.

Table 3.11.

Filter Name	FOV Location	Aperture Name	Mean Wavelength	Effective Width	Comments
F160AW	PC1	PC1	1600	900	Nominal filter position
F160BW	PC1	PC1	1600	900	Nominal filter position
F160AN15	WF3	F160AN15	1600	900	Filter rotated -15 degrees
F160BN15	WF3	F160BN15	1600	900	Filter rotated -15 degrees

Table 3.11 Wood's Filters

The filter name required is selected on the basis of whether a PC or WF observation is required. The choice between filter A or B is arbitrary pending a full evaluation of the filters during SMOV. The two Wood's filters are often referred to generically as F160W in this handbook. We also document F157W (which is a WF/PC-1 filter with a redleak), which might replace one of the Wood's filters if they are not suitable for flight. It is not presently expected to be included.

3.6. APERTURES

The WFPC2 camera configuration and filter set require a substantial number of new apertures. A summary of all possible aperture/filter combinations is given in Table 3.12.

Each camera has an associated 'optimum' aperture within its field of view (FOV) close to the field center of the CCD. The present location for these apertures is the geometric center of each CCD at pixel (420,420) (after allowing for a 40 pixel overlap). These positions may be adjusted to reflect changes in CCD performance and will first be reviewed following SLTV. The aperture designations are WF2, WF3, WF4 and PC1 for the individual cameras and WFA11 for the three WFC combination. WFA11 is located close to the apex in WF3 (see Figure 1.1). Observers are expected to place small or unresolved targets on these apertures.

In cases where the user does not want to use the current 'optimum' centers, a complimentary set of apertures has been implemented specifically for this purpose. These locations remain fixed and correspond to the geometric center of each camera within each field of view. They are designated WF1-FIX, WF2-FIX, WF3-FIX, PC1-FIX and WFA11-FIX. Observers are expected to place extended targets on these apertures.

An additional set of aperture names have been defined for use with the WFPC2 filters which require partial rotations. The characteristics and uses of these filters are discussed earlier in this Chapter. **It is possible that partial filter rotation will not be fully implemented for GO use in time for the start of Cycle 4 observations.** Please contact the Instrument Scientists for the latest information. Apertures which may be affected by this are listed as class 2 in Table 3.12. In the nominal filter position, the three WFC segments of the [OII], Methane and Polarizer quad filters can be selected with an aperture for each camera corresponding to the optimum or geometric camera centers. The partially rotated quad filters, which generally fall into more than one camera, have been assigned apertures in the camera which provides the largest clear aperture. The pixel coordinates of these apertures will be reviewed on a regular basis to reflect changes in CCD and filter cosmetics. There are no analogous fixed apertures for the partially rotated filter configurations. The aperture name is generally the same as the (rotated) filter name. For the Wood's filters, the nominal filter position is used for the PC1 FOV only, while the rotated filter position used for WFC observations. The linear ramp filters are unique because an aperture name is not required, since the ultimate location of the target will be determined from the central wavelength specified.

Class	Aperture Name	Filter	Aperture Location	Aperture Coordinates
1	PC1	n/a	optimum center PC1	445,445
1	WF2	n/a	optimum center WF2	420,420
1	WF3	n/a	optimum center WF3	420,420
1	WF4	n/a	optimum center WF4	420,420
1	WFALL	n/a	optimum apex WF3	110,110
1	PC1-FIX	n/a	geometric center PC1	445,445
1	WF2-FIX	n/a	geometric center WF2	420,420
1	WF3-FIX	n/a	geometric center WF3	420,420
1	WF4-FIX	n/a	geometric center WF4	420,420
1	WFALL-FIX	n/a	near apex WF3	110,110
1	WF2	FQUVN	optimum center WF2	420,420
1	WF3	FQUVN	optimum center WF3	420,420
1	WF4	FQUVN	optimum center WF4	420,420
1	WF2-FIX	FQUVN	geometric center WF2	420,420
1	WF3-FIX	FQUVN	geometric center WF3	420,420
1	WF4-FIX	FQUVN	geometric center WF4	420,420
2	FQUVN33	FQUVN33	optimum location WF2	264,416
1	WF2	POLQ	optimum center WF2	420,420
1	WF3	POLQ	optimum center WF3	420,420
1	WF4	POLQ	optimum center WF4	420,420
1	WF2-FIX	POLQ	geometric center WF2	420,420
1	WF3-FIX	POLQ	geometric center WF3	420,420
1	WF4-FIX	POLQ	geometric center WF4	420,420
2	POLQN33	POLQN33	optimum location WF2	264,416
1	WF2	FQCH4N	optimum center WF2	420,420
1	WF3	FQCH4N	optimum center WF3	420,420
1	WF4	FQCH4N	optimum center WF4	420,420
1	WF2-FIX	FQCH4N	geometric center WF2	420,420
1	WF3-FIX	FQCH4N	geometric center WF3	420,420
1	WF4-FIX	FQCH4N	geometric center WF4	420,420
2	FQCH4N33	FQCH4N33	optimum location WF2	350,250
2	FQCH4N15	FQCH4N15	optimum location PC1	445,445
2	FQCH4P15	FQCH4P15	optimum location PC1	200,200
1	PC1	F160AW	optimum center PC1	445,445
1	PC1	F160BW	optimum center PC1	445,445
1	PC1-FIX	F160AW	geometric center PC1	445,445
1	PC1-FIX	F160BW	geometric center PC1	445,445
2	F160AN15	F160AN15	optimum location WF3	420,400
2	F160BN15	F160BN15	optimum location WF3	420,400
2	LRF	LRF	defined by wavelength	

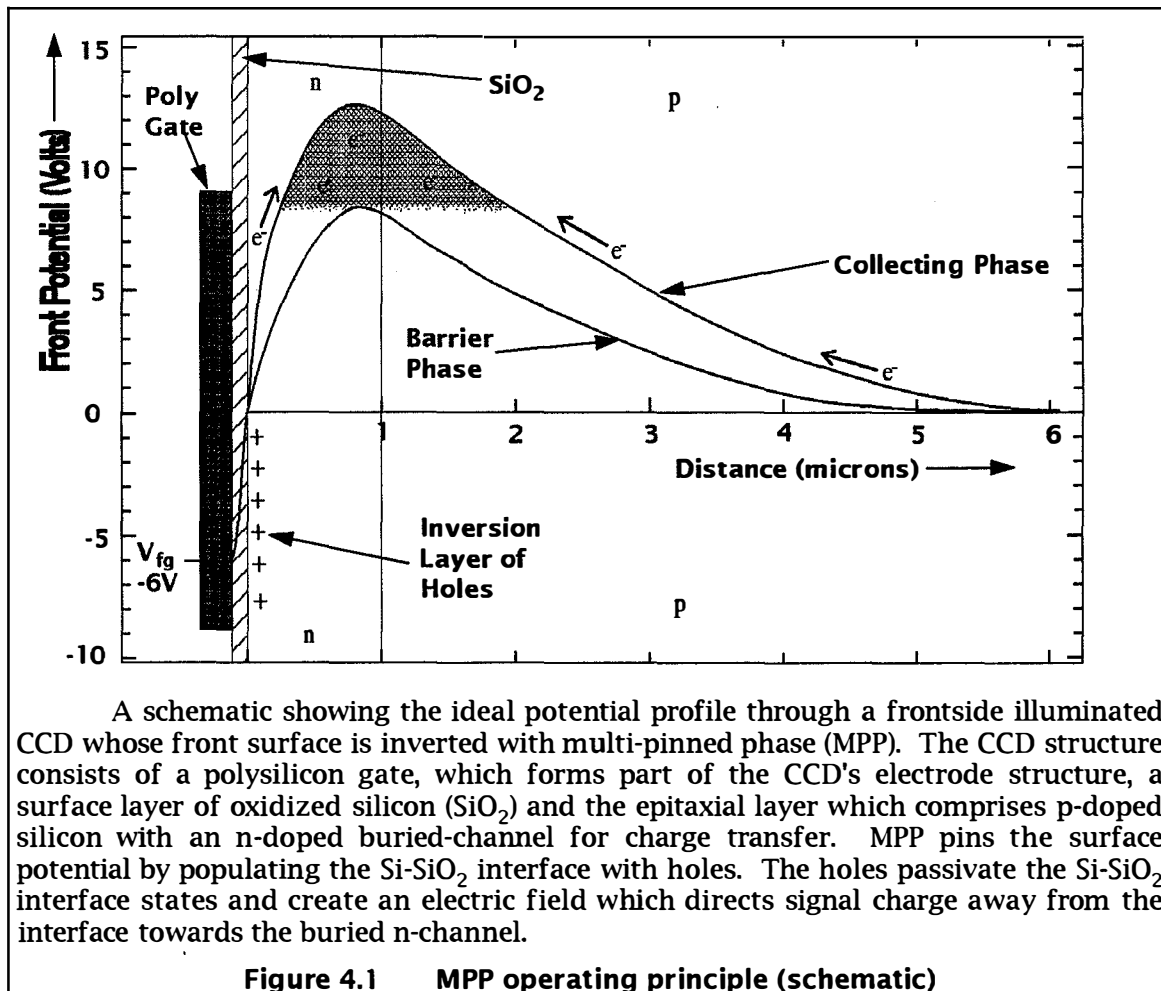
Table 3.12 *Summary of preliminary aperture definitions. The coordinate system is (row,column) pixel numbers for the camera in use (see Figure 1.1).*

4. CCD PERFORMANCE

4.1. INTRODUCTION

It was originally intended that the WFPC2 CCDs would be Texas Instruments (TI) 800×800 CCDs, with Platinum bias gate electrodes to address the problem of quantum efficiency hysteresis (QEH). Subsequently, due to the limited availability of flight quality devices it was decided to design and fabricate a new CCD, based on the TI format, at Loral (formerly Ford Aerospace).

The WFPC2 CCDs are thick, front-side illuminated devices with a format of 800×800, 15×15 μm pixels. They are three-phase devices employing a recent CCD innovation, multi-pinned phase (MPP). MPP allows CCD exposure with the total inversion of all phases so that the Si-SiO₂ interface, at the surface of the CCD, can be pinned at the substrate potential, directing signal charge away from the Si-SiO₂ interface states towards the buried n-channel. Figure 4.1 shows a schematic which illustrates the principle of MPP (modified from Janesick et al. 1989). The frontside Si-SiO₂ interface significantly affects the performance of CCDs, so MPP operation yields many practical benefits including, reduced dark noise, optimal charge transfer efficiency (CTE), rapid removal of residual images, excellent pixel-to-pixel uniformity and improved radiation hardness. MPP technology has been demonstrated and characterized in both Loral (Janesick et al. 1989) and Tektronix devices (Woodgate et al. 1989). The CCD sensors



for WFPC2 were manufactured by Loral in 1991 and processed and packaged for flight at JPL.

WF/PC-1 CCDs are thinned and 'back' illuminated, meaning that the active silicon layer is a free-standing membrane somewhat less than $10\mu\text{m}$ thick, with photons impinging directly on the silicon layer without attenuation in the polysilicon gate structure built on the other ('front') side of the device. On the other hand, the Loral CCDs are illuminated from the 'front' surface, i.e. the light passes through the polysilicon gate structure overlying the $10\mu\text{m}$ thick active silicon layer. Because the WFPC2 devices are frontside illuminated and supported by a bulk silicon substrate the CCD surface is flat, which is expected to reduce uncertainties in astrometric calibrations to about the 1/10 pixel level.

4.2. CCD CHARACTERISTICS

In this section the performance characteristics of the WFPC2 CCDs are reviewed and compared to the WF/PC-1 devices. In order to facilitate a rapid comparison a summary of device characteristics is presented in Table 4.1.

PARAMETER	WF/PC-1	WFPC2
Device	TI	Loral
Architecture	Thinned	Thick
Illumination	Backside	Frontside
Format	800×800	800×800
Pixel size	$15\mu\text{m}^2$	$15\mu\text{m}^2$
UV Phosphor	Coronene	Lumogen
Dark noise	$0.03\text{ e}^-/\text{pixel/s}(-87^\circ)$	$0.01\text{ e}^-/\text{pixel/s}(-80^\circ)$
Read noise	13 e^- RMS	7 e^- RMS
Linear Full well (e^-)	$\sim 40000\text{ e}^-$	$\sim 70000\text{ e}^-$
Gain	$8\text{ e}^-/\text{DN}$	$7\text{ e}^-/\text{DN}$ or $15\text{ e}^-/\text{DN}$
ADC range	12 bits (4096 DN)	12 bits (4096 DN)
QE 6000Å	50%	35%
QE 2500Å	12%	15%
WFC resolution	0.10 arcsec/pixel	0.10 arcsec/pixel
PC resolution	0.043 arcsec/pixel	0.046 arcsec/pixel

Table 4.1 Comparison Between WF/PC-1 and WFPC2 CCDs

4.2.1. Quantum Efficiency

The Loral CCDs are thick, frontside illuminated devices and so their intrinsic QE is lower than thinned, backside-illuminated CCDs due to the absorption of some incident light by the polysilicon electrode structure on the frontside surface of the CCD. The phosphor coating, which converts UV light into the visual range, also produces an enhancement of DQE at visual wavelengths since it acts as an anti-reflection coating

The WF/PC-1 devices are overcoated with a coronene phosphor, which converts photons shortward of 3600\AA to longer wavelengths where the CCD DQE is high. The flat field appearance of the WF/PC-1 CCDs results from local variations in membrane thickness, and variations in thickness of residual inactive silicon and the electrostatic charge state at the back surface. A massive UV (2500\AA) flood followed by maintenance of a continuous cold temperature is required to stabilize the backside charge state and QE of the WF/PC-1 CCDs. The QE instability is most pronounced in B band images.

In the WFPC2 devices, the front surface is overcoated with a lumogen phosphor, which serves as the primary detection medium for photons shortward of about 4800\AA , down-converting these to $5100\text{-}5800\text{\AA}$. The QE of the Loral devices is stable without

maintenance, hence the UV flood is unnecessary. Lumogen typically yields gains in DQE of 2-2.5 over the WF/PC-1 coronene phosphor for a given CCD. Its long wavelength cutoff (4800Å) is also better matched to a CCD's intrinsic sensitivity. The QE of the four flight WFPC2 CCDs is shown in Figure 4.2 and shows the uniform UV response of 10-15% and a peak optical QE of 40%.

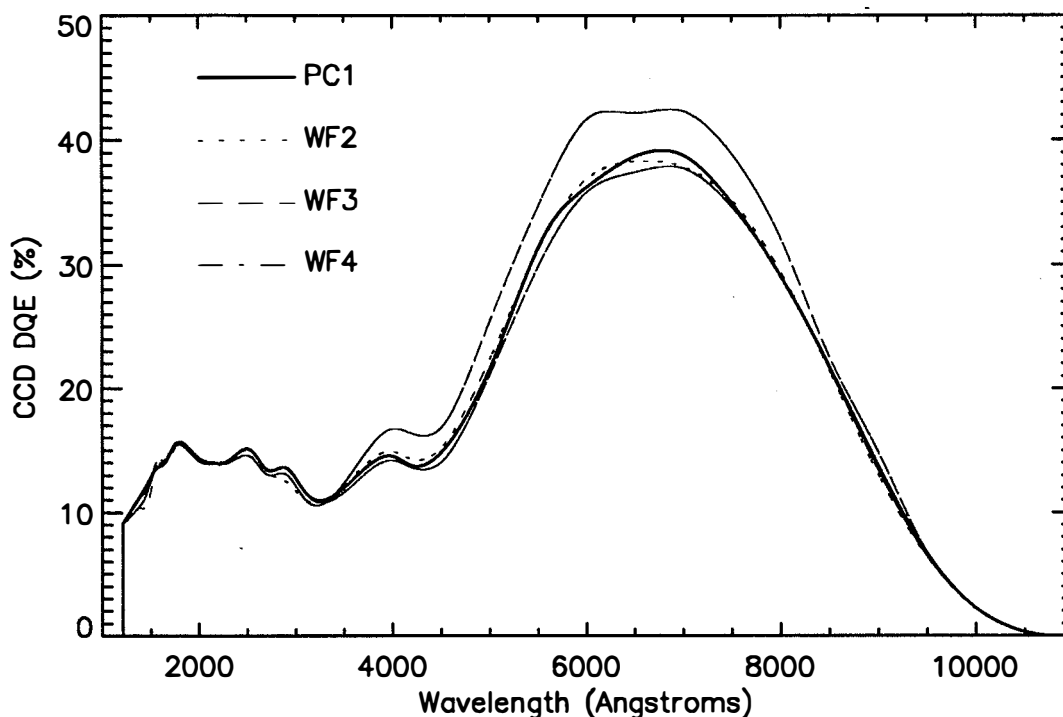


Figure 4.2 WFPC2 Flight CCD DQE

4.2.2. Dynamic Range

Linear full well capacity for these devices, clocked appropriately for the MPP mode, is approximately $70000e^-/\text{pixel}$. The full well capacity of the WF/PC-1 CCDs is about $40000e^-$, but signal level is set in practice by the system gain of $7e^-/\text{DN}$ and the ADC resolution of 12 bits giving ADC saturation at $30000e^-$. Flight qualified ADC with higher dynamic range (>12 bits) were not available so WFPC2 will operate the two available ADCs with different gain factors. One channel will have a gain of $14e^-/\text{DN}$, which significantly undersamples the CCD read noise ($7e^- \text{ RMS}/\text{pixel}$) and gives a digital full well of about $60000e^-$. The other channel will have a gain of $7e^-/\text{DN}$, which is comparable to the CCD read noise and saturates at about $30000e^-$. The choice of gain factor will be determined by the scientific objective. The $7e^-/\text{DN}$ channel is best suited to faint object and UV imaging, where the lower CCD read noise will be most effective. For example it should be used for UV imaging of planets or narrowband imaging of high redshift galaxies. The $14e^-/\text{DN}$ channel has slightly higher effective read noise due to the quantization granularity but can be used for programs where a signal level in excess of $30000e^-$ is required. Even when imaging faint sources, it may be desirable to retain the high signal to noise information on brighter field stars as a PSF reference.

4.2.3. Blooming

Blooming up and down a CCD column occurs when more than about $100000e^-$ (the full well capacity) are collected in any pixel. When the pixel is full, the charge will flow into the next pixels along the column, and so on. The orientation of the bloomed

column(s) on the sky depends on the read-out direction of the particular CCD (see Figure 1.1) and the roll angle of the spacecraft.

Extreme overexposure of the Loral CCDs is not believed to cause any permanent effects and therefore the WFPC2 does not have any bright object limits other than those imposed by the HST as a whole.

The WFPC2 CCDs can be operated in a non-standard mode during the integration phase of an exposure in order to limit the blooming to only those columns containing the bright sources. This is accomplished by operating the serial transfer register clocks during the integration. This will result in an enhanced dark current rate over much of the CCDs and is only necessary for overexposures expected to have signal levels of a few $\times 10^7$ electrons within a single column. This mode is only possible for exposure times greater than 1 second.

4.2.4. Residual Image

Residual images in the WF/PC-1 CCDs occur when the full well capacity is exceeded, causing electrons to become trapped at the backside Si-SiO₂ surface interface. Trapped charge is slowly released over a period of time ranging from minutes to several hours, giving rise to residual images. A similar phenomenon, associated with the frontside Si-SiO₂ surface interface, is seen with frontside-illuminated CCDs. Inverted phase operation (MPP) allows holes to recombine with the trapped electrons at the frontside interface and so residual images dissipate very rapidly, on a timescale of minutes.

A second potential source of residual images, which occurs only in frontside-illuminated CCDs, is known as residual bulk image (RBI). Long wavelength photons can penetrate deeply enough to produce charge in the substrate. Most of this charge recombines rapidly (due to short carrier lifetimes) but some may diffuse into the epitaxial layer where it can become trapped in epitaxial interface states. Residual images can occur as this charge is slowly released during an exposure. RBI is temperature sensitive since the bulk trapping time constants decrease with increasing temperature. The WFPC2 CCDs do exhibit RBI, but at -70°C trapped charge rapidly escapes so that residual images disappear within 1000 seconds. Driven by the WFPC2 electronics, the CCDs recover quickly from a large overexposures (100 times full well or more), showing no measurable residual images a half hour after the overexposure.

4.2.5. Quantum Efficiency Hysteresis

The problem of quantum efficiency hysteresis (QEH) due to backside charge accumulation has been reviewed in detail by Griffiths et al. (1989) and Janesick and Elliot (1991). QEH should not be present in the Loral CCDs because they are frontside illuminated and incorporate MPP operation, and this has been verified in component tests at JPL. The absence of QEH means that the devices do not need to be UV-flooded as for WF/PC-1 and so decontamination procedures can be planned without the constraint of maintaining the UV-flood.

4.2.6. Flat Field

The flat field response is uniform within a few percent, with the exception of a manufacturing pattern defect which generates a 3% reduction in QE once every 34 rows. This pattern defect is identical in all CCDs, and also creates an astrometric offset of approximately 3% of the pixel height (0.003 arcsec in the WFCs) every 34 rows. More precisely, there was a 0.5 μ m overlap between adjacent 1024 \times 0.5 μ m raster scans during

the construction of the masks used to fabricate the chips. Photometry of point sources imaged onto these defects will be affected, and it will be better to correct flat fields for these rows for such applications. WFPC2 flat fields will also include instrumental effects, such as vignetting and shadowing by dust particles, and will not be available until the completion of SLTV and on orbit calibrations.

The accuracy of flat fielding is currently one of the major limiting factors in the photometric calibration of scientific observations with WF/PC-1. The WFPC2 CCDs have intrinsically uniform flat field response since they are not thinned, so there are no large scale chip non-uniformities resulting from the thinning process. MPP operation also improves pixel-pixel uniformity because charge transfer is driven deep into the buried n-channel away from the influence of Si-SiO₂ interface states. The WFPC2 CCD flat fields show an overall pixel-to-pixel response having <2% non-uniformity. Figure 4.3 shows a portion of a WFPC2 CCD flat field obtained during quantum efficiency measurements at JPL. The image illustrates the excellent pixel to pixel uniformity of the Loral devices. The 34 row defect is clearly visible, and its amplitude of 3% serves to calibrate the grey scale.

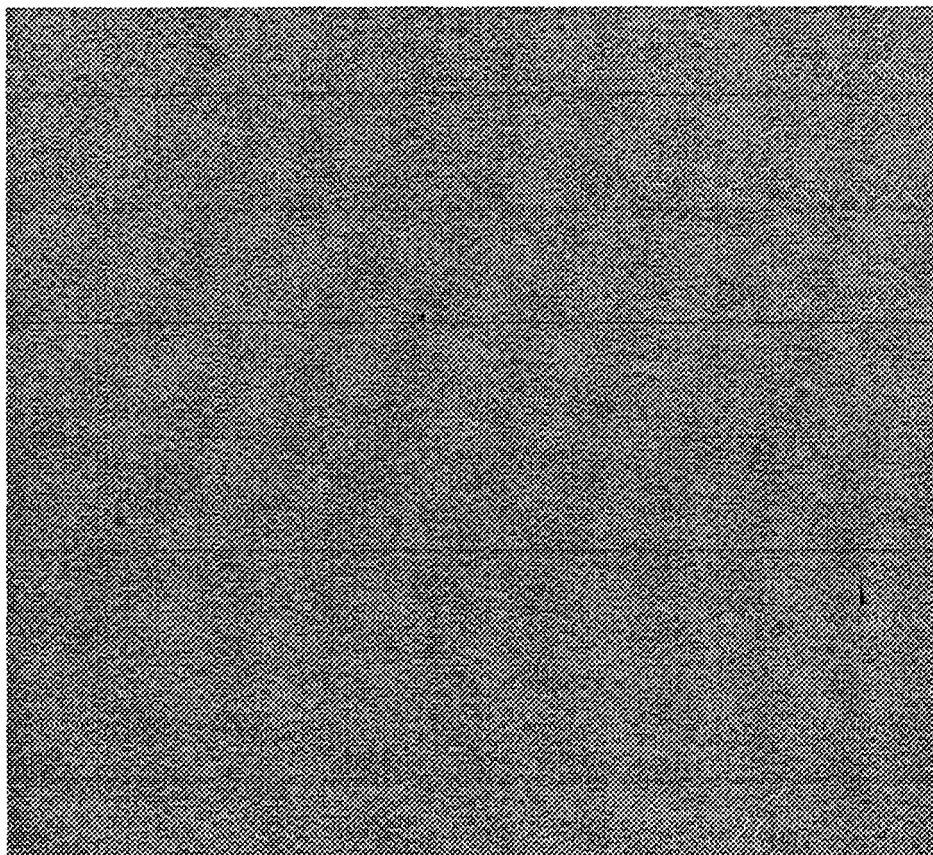


Figure 4.3 WFPC2 CCD Flat Field

4.2.7. Dark Noise

A reduction in dark noise is one of the benefits of MPP, since inverted phase operation suppresses the dominant source of CCD dark noise production (Si-SiO₂ surface states). The remaining source of dark noise, thermal generation in the silicon bulk, is determined by the quality of the silicon used in chip fabrication. The dark noise of WFPC2 CCDs is typically <0.01e⁻/pixel/second at -80°C, compared to 0.03e⁻/pixel/second at -88°C for the WF/PC-1 detectors.

The main impact of the Loral CCDs on the instruments UV capability is their ability to operate at higher temperatures, reducing the rate of condensation of contaminants on the CCD window. The new temperature setpoints for the WFPC2 TEC coolers are -90, -83, -77, -70, -50, -40, -30 and -20°C.

Approximate dark noise rates for the latter five setpoints are given in Table 4.2

Temperature (°C)	Dark noise (Counts/s/pixel)
-20	10.0
-30	3.0
-40	1.0
-50	0.3
-70	0.02

Table 4.2 CCD Dark Count Rates

It is also possible to perform ambient-temperature imaging which will allow the CCDs to be used for evaluation of the internal instrument alignment during thermal vacuum testing, ground activities prior to launch and the coarse optical alignment phase during SMOV. General Observers cannot command setpoint changes. The detectors are expected to be normally operated at -70°C.

4.2.8. Cosmic Rays

HST is subjected to cosmic rays and protons from the earth's radiation belts. The cosmic ray signature in the Loral CCDs is essentially the same as seen in the WF/PC-1 devices. Electron-hole pairs generated in the substrate by cosmic rays (and infrared photons) are efficiently removed by recombination in the low resistivity substrate material, and electrons do not diffuse efficiently up to the collecting phase.

Due to the finite thickness of the CCD detectors, cosmic ray events often deposit significant quantities of charge in more than one pixel. At low count levels the cosmic ray events become undetectable in the read-noise. A count of rate of cosmic ray events implies that an event threshold is used. Several cases are analyzed in the WF/PC-1 IDT OV/SV Report. Rates of 4.7 pixels/second/CCD above a threshold of 9 DN and 3.2 pixels/second/CCD above 20 DN were present. At these levels an average of 2.7 and 1.88 pixels, respectively, were involved in each event. This yields an event rate of 1.7 events/second/CCD.

Cosmic ray events will impact scientific imaging differently with WFPC2 in two ways. Firstly, the WFPC2 CCDs have an epitaxial thickness of about 10 μm , compared to 8 μm for the thinned WF/PC-1 device, and a recombination length of 8-10 μm in the substrate. WFPC2 CCDs also have lower read noise and so the number of cosmic ray events will consequently, differ from that of the WF/PC-1 CCDs, since the low amplitude tails will be detected. In practice, this means that the number of pixels apparently contaminated by cosmic rays in an image will be higher in WFPC2, although the underlying event rate is similar to that experienced in WF/PC-1.

Secondly, the implementation of corrective optics in WFPC2 means that stellar images will be undersampled and much more difficult to separate from cosmic rays, as is shown in Figure 4.4 which compares the predicted WFPC2 point spread functions with cosmic ray images from a WF/PC-1 image. Long science observations will usually have to be broken into at least two exposures (CR-SPLIT) to ensure that cosmic ray events can be identified.

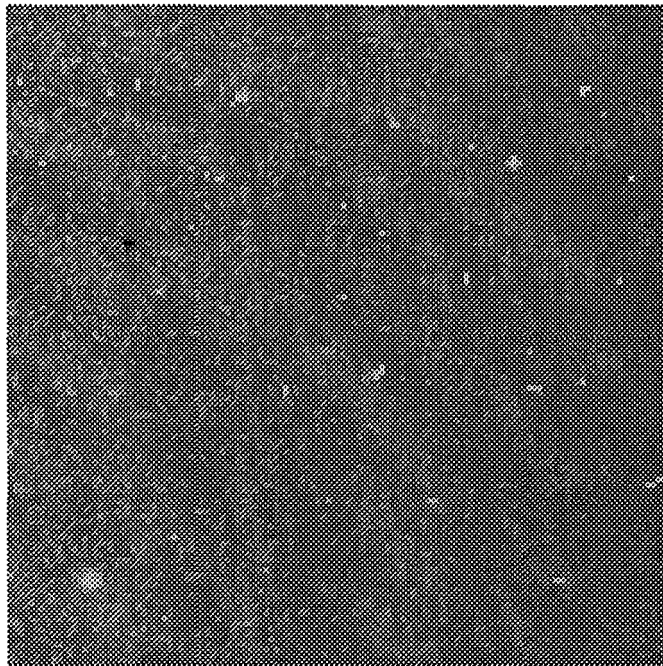


Figure 4.4 Comparison of PSF and Cosmic Ray Events (schematic) A simulation in which suitably scaled WF point spread functions (PSFs), have been inserted into a section of an internal flat field image obtained with WF/PC-1.

4.2.9. Radiation Damage

In low earth orbit (LEO) the CCDs will be subject to radiation damage from the earth's radiation belts. The WFPC CCDs are shielded from energetic electrons, and about half the incident energetic protons. Long term radiation damage to the CCDs from high energy protons leads to an increase in dark count rate (mainly from the creation of hot pixels), baseline shifts in the CCD amplifiers and long term degradation of CTE. In the case of WF/PC-1 a long term dark frame program is monitoring the increase in the number of hot pixels (which is about 30/CCD/month). There has not been a significant degradation in the amplifier baselines since launch. One of the major radiation damage mechanisms is the creation of new Si-SiO₂ interface states which causes increased dark noise. In the MPP CCD these states immediately recombine with holes reducing the gradual increase in dark noise by factors of ~25 compared to normal three-phase CCDs (Woodgate et al. 1989, Janesick et al. 1989b).

4.2.10. Charge Transfer Efficiency

The WF/PC-1 CCDs exhibit low-level non-linearity, known as deferred charge, mainly due to charge traps in the CCD transfer gate, a design fault discussed by Janesick and Elliot (1991) and Griffiths, et al. (1989). In practice low signal levels (<250 e⁻) are effectively smeared over several pixels during transfer. Rectification of the problem requires a preflash exposure (40e⁻ pedestal) prior to the majority of science observations, increasing the read noise and adding to the overhead time associated with an exposure.

There are no significant deferred charge problems, in the WFPC2 CCDs. Typically 3-4 low level traps may be present over whole CCD area but they account for a negligible amount of deferred charge (<200e⁻ total). The absence of a deferred charge

problem means that preflash exposures will not be required. Typical charge transfer efficiency is 0.99995 in flight devices.

4.2.11. Read Noise and Gain Settings

The CCDs and their associated signal chains have read-out noise levels (in the absence of signal shot noise or interference) of approximately $7e^-$. The WF/PC-1 CCD read noise is effectively $15-20e^-$, since there are additional contributions above the nominal $13e^-$ resulting from "missing codes" in the ADC and the preflash exposure.

The conversion factors from detected electrons ($QE \times$ number of incident photons) to data numbers (DN) are as tabulated in Table 4.3 from JPL memos DFM 1973 (11 Aug 1992) and DFM 2023 (14 Dec 1992):

Camera	ATD-GAIN=7 (e^-/DN)	ATD-GAIN=15 (e^-/DN)
PC1	7.1	14.3
WF2	7.3	14.7
WF3	7.0	14.2
WF4	7.1	14.3

Table 4.3 Signal Chain Gains

4.2.12. CCD Electronics

The CCD camera electronics system are essentially the same design flown on WF/PC-1 with the exception of changes made to implement the different clock pattern for MPP inverted phase operation. Changes in circuit timing have also been made to correct the problem of ADC conversion errors (Lauer 1991).

4.3. REFERENCES

1. Groth, E. and Shaya, E., 1991, in *Wide Field/Planetary Camera Final Orbital/Science Verification Report*, S., M., Faber, Ed.
2. Griffiths, R. Ewald, S. and Mackenty, J. W., in *CCDs in Astronomy*, P.A.S.P. 8, 231, G. Jacoby, ed. (1989)
3. Janesick, J., Elliot, T., Bredthauer, R., Cover, J., Schaefer, R. and Varian, R., in *Optical Sensors and Electronic Photography*, SPIE Proc. 1071 (1989).
4. Janesick, J., Elliot, T., Blouke, M. and Corrie, B., 1989b, in *Optical Sensors and Electronic Photography*, SPIE Proc. 1071, 115 Blouke, D. Pophal, Ed. (1989)
5. Blouke, D. Pophal, Eds. 153. Janesick, J. and Elliot, T., 1991, in P.A.S.P. 8
6. Lauer, T., E., in *Wide Field/Planetary Camera Final Orbital/Science Verification Report*, S., M., Faber, Ed. (1991)
7. Trauger, J. T., in *CCDs in Astronomy*, P.A.S.P. 8, 217, G. Jacoby, ed., (1989).
8. Woodgate, B. E., in *CCDs in Astronomy*, P.A.S.P. 8, 237 G. Jacoby, ed., (1989)

5. POINT SPREAD FUNCTION

5.1. EFFECTS OF OTA SPHERICAL ABERRATION

The OTA spherical aberration produces the Point Spread Function (PSF - the apparent surface brightness profile of a point source), observed by the WF/PC-1. Briefly, the fraction of the light within the central 0.1 arcsecond is reduced by a factor of about 5. The resulting PSF has "wings" which extend to large radii (several arcseconds), greatly reducing the contrast of the images and degrading the measurements of sources near bright objects or in crowded fields. Burrows et al. (1991, Ap. J. Lett. 369, L21) provide a more complete description of the present HST PSF. Figure 5.1 shows the PSF in three cases. It shows the present HST PSF, the projected PSF after the WFPC2 is installed, and for comparison the PSF that would be obtained from a long integration if HST were installed at a ground based observatory with one arcsecond seeing. All the PSFs were computed at 4000Å. The FWHM of the image both before and after the installation of WFPC2 is approximately proportional to wavelength but the WF/PC-1 core is approximately 50% broader than that predicted for WFPC2. Figure 5.2 shows the encircled energy (EE), the proportion of the total energy from a point source within a given radius of the image center, for the same three cases. It can be seen that the core of the image in WFPC2 will contain most of the light and will satisfy the original Level 1 specification for HST which calls for 70% of the energy from a point source to fall within a radius of 0.1 arc seconds (WF/PC-1 has about 15%). There is an improvement of 2 magnitudes in limiting magnitude when background limited.

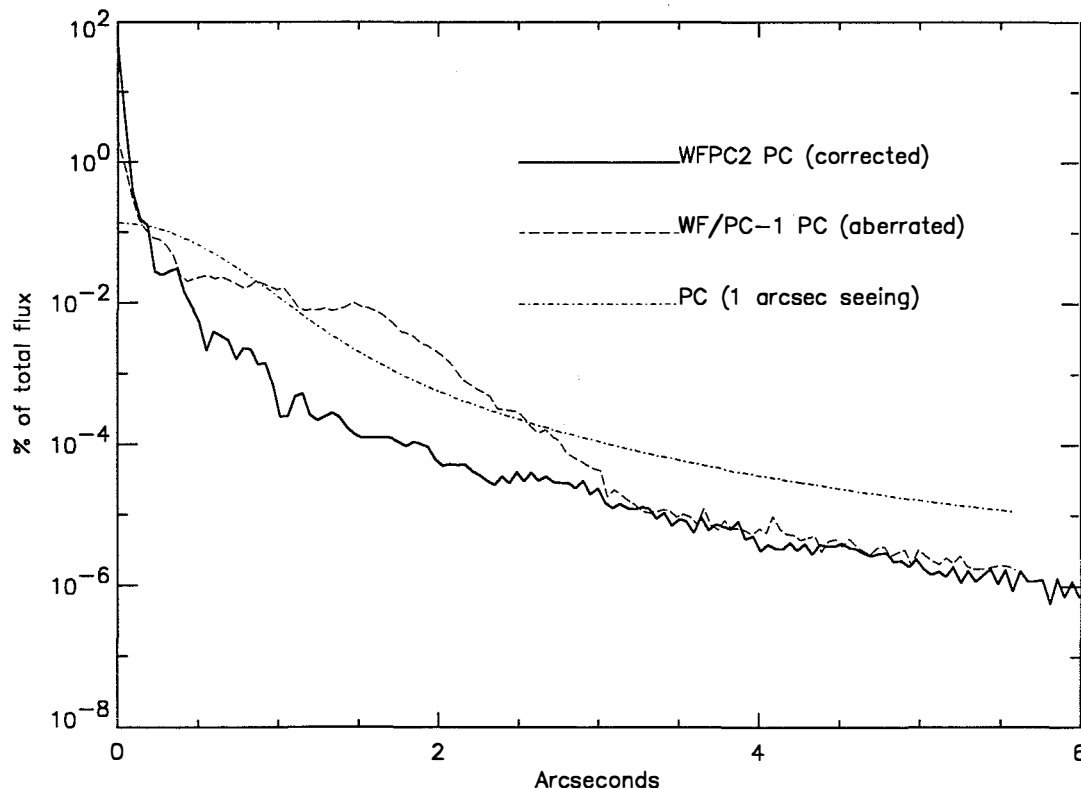


Figure 5.1 PSF Surface Brightness. The percentage of the total flux at 4000Å falling on a PC pixel as a function of the distance from the peak of a star image.

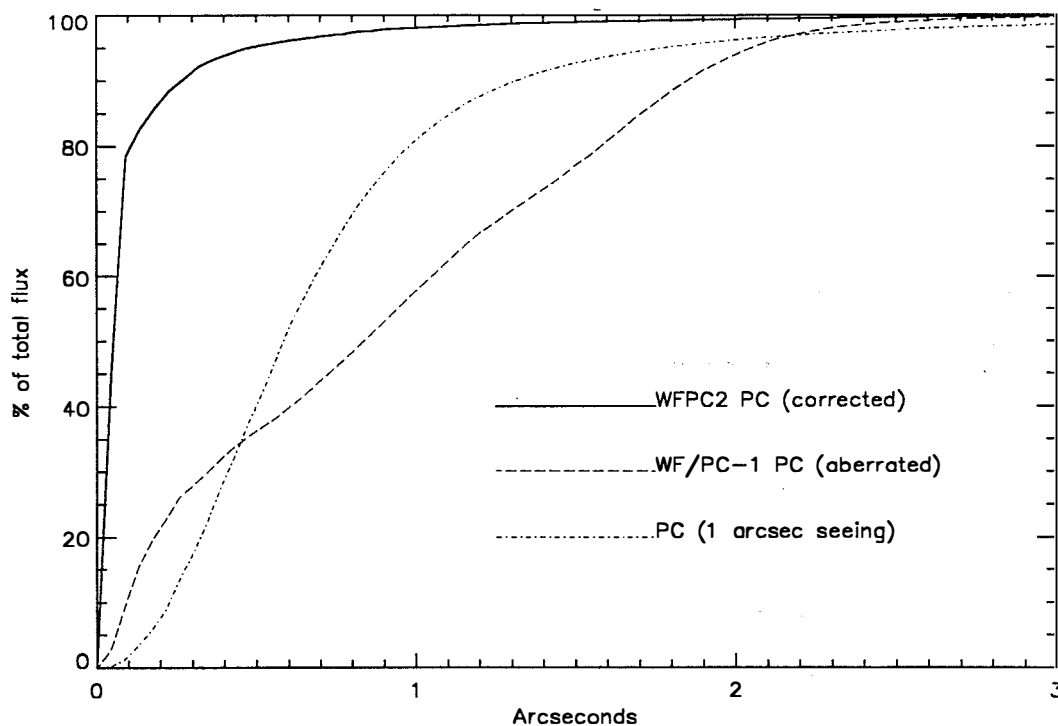


Figure 5.2 Encircled Energy. The percentage of the total flux at 4000Å within a given radius of the image peak.

5.2. MODEL PSFs

Considerable effort has gone into the modeling of the HST PSF, both in order to measure the optical aberrations in support of the WFPC2, COSTAR and advanced scientific instruments and to provide PSFs for image deconvolution in the present aberrated telescope. Such PSFs are noise free and do not require valuable HST observing time. Software to generate model PSFs for any WF/PC-1 filter and at any location within the field of view is available from the STScI. It can also be used to generate model PSFs for the WFPC2. The results are illustrated in Tables 5.1 and 5.2 for the PC and WFC respectively. A representative PSF is on the left in each panel. It meets the wavefront error budget, with an assumed equal mix of focus, coma, astigmatism, and spherical aberration. On the right is the diffraction limited case for comparison. In each case the percentage of the total flux in a central 5×5 pixel region of a point source is displayed. The peak of the star image can be at an arbitrary point relative to the boundaries of the CCD pixels. Two cases are shown: one where the star is approximately centered on a pixel, and one where it is approximately centered at a pixel corner. As a consequence of the under-sampling in the WFPC2, the limiting magnitude attainable in the background limit varies by about 0.5 magnitude, depending on the position of the source. This point is discussed in more detail in Chapter 6.

Neither observed or modeled PSFs will provide a perfect match to the PSF in actual science observations due to modeling uncertainties, the "jitter" in the HST pointing, and orbit to orbit variations in telescope focus ("breathing" - which seems to generally be limited to about 1/20 wave peak to peak). Jitter is not predictable but can be recovered to a reasonable extent for observations obtained in Fine Lock. It can only be estimated for observations obtained in Coarse Track. In long exposures, up to about 10 milliarcseconds of apparent pointing drift may occur as a result of the breathing effects in the FGS.

2000A Peak near corner of PC pixel :

0.7	0.7	1	0.5	0.8	0.5	1	0.7	0.6	0.6
1	14.4	14.1	1	0.7	1.1	20.6	16.3	1.1	0.7
1.2	20.6	21.2	1.8	0.6	1.1	19.8	20.6	1.2	0.6
0.5	1.6	1.9	1	0.8	0.9	0.9	1	0.5	0.3
0.4	1	0.7	0.6	0.6	0.5	0.5	0.6	0.2	0.3

Peak near center of pixel :

0.4	0.6	1.1	0.6	1	0.2	0.5	1	0.6	0.7
0.5	2.1	8.7	2.7	0.9	0.5	1.8	5.9	1.1	1
0.9	6.3	45.2	6.5	0.6	1	4.9	53.4	6.3	0.7
1.2	0.9	4.2	1.4	0.6	1.1	0.7	7.2	1.4	0.6
0.7	0.5	0.8	0.6	0.7	0.5	0.4	0.5	0.5	0.4

4000A Peak near corner of PC pixel :

0.4	2.1	2.3	0.3	0.3	0.5	3.1	2.6	0.4	0.1
2.3	16	15.6	2.1	0.2	3.3	16.8	17.2	3.8	0.4
3.6	15.9	17.1	4.7	0.5	2.2	16.5	17.4	2.6	0.2
0.8	4.2	3.8	1.1	0.3	0.3	3.2	3.6	0.5	0.3
0.2	0.6	0.8	0.2	0.2	0.1	0.3	0.2	0.2	0.1

Peak Near Center of pixel

0.1	0.8	1.2	0.8	0.3	0.1	0.3	0.5	0.3	0.1
0.5	6.4	6.2	6.7	1	0.4	5.1	5.1	4.8	0.4
0.6	5.3	47.9	5.4	0.6	0.4	4.9	51.6	5.6	0.5
0.4	3.3	4.5	2.7	0.2	0.2	3.6	6.3	3.8	0.4
0.1	0.2	0.4	0.2	0.1	0.1	0.3	0.6	0.2	0.1

8000A Peak near corner of PC pixel :

2.5	1.2	1.2	2.4	1.7	1.8	1.1	1.2	1.9	1.1
1.1	13.4	14.3	1.3	2	1	14.2	14.7	1.1	1.7
1.1	14.3	14.6	1.1	1.6	1.1	13.9	14.7	1.2	1.9
1.5	1.2	1.1	1.6	1	2.1	1.2	1.1	2	1.4
1.1	1.4	1.6	1.1	0.1	1.2	1.7	1.5	1.2	0.2

Peak near center of pixel :

1.9	2.5	1.6	2.3	2	1.6	2.1	1.3	1.8	1.6
2.4	1.8	7.1	2	2.5	2.2	1.8	7.3	1.9	2.2
1.3	7.5	25.4	7.4	1.4	1.3	7.6	26	7.5	1.5
1.5	2.2	7.8	1.9	1.6	1.7	2	7.7	2	1.8
1.3	1.6	1.1	1.7	1.2	1.5	2	1.5	2.2	1.4

Table 5.1 PC Point Spread Functions shown as percentages of the total flux in a 5 by 5 pixel region. On the left in each case is a typical PSF that meets the instrument's wavefront error budget. On the right is the diffraction limited case for comparison.

<i>2000A Peak near corner of WF pixel :</i>										
0.7	2.1	1.9	0.5	0.1	0.5	1.6	1.4	0.5	0.1	
0.9	18	22.3	2.4	0.3	1	20.4	20	1.3	0.2	
1.1	15	22.5	2.3	0.3	0.9	20.4	23.1	1.1	0.2	
0.3	2	2	1.1	0.2	0.6	1.6	1.2	0.5	0.1	
0.1	0.3	0.2	0.3	0.1	0.2	0.4	0.3	0.1	0.1	
<i>Peak near center of pixel :</i>										
0.3	0.6	0.8	0.4	0.2	0.2	0.3	0.6	0.4	0.2	
0.8	3.1	3.6	1.7	0.2	0.3	2.1	3.4	1.5	0.3	
1.3	4.1	66.7	2.7	0.4	0.5	3	73.2	2.4	0.4	
0.5	1.8	3.9	2.1	0.3	0.3	1.2	3.8	1.7	0.3	
0.1	0.4	1	0.6	0.3	0.2	0.3	0.7	0.5	0.2	
<i>4000A Peak near corner of WF pixel :</i>										
0.6	1	0.6	0.4	0.2	0.3	0.8	0.7	0.5	0.3	
0.5	19.9	22.4	0.9	0.5	0.7	21.3	21.4	0.7	0.3	
0.7	18	24.1	1	0.5	0.5	22.1	22.5	0.7	0.3	
0.3	0.8	0.9	0.7	0.4	0.5	0.9	0.7	0.3	0.2	
0.3	0.4	0.3	0.3	0.3	0.3	0.4	0.3	0.2	0.1	
<i>Peak near center of pixel :</i>										
0.5	0.6	0.5	0.4	0.4	0.4	0.4	0.5	0.3	0.3	
0.6	1.3	5.3	0.9	0.3	0.4	0.8	4.9	1.1	0.3	
0.8	7	63	3.7	0.4	0.6	4.4	67.6	5.5	0.4	
0.4	1	5.4	0.9	0.3	0.3	0.9	4.8	0.8	0.2	
0.3	0.3	0.6	0.8	0.4	0.2	0.3	0.6	0.6	0.3	
<i>8000A Peak near corner of WF pixel :</i>										
0.2	2	3	0.4	0.2	0.2	2.7	2.2	0.3	0.3	
2	17.5	18.7	2.9	0.2	2.2	18.2	18.5	2.6	0.1	
2.2	18.6	18.8	2.9	0.2	2.2	18.7	19.2	2.8	0.1	
0.2	2.3	2.7	0.4	0.2	0.2	2.6	2.3	0.2	0.2	
0.3	0.2	0.1	0.2	0.1	0.2	0.1	0.1	0.3	0.2	
1	2	3	4	5						
<i>Peak near center of pixel :</i>										
0.1	0.5	0.4	0.2	0.1	0.1	0.3	0.4	0.3	0.1	
0.5	5	5.4	2.9	0.1	0.2	4.1	5.4	3.5	0.2	
0.7	5.9	54.2	4.8	0.2	0.4	5	55.4	6	0.4	
0.4	4.6	5.3	3.4	0.2	0.2	4	5.2	3.8	0.3	
0.1	0.3	0.3	0.3	0.1	0.1	0.2	0.3	0.2	0.1	

Table 5.2 *WF Point Spread Functions* On the left in each case is a typical PSF that meets the instrument's wavefront error budget. On the right is the diffraction limited case for comparison.

5.3. ABERRATION CORRECTION.

The strategy for correction of the HST aberration preserves the optical layout of WF/PC-1, but with steep corrective figure on the relay secondary mirrors and substantially tighter optical alignment tolerances. The optical correction implemented for WFPC2 will recover near-diffraction limited images over the entire CCD fields of view. We expect that the corrective optics will enable essentially all of the scientific objectives of the original WF/PC to be met.

Through a number of independent analyses, based on investigations of star images obtained on-orbit and the examination of fixtures used during the figuring of the primary mirror, the aberrations of the HST optics are now considered well characterized. The surface of the primary mirror was figured to an incorrect conic constant: -1.0139 ± 0.0005 rather than the -1.0023 design requirement, resulting in a large amount of spherical aberration. By design, WF/PC-1 creates an image of the primary mirror near the surface of the relay cassegrain secondary mirror in each of its channels. This design was originally intended to minimize vignetting in the relay optics, but for WFPC2 the image (complete with the wavefront aberration) serves an additional purpose. The optical figure of the WFPC2 secondary mirrors has been altered with the addition of a compensating 'error' in conic constant. By adopting a prescription within the error bars for the HST primary mirror, corrective secondary mirrors have been made with sufficient accuracy that we expect the residual spherical aberration in the WFPC2 wavefront to be small compared to other terms in the WFPC2 optical wavefront budget. On the other hand, new and stringent alignment requirements are created by the steep optical figure on the corrective relay secondary mirrors. The primary mirror image must be accurately centered on the corrective mirror, and must have the correct magnification. Centering is the most demanding requirement. A failure to center accurately would create a new aberration in the form of coma. A misalignment of 7% of the pupil diameter introduces as much RMS wavefront error as was present in the form of spherical aberration prior to the introduction of corrective optics. The new requirements for alignment accuracy and stability lead to the introduction of a tip-tilt mechanism on the pickoff mirror to compensate for camera alignment uncertainties with respect to the OTA, and actuated fold mirrors which can compensate for internal misalignments. There is an additional term in the CEIS specification of the overall instrument wavefront error budget for alignment stability. It is $\lambda/25$ RMS at 6328\AA , as shown in the Table 5.3.

Camera	WFC (F/12.9)	PC(F/28.3)
Design error	$\lambda/143$	$\lambda/50$
Fabrication and alignment error	$\lambda/14.7$	$\lambda/14.7$
Alignment stability error	$\lambda/25$	$\lambda/25$
Total wavefront error	$\lambda/12.6$	$\lambda/12.3$

Table 5.3 Wavefront Error Budget

The first two lines in the wavefront error budget are essentially identical to those for WF/PC-1. 'Design error' refers to the aberrations inherent in the design itself, which would be seen if the optics conformed perfectly to their specifications. All the optics have been fabricated and integrated into the WFPC2 optical bench, and it has been established on the basis of component tests, end-to-end optical interferometry, and through focus phase retrieval that the WFPC2 optical system is performing well within the stated tolerances for 'fabrication and alignment' in the current laboratory environment. What remains is to demonstrate the stability of the optical alignment during forthcoming instrument tests, launch vibrations, and in response to the thermal environment on-orbit. The 'stability' line anticipates these uncertainties, and must be verified during system tests and early science operations.

6. EXPOSURE TIME ESTIMATION

6.1. PRELIMINARY SYSTEM THROUGHPUT

A decision on a suitable exposure time will require the combination of

- The overall spectral response of the system (Figure 2.4).
- The spectral transmission of the filters (Chapter 3 and Appendix 8.1).
- The spectral energy distribution and spatial profile of the target.
- The point response function and pixel size of the instrument (Chapter 5).
- Criteria for specifying desirable charge levels.

When the transmissions of filters $T(\lambda)$ are combined with the **preliminary** overall system response $Q(\lambda)$, we obtain detective quantum efficiency plots (electrons-per-photon as a function of λ) for each filter. These DQE plots link the output of the CCD to the photon flux at the input to an unobscured 2.4 m telescope.

These calibrations exist in the STScI Calibration Data Base and are accessible with the STSDAS Synphot package or with the XCAL software. The XCAL and Synphot Users Guides should be consulted for further details. We include here a sufficient calibration for exposure planning.

In Table 6.1 the **preliminary** dimensionless efficiency and the mean wavelength for each filter are tabulated together with the effective width, the equivalent Gaussian dimensionless width, the maximum transmission, the derivative of the mean wavelength with respect to spectral index, the pivot wavelength, average wavelength, and wavelength of maximum transmission. The parameters are defined as follows. The dimensionless efficiency is

$$\int Q(\lambda)T(\lambda)d\lambda / \lambda$$

The mean wavelength is defined in Schneider, Gunn, and Hoessel *Ap. J.*, 264, 337 (1983)

$$\bar{\lambda} = \exp \left[\frac{\int Q(\lambda)T(\lambda) \log_e(\lambda) d\lambda / \lambda}{\int Q(\lambda)T(\lambda) d\lambda / \lambda} \right]$$

This rather unconventional definition has the property that the correspondingly defined mean frequency is just c/λ . It is in some sense halfway between the conventional frequency mean and the wavelength mean. The pivot wavelength is defined as

$$\lambda_p = \left[\frac{\int Q(\lambda)T(\lambda)\lambda d\lambda}{\int Q(\lambda)T(\lambda) d\lambda / \lambda} \right]^{1/2}$$

The effective Gaussian is defined implicitly by

$$\sigma^2 = \frac{\int_{\bar{\lambda}-5\sigma}^{\bar{\lambda}+5\sigma} Q(\lambda)T(\lambda) (\log_2(\lambda/\bar{\lambda}))^2 d\lambda / \lambda}{\int_{\bar{\lambda}-5\sigma}^{\bar{\lambda}+5\sigma} Q(\lambda)T(\lambda) d\lambda / \lambda}$$

where the integration limits eliminate unrealistic contributions from imperfect blocking far from the passband. The effective width of the bandpass is

$$\delta\bar{\lambda} = 2[2\log_2 2]^{1/2} \sigma\bar{\lambda}$$

and it can be shown that

$$\frac{d\bar{\lambda}}{d\alpha} = \bar{\lambda}\sigma^2$$

Of some interest is possible camera-to-camera variation of the mean wavelength, due to the variations in CCD QE. It might be noticeable in the wide bandpass filters, but the preliminary DQE data available is not sufficiently accurate to estimate the effect.

The WFPC2 UBVR system is fairly close as regards effective wavelengths to the Johnson UBVR system, but cross-calibration will be necessary to convert to Johnson magnitudes. See the IDT OV/SV Report and Harris et al. *A.J.* 101, 677 (1991) for examples in the case of WF/PC-1. Figures 6.1 and 6.2 show the preliminary results of regression fits between these two systems on the main sequence stars in the Bruzual,

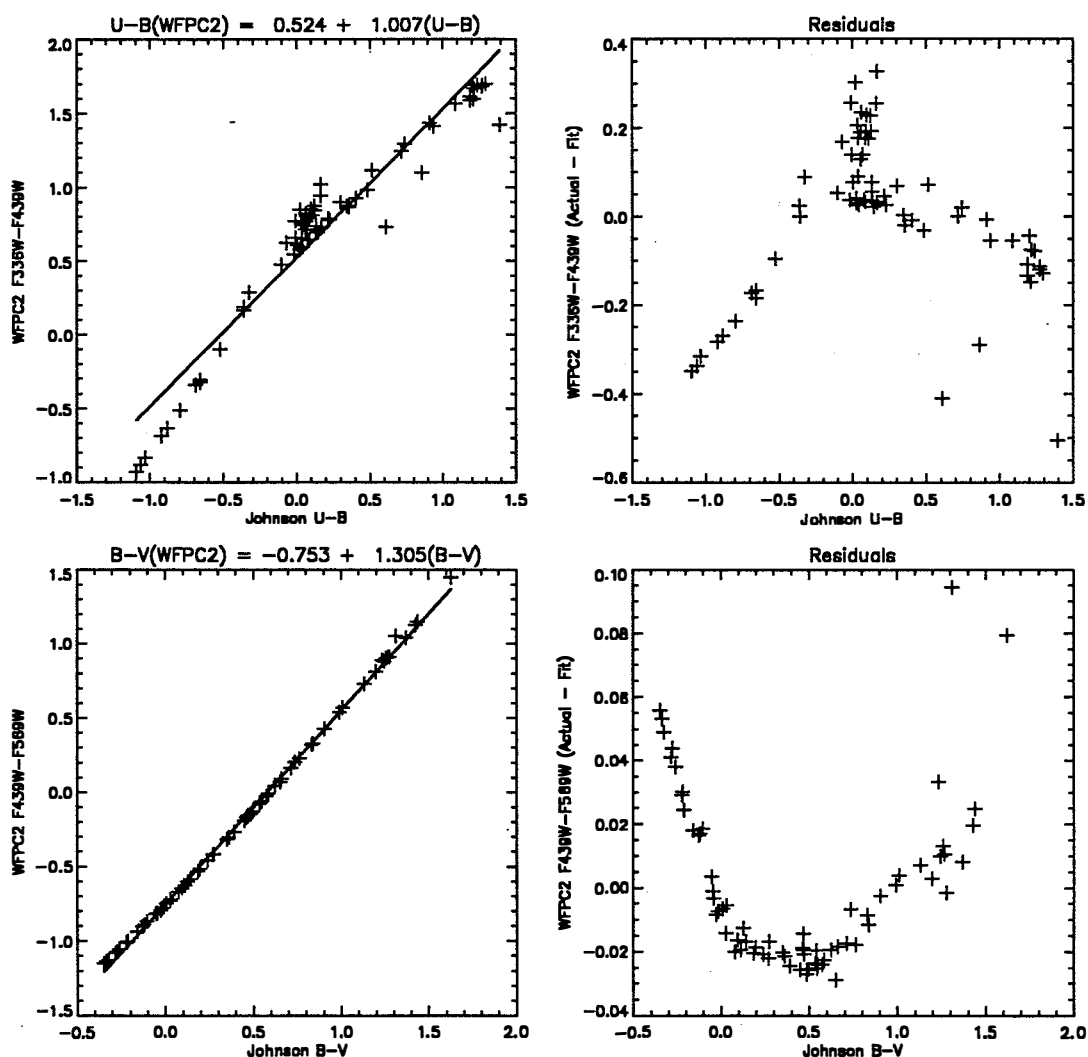


Figure 6.1 Johnson UB regression to WFPC2 passbands

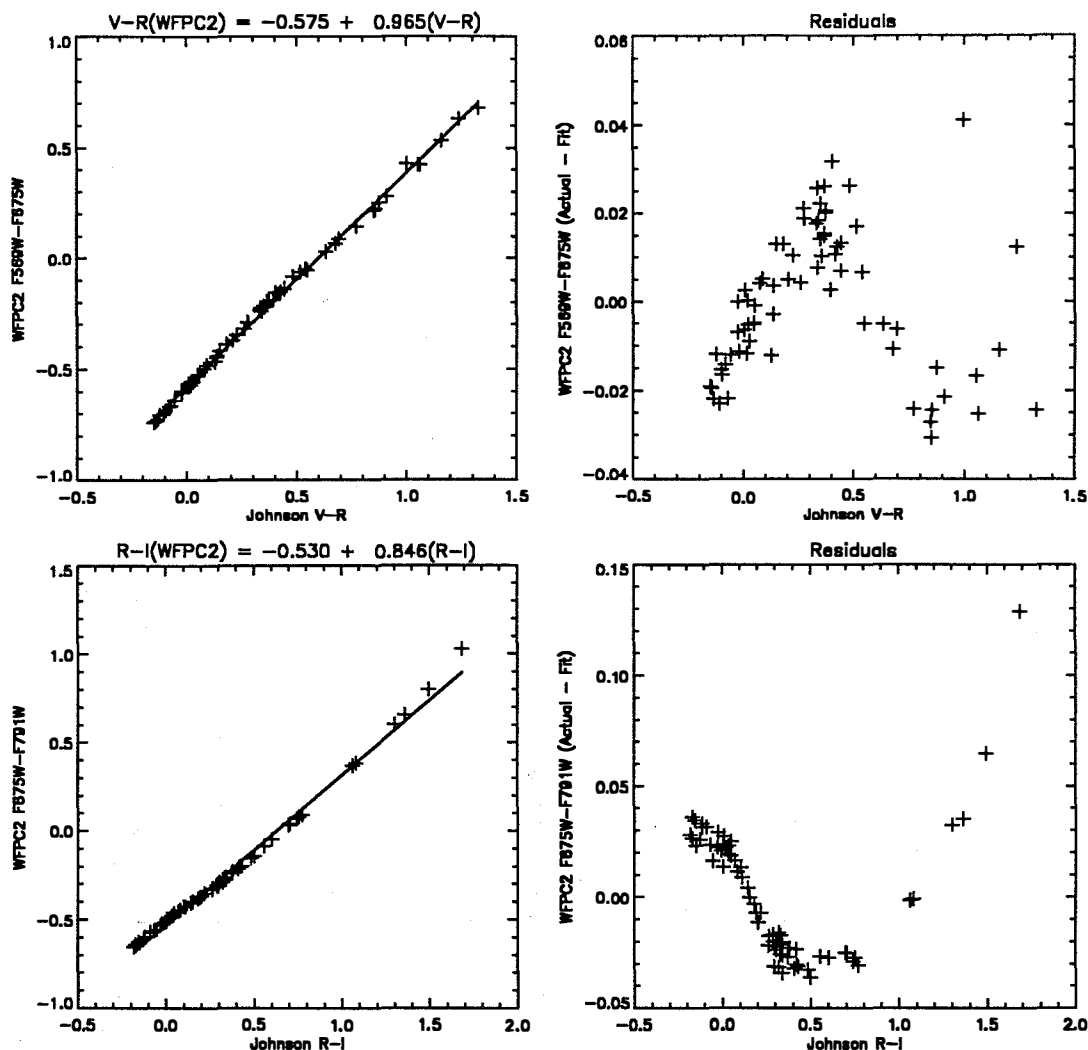


Figure 6.2 Johnson Cousins VRI regression to WFPC2 passbands

Persson, Gunn, Stryker atlas that is installed in the Calibration database system (CDBS).

To estimate the number of electrons collected from a point source of apparent visual magnitude V , one can use the equation

$$N_e = 2.5 \times 10^{11} t \left[\int Q(\lambda) T(\lambda) d\lambda / \lambda \right] \times 10^{-0.4(V+AB_v)}$$

where, t is the exposure time in seconds, the QT integral is given in Table 6.1, and AB_v is given in Table 6.2 as a function of spectral type and wavelength for some example spectral energy distributions. If one knows the spectral index α (which is zero for a source with a flat continuum), $V+AB_v$ can also be calculated as the monochromatic Oke system magnitude at the corrected mean wavelength of the filter:

$$V + AB_v = -2.5 \log_{10} (F_v [\bar{\lambda} + \alpha(d\bar{\lambda}/d\alpha)]) - 48.6$$

where F_v is the flux in $\text{ergs cm}^{-2} \text{s}^{-1} \text{Hz}^{-1}$ as in Oke and Gunn, *Ap. J.*, 266, 713 (1983). See also Koornneef, J., et al. "Synthetic Photometry and the Calibration of the Hubble Space Telescope" in Highlights of Astronomy 7, 833, J.-P. Swings Ed. (1983).

Filter	$\int Q T d\lambda / \lambda$	$\bar{\lambda}$	$\delta\bar{\lambda}$	σ	$Q T_{MAX}$	$d\bar{\lambda} / d\alpha$	λ_p	$\langle \lambda \rangle$	MAX
F122M	0.02%	1368	339.6	10.54%	0.19%	15.20	1574	1738.0	1256
F130LP	9.65%	4796	5365.2	47.50%	12.27%	1082.33	5683	6105.3	6183
F157W	0.06%	1538	424.9	11.73%	0.24%	21.17	1637	1707.2	1354
F160W	0.10%	1523	483.1	13.47%	0.26%	27.64	1552	1566.3	1536
F165LP	9.36%	5002	5036.4	42.76%	12.38%	914.50	5777	6151.3	6182
F170W	0.14%	1730	500.2	12.28%	0.48%	26.09	1772	1797.7	1817
F185W	0.10%	1933	307.9	6.77%	0.53%	8.85	1945	1951.5	1901
F218W	0.13%	2159	358.0	7.04%	0.68%	10.71	2170	2176.2	2156
F255W	0.11%	2553	392.9	6.53%	0.66%	10.90	2565	2570.7	2519
F300W	0.48%	2911	744.8	10.87%	1.64%	34.37	2952	2973.9	2722
F336W	0.33%	3344	381.1	4.84%	2.34%	7.83	3363	3373.7	3458
F343N	0.01%	3424	24.5	0.30%	0.65%	0.03	3437	3443.9	3433
F375N	0.01%	3737	26.7	0.30%	0.70%	0.03	3745	3749.6	3737
F380W	0.62%	3960	674.9	7.24%	3.00%	20.74	3981	3991.0	4007
F390N	0.03%	3889	45.3	0.49%	1.64%	0.10	3890	3890.3	3890
F410M	0.15%	4090	146.5	1.52%	3.36%	0.95	4093	4094.1	4098
F437N	0.02%	4369	25.2	0.24%	2.25%	0.03	4369	4369.2	4368
F439W	0.47%	4300	474.8	4.69%	3.24%	9.45	4310	4314.4	4175
F450W	1.33%	4521	957.9	9.00%	7.04%	36.60	4557	4574.9	5068
F467M	0.21%	4669	166.3	1.51%	4.68%	1.07	4670	4671.0	4732
F469N	0.02%	4695	24.9	0.23%	3.24%	0.02	4694	4694.5	4699
F487N	0.03%	4866	25.8	0.23%	4.12%	0.03	4866	4865.9	4864
F502N	0.03%	5013	26.9	0.23%	4.28%	0.03	5013	5013.6	5010
F547M	1.05%	5479	486.1	3.77%	8.89%	7.78	5487	5490.8	5651
F555W	2.50%	5407	1235.6	9.70%	9.17%	50.92	5458	5483.6	5691
F569W	1.92%	5624	973.9	7.35%	9.22%	30.42	5655	5670.2	5690
F588N	0.13%	5893	49.0	0.35%	11.43%	0.07	5894	5893.6	5896
F606W	3.94%	5957	1508.8	10.76%	12.76%	68.91	6026	6059.6	6183
F622W	2.52%	6170	916.6	6.31%	12.27%	24.56	6195	6206.8	6089
F631N	0.08%	6283	30.7	0.21%	11.48%	0.03	6283	6282.7	6281
F656N	0.05%	6564	21.4	0.14%	11.03%	0.01	6564	6564.1	6561
F658N	0.06%	6590	28.5	0.18%	10.65%	0.02	6591	6591.0	6591
F673N	0.10%	6732	47.2	0.30%	10.11%	0.06	6732	6732.4	6731
F675W	2.16%	6714	877.3	5.55%	12.31%	20.67	6735	6745.2	6636
F702W	3.23%	6895	1389.2	8.56%	12.65%	50.47	6946	6971.8	6540
F785LP	0.91%	8674	1407.2	6.89%	4.84%	41.17	8716	8737.5	8306
F791W	1.69%	7829	1217.5	6.60%	9.93%	34.14	7864	7881.5	7400
F814W	1.96%	7940	1531.4	8.19%	10.68%	53.27	7995	8022.8	7266
F850LP	0.47%	9124	1050.6	4.89%	3.80%	21.82	9146	9157.3	8846
F953N	0.01%	9534	61.3	0.27%	1.99%	0.07	9540	9542.0	9528
F1042M	0.02%	10201	381.9	1.59%	0.62%	2.58	10206	10207.7	10113
QF375N-A	0.03%	3765	73.1	0.82%	1.01%	0.26	3766	3766.6	3802
QF375N-B	0.03%	3830	57.2	0.63%	1.32%	0.15	3831	3831.4	3828
QF375N-C	0.03%	3913	59.3	0.64%	1.75%	0.16	3915	3915.3	3908
QF375N-D	0.04%	3992	63.5	0.68%	2.00%	0.18	3993	3993.4	3990
QFCH4N-A	0.07%	5443	38.4	0.30%	8.38%	0.05	5448	5450.9	5442
QFCH4N-B	0.08%	6211	44.1	0.30%	10.85%	0.06	6217	6220.7	6202
QFCH4N-C	0.07%	7286	42.1	0.25%	9.88%	0.04	7289	7290.1	7278
QFCH4N-D	0.03%	8922	59.9	0.29%	3.79%	0.07	8926	8927.6	8930
POLQ	5.93%	5592	4489.0	34.09%	8.72%	649.87	6157	6430.8	6569
POLQ	1.39%	7191	5144.4	30.38%	3.93%	663.72	7683	7896.4	8002

Table 6.1 Preliminary System Throughputs

	B-V	1500	2000	2500	3000	3500	4000	4500	5000	6000	7000	8000	9000	10000
sky	1.10	2.45	5.46	5.46	3.12	2.00	1.03	0.55	0.18	-0.11	-0.33	-0.55	-0.65	-0.75
B0	-0.31	-1.60	-1.50	-1.20	-0.78	-0.62	-0.46	-0.36	-0.22	0.16	0.46	0.76	0.96	1.17
A0	0.00	2.22	1.35	1.11	1.21	1.00	-0.23	-0.16	-0.09	0.11	0.22	0.33	0.36	0.4
F0	0.27	7.22	4.10	3.11	1.99	1.38	0.29	0.06	0.03	0.03	0.05	0.08	0.09	0.1
G0	0.58	8.9	6.35	4.61	2.46	1.63	0.67	0.26	0.08	-0.04	-0.12	-0.21	-0.23	-0.25
K0III	1.07	13	10.3	8.11	5.46	2.13	1.16	0.46	0.2	-0.24	-0.42	-0.61	-0.66	-0.72
M0III	1.60	15	12.3	9.36	6.21	4.63	2.26	0.96	0.51	-0.46	-0.76	-1.06	-1.12	-1.19
gE	1.00	6.82	6.41	5.43	3.63	2.49	1.40	0.55	0.21	-0.19	-0.52	-0.81	-1.07	-1.29
Sa	0.80	5.40	4.80	4.10	3.00	2.01	1.12	0.44	0.19	-0.17	-0.44	-0.7	-0.95	-1.16
Sbc	0.60	4.03	3.18	2.86	2.46	1.54	0.84	0.34	0.17	-0.14	-0.37	-0.6	-0.84	-1.04
Scd	0.45	2.67	2.29	2.15	1.76	1.35	0.65	0.28	0.13	-0.11	-0.26	-0.39	-0.47	-0.58
IrI	0.30	1.77	1.40	1.36	1.24	0.94	0.43	0.34	0.17	0.13	-0.04	-0.21	-0.33	-0.45

Table 6.2 AB_v As a Function of Spectral Type and Wavelength

6.2. SKY BACKGROUND

The actual sky brightness depends on the heliocentric ecliptic latitude and apparent longitude, in a manner summarized in Table 6.3 (taken from an early version of the FOS Instrument Handbook by H. Ford). The appropriate AB_v can be taken from Table 6.2. To convert magnitudes/arcsecond² to magnitudes/pixel² one needs to add 5 (WFC) or 6.7 (PC1).

Apparent Longitude	Ecliptic Latitude			
	0	30	60	90
180	22.1	22.7	23.2	23.3
145	22.4	22.9	23.3	23.3
110	22.3	22.9	23.3	23.3

Table 6.3 Sky Brightness (V magnitude/arcsecond²) as a Function of Ecliptic Latitude and Apparent Longitude

6.3. POINT SOURCES

The signal to noise for a point source in the normal read noise or background limited case is a function not only of the expected number of detected photons I from the source but also of the average background count rate in each pixel B , the point spread function $P(i,j)$, and the weights used to average the signal in the pixels affected by the source. It is easy to show that the signal to noise ratio for optimal weights

	2000 Å		4000 Å		8000 Å	
	Budget	Diffraction	Budget	Diffraction	Budget	Diffraction
PC Center	0.224	0.301	0.252	0.286	0.093	0.096
PC Corner	0.130	0.152	0.114	0.123	0.085	0.087
WF Center	0.453	0.542	0.410	0.468	0.312	0.325
WF Corner	0.158	0.178	0.181	0.191	0.140	0.144

Table 6.4 Signal to noise corrections

(which are proportional to the point spread function) is given by

$$(S / N)^2 = \frac{I^2}{B} \sum P(i,j)^2$$

The sum on the right is tabulated for a few representative cases in Table 6.4. To estimate the signal to noise, multiply the signal to noise obtained assuming all the flux is in one pixel by the square root of the value in the Table.

6.4. EXTENDED SOURCES

In general, the signal to noise level for extended sources is computed for each pixel. The sources of noise are read noise, sky background, flat field residuals, and photon noise. If read noise is the dominant noise source, the signal to noise can be improved by using AREA mode (see page 13), at some cost in resolution. Observers are encouraged to simulate the expected image in order to optimize their observations.

For high- z galaxies, a much smaller fraction of light falls in the central pixel than for a point source of equivalent total flux. The rough magnitude difference between the light falling in the central pixel and the entire galaxy is plotted against redshift in Figure 6.3, for giant elliptical galaxies. For other types of galaxies, a morphological term can be added to the values in for example, 0.6 magnitudes for lenticulars, 0.7 for S, 0.8 for Sab, 0.9 for Sbc, 1.2 for Scd, and 1.8 for Im. These values must be increased by an additional 1.7 magnitudes for the PC.

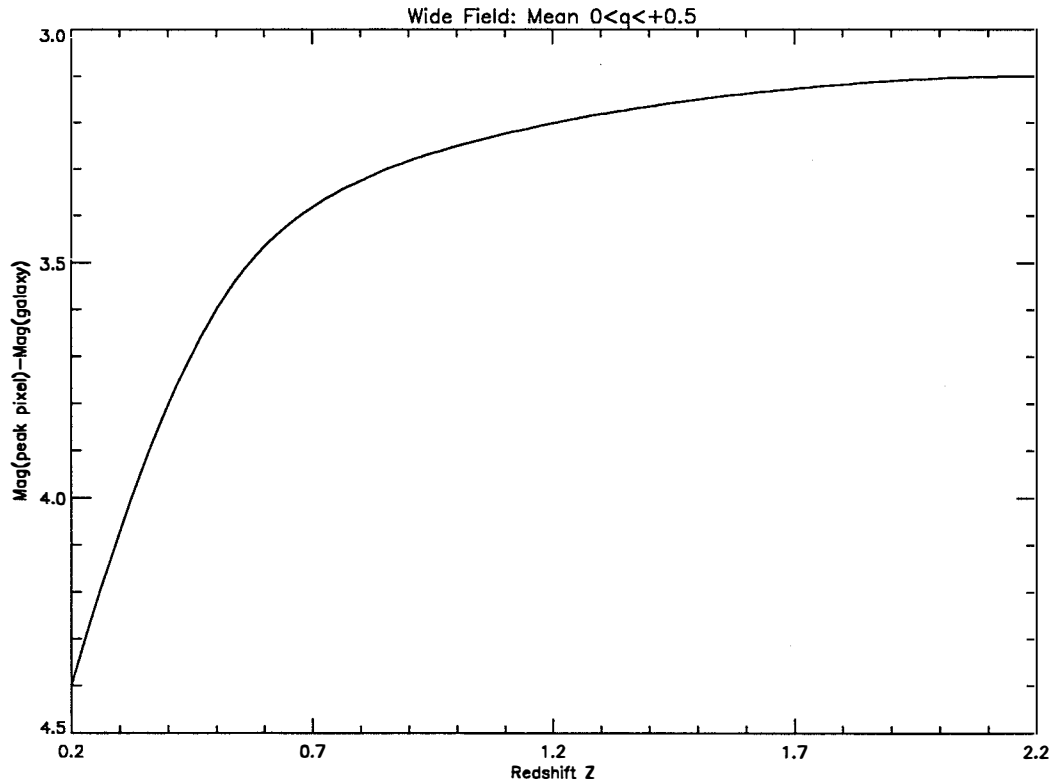


Figure 6.3 Giant Elliptical Galaxy

6.5. RED LEAKS IN UV FILTERS

The "red leaks" in the UV filters are shown in Figure 6.4 for F122M, F157W (which is not baselined), F160W (the new Woods filter), F170W, F185W, F218W, F255W and F300W. The presence of significant red leaks in the UV filters, together with the much greater sensitivity and wavelength coverage in the red part of the spectrum, makes calibration of UV observations difficult. Table 6.5 shows preliminary red leak estimates as a percentage of the total detected flux from dereddened stellar sources ordered by spectral type. In each column, the red leak is defined as the percentage of the detected flux longward of the cutoff wavelength in the second row. In the presence of interstellar reddening, the red leaks will be larger.

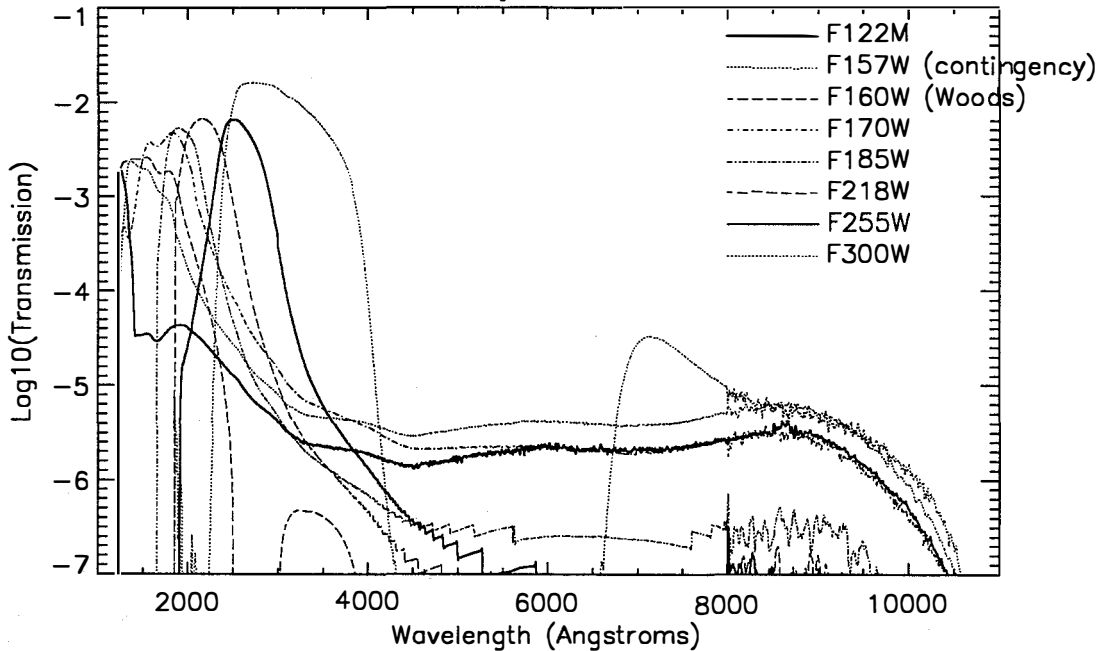


Figure 6.4 UV Filter Red Leaks

Filter	Wavelength	122	157	160	170	185	218	255	300	122	157	160	170	185	218	255	300
Cutoff Wavelength		140	240	240	260	260	280	310	400	380	380	380	380	380	380	380	380
9 SGR	O6	9.2	0.5		0.3	0.1	0.1	0.2		0.2	0.1						0.4
9 SGE	O8F	9.2	0.5		0.3	0.1	0.1	0.2		0.2	0.1						0.4
HR 8023	O6	12.1	0.7		0.3	0.2	0.1	0.3		0.3	0.1						0.5
-1 935	B1V	10.9	0.6		0.3	0.1	0.1	0.3		0.3	0.1						0.5
60 CYG	B1V	10.9	0.6		0.3	0.1	0.1	0.3		0.3	0.1						0.6
102 HER	B2V	12.3	0.8		0.4	0.2	0.2	0.3	0.1	0.5	0.2		0.1				0.7
ETA HYA	B3V	12.4	0.9		0.4	0.2	0.2	0.3	0.1	0.7	0.3		0.1				0.8
IOTA HER	B3V	12.4	0.9		0.4	0.2	0.2	0.3	0.1	0.7	0.3		0.1				0.8
HR 7899	B4V	12.5	0.9		0.4	0.2	0.2	0.3	0.1	0.7	0.3		0.1				0.8
38 OPH	A1V	17.5	1.3		0.6	0.3	0.2	0.4	0.1	1.5	0.6		0.2				1.0
HR 7174	B6V	17.9	1.5		0.6	0.3	0.2	0.4	0.1	2.0	0.7		0.2	0.1			1.2
9 VUL	B7V	17.9	1.5		0.6	0.3	0.2	0.4	0.1	2.1	0.8		0.2	0.1			1.3
HD 189689	B9V	26.5	2.2		0.8	0.3	0.2	0.4	0.2	4.1	1.2		0.3	0.1		0.1	1.5
THETA VIR	A0V	43.6	4.7		1.4	0.4	0.3	0.6	0.3	12.7	3.3		0.8	0.1		0.1	2.3
NU CAP	B9V	42.7	4.3		1.3	0.4	0.3	0.6	0.3	11.4	2.9		0.7	0.1		0.1	2.0
HR 6169	A2V	43.4	4.6		1.4	0.4	0.3	0.6	0.3	12.5	3.2		0.7	0.1		0.1	2.1
HD 190849A	A1V	60.5	4.6		1.3	0.4	0.3	0.5	0.3	16.3	3.1		0.7	0.1		0.1	1.8
69 HER	A2V	43.4	4.6		1.4	0.4	0.3	0.6	0.3	12.5	3.2		0.7	0.1		0.1	2.0
HD 190849B	A3V	82.0	10.7	0.1	2.3	0.5	0.3	0.7	0.4	32.9	8.0		1.3	0.2		0.1	2.3
58 AQL	A0V	62.3	5.5		1.5	0.4	0.3	0.6	0.4	20.2	4.0		0.9	0.2		0.1	2.5
78 HER	B9V	61.9	5.3		1.5	0.4	0.3	0.6	0.3	19.3	3.8		0.8	0.2		0.1	2.2
HR 6570	A7V	82.9	11.8	0.1	2.4	0.6	0.3	0.8	0.4	36.1	9.1		1.5	0.2	0.1	0.1	2.5
HD 187754	A2V	96.3	23.5	0.1	3.9	0.7	0.4	0.9	0.6	53.0	19.2		2.7	0.3	0.1	0.2	3.0
THETA 1 SER	A5V	96.0	21.0	0.1	3.5	0.7	0.4	0.9	0.5	48.5	16.6		2.2	0.3	0.1	0.2	2.5
PRAE 276		99.5	28.4	0.2	4.4	0.8	0.4	0.9	0.6	56.4	23.2		3.0	0.4	0.1	0.2	2.8
PRAE 114		99.5	27.3	0.2	4.2	0.8	0.4	0.9	0.5	54.8	22.0		2.8	0.3	0.1	0.2	2.6
PRAE 154		99.9	41.6	0.3	6.5	1.0	0.5	1.0	0.6	62.1	34.2		4.4	0.5	0.1	0.2	2.7
HD 190192	A5V	99.9	42.4	0.3	6.7	1.1	0.5	1.0	0.6	63.0	35.0		4.5	0.5	0.1	0.2	2.7
PRAE 226		99.9	42.4	0.3	6.6	1.0	0.5	1.0	0.6	63.1	35.0		4.5	0.5	0.1	0.2	2.6
PRAE 37		100.0	71.5	0.9	18.5	2.9	0.9	1.4	0.7	75.9	60.6	0.1	12.9	1.4	0.2	0.2	2.7
HD 191177	F4V	100.0	88.9	2.8	41.7	7.3	1.4	1.9	0.9	83.8	78.2	0.2	31.3	4.1	0.3	0.4	3.5
PRAE 332		100.0	87.8	2.7	39.2	6.8	1.3	1.8	0.8	82.2	76.1	0.1	28.4	3.6	0.2	0.3	2.8
BD +293891	F6V	100.0	90.2	3.0	44.3	8.2	1.8	2.1	0.9	84.7	79.3	0.2	33.0	4.5	0.3	0.4	3.0
PRAE 222		100.0	81.4	1.4	27.1	4.4	1.3	1.8	0.8	81.8	71.1	0.1	19.9	2.3	0.2	0.3	2.7
HD 35296	F8V	100.0	82.6	1.4	28.4	4.6	1.3	1.8	0.9	83.2	73.0	0.1	21.3	2.5	0.2	0.3	2.8
BD +263780	G0V	100.0	82.8	1.4	28.6	4.6	1.3	1.8	1.0	83.4	73.2	0.1	21.5	2.5	0.3	0.3	2.8
HD 148816	F9V	100.0	81.9	1.4	27.5	4.4	1.3	1.8	0.9	82.3	71.8	0.1	20.3	2.4	0.2	0.3	2.8
HD 155675	F8V	100.0	91.1	2.8	45.2	8.4	2.2	2.9	1.1	87.6	82.1	0.2	35.3	5.0	0.5	0.5	3.3
PRAE 418		100.0	91.6	2.8	46.6	8.7	2.3	2.9	1.2	88.3	83.1	0.1	36.9	5.4	0.5	0.5	3.2
HYAD 1		100.0	92.1	2.8	48.0	9.1	2.3	3.0	1.3	89.0	84.1	0.2	38.6	5.7	0.5	0.6	3.4
HD 122693	F8V	100.0	92.2	2.8	48.3	9.1	2.3	3.0	1.3	89.1	84.2	0.2	38.8	5.8	0.5	0.6	3.5
HD 154417	F8V	100.0	91.8	2.8	47.0	8.8	2.3	2.9	1.2	88.5	83.4	0.2	37.4	5.5	0.5	0.5	3.3
HYAD 2		100.0	97.8	10.8	77.9	25.3	4.1	2.9	1.3	91.1	89.8	0.6	63.1	16.2	0.9	0.6	3.3
HD 227547	G5V	100.0	97.8	11.0	78.4	25.6	4.1	3.0	1.4	91.3	90.0	0.6	63.8	16.5	1.0	0.6	3.4
HD 154760	G2V	100.0	97.8	11.0	78.1	25.4	4.1	2.9	1.4	91.1	89.8	0.6	63.3	16.2	0.9	0.6	3.4
HD 190605	G2V	100.0	98.0	11.1	79.3	26.4	4.2	3.0	1.5	91.7	90.5	0.6	65.1	17.3	1.0	0.6	3.4
HYAD 15		100.0	98.0	11.0	79.6	26.7	4.2	3.0	1.5	92.0	90.8	0.6	65.8	17.7	1.0	0.6	3.4
HD 139777A	K0V	100.0	97.9	11.1	79.0	26.1	4.1	2.9	1.5	91.6	90.4	0.6	64.7	17.0	1.0	0.6	3.5
HD 136274	G8V	100.0	98.3	11.0	82.1	29.1	4.3	3.1	1.9	93.3	92.3	0.5	69.9	20.4	1.2	0.7	3.7
HYAD 26		100.0	98.4	11.2	82.5	29.7	4.4	3.1	1.9	93.5	92.5	0.6	70.5	21.0	1.2	0.7	3.7
HD 150205	G5V	100.0	98.4	11.2	82.6	29.7	4.4	3.1	1.9	93.4	92.4	0.6	70.5	21.0	1.2	0.7	3.9
HYAD 21		100.0	98.7	11.3	84.9	32.6	4.6	3.2	2.3	94.6	93.7	0.5	74.4	24.2	1.4	0.8	4.0
+02 3001	G8V	100.0	98.7	11.3	85.1	33.0	4.6	3.2	2.5	94.8	93.9	0.6	74.9	24.7	1.4	0.8	4.4
HD 190571	G8V	100.0	99.9	75.0	99.0	89.4	28.3	10.5	3.9	97.0	96.8	4.5	91.6	75.3	12.6	3.1	6.5
HYAD 183		100.0	100.0	74.8	99.2	91.1	30.1	11.0	4.9	97.7	97.5	4.2	93.3	79.4	14.8	3.5	7.2
HD 190470	K3V	100.0	100.0	75.0	99.3	91.5	30.6	11.1	5.1	97.8	97.6	4.2	93.5	80.1	15.4	3.7	7.5
HD 154712	K4V	100.0	100.0	65.8	99.3	89.8	33.1	15.1	7.5	98.5	98.3	4.2	95.4	82.0	19.8	5.8	10.2
HYAD 185		100.0	100.0	68.2	99.5	92.0	38.1	15.4	9.1	98.7	98.6	4.3	96.1	85.2	24.4	6.3	11.6
+38 2457	K8V	100.0	100.0	65.7	99.5	91.9	36.3	16.1	10.0	98.8	98.8	4.3	96.5	85.6	23.8	7.0	12.6
HYAD 173		100.0	99.9	41.6	99.0	85.8	23.0	8.6	13.3	99.1	99.0	3.1	96.7	81.1	16.0	4.5	15.7
GL 40	M0V	100.0	100.0	42.1	99.2	88.1	25.7	9.2	16.3	99.3	99.2	3.6	97.3	84.1	18.9	5.2	19.0
HYAD 189		100.0	100.0	42.0	99.3	89.0	27.1	9.6	17.7	99.4	99.3	3.5	97.6	85.3	20.5	5.6	20.2
HD 151288	K7V	100.0	100.0	43.0	99.3	89.7	28.3	10.0	18.5	99.4	99.3	3.7	97.7	86.1	21.7	5.9	21.1
HD 157881	K7V	100.0	100.0	42.0	99.3	89.6	28.1	9.8	18.8	99.4	99.3	3.6	97.7	86.1	21.6	5.8	21.3
HD 132683	M0V	100.0	100.0	42.3	99.4	90.1	29.0	10.1	19.8	99.4	99.4	3.8	97.8	86.7	22.5	6.1	22.5
GL 15A	M0V	100.0	100.0	45.8	99.7	94.3	42.2	14.1	30.4	99.7	99.6	5.1	98.8	92.3	36.7	10.0	33.3
GL 49	M2V	100.0	100.0	43.8	99.6	93.5	39.3	12.9	28.4	99.6	99.6	4.9	98.6	91.3	33.7	8.9	31.4
GL 109	M4V	100.0	100.0	44.9	99.7	95.7	50.1	16.6	37.7	99.8	99.7	5.8	99.1	94.1	45.5	12.8	40.5
GL 15B	M6V	100.0	100.0	47.6	99.9	97.9	68.0	26.6	55.0	99.9	99.9	7.7	99.6	97.1	65.0	23.2	57.2
GL 83.1	M8V	100.0	100.0	43.0	99.4	90.1	31.8	10.3	19.7	99.5	99.4	3.6	97.9	86.8	25.4	6.0	22.2
GL 65	M5V	100.0	100.0	41.9	99.6	92.6	39.6	12.0	25.4	99.6	99.6	3.9	98.5	90.1	34.1	7.9	27.9

Table 6.5 Red Leak in UV Filters A preliminary calculation with dereddened BPGS stellar spectra.

7. CALIBRATION AND DATA REDUCTION

7.1. CALIBRATION OBSERVATIONS AND REFERENCE DATA

Standard calibration observations will be obtained and maintained in the calibration data base at the STScI. This includes those flat field, dark and bias frames needed to operate the Post Observation Data Processing System (PODPS; usually just called the "pipeline"), a photometric calibration derived from standard star observations and the measured filter profiles, and derived determinations of the plate scale, distortion, and so on. The first set of these calibrations will be provided to the STScI by the WFPC2 IDT from the Servicing Mission Observatory Verification (SMOV) and System Level Thermal Vacuum (SLTV) testing periods, and will be maintained and updated thereafter by the STScI with initial assistance from the IDT as part of the long term calibration program. For measurements requiring more precise calibrations, special calibration observations may need to be obtained as part of the observing proposal. Please consult the STScI WFPC2 Instrument Scientists for guidance if the routine calibration appears unlikely to support the requirements of a proposed observation.

7.2. INSTRUMENT CALIBRATION

A database of laboratory characterizations of optical components, CCD sensors, filters, and the flat field channel has been generated to support the instrument calibration. This database of component test results was used to generate this handbook. In addition, the SLTV testing of the assembled instrument with calibrated reference sources is a critical element leading to the calibrated instrument on-orbit. SLTV is currently scheduled for April/May 1993.

On-orbit pointed calibrations can require large HST resources, taking time that could otherwise be used for direct scientific observations. They can also be unsatisfactory due to the limitations of the available astronomical reference sources. The need for such calibrations has been minimized. For WFPC2 the inherent stability and uniformity of the CCD sensors, the well calibrated filters, the internal flat field calibration system, and a calibration database populated with flat field images obtained in SLTV prior to launch should improve the scientific data analysis and productivity.

7.3. FLAT FIELDS

The process of correcting for the effect of the variation in the sensitivity of the WFPC2 with field position is usually known as flat-fielding or flattening. A "flat field" (an exposure of a spatially uniform source) needs to be observed through the telescope and desired filter. Real flat fields are always external; however, the WFPC2 has an internal calibration channel which produces a reasonably flat illumination pattern down to about 1800Å. This channel can be used to monitor and correct for changes in the flat fields. The instrument flat field will also be coarsely monitored using the internal flat channel that is the same as that installed in WF/PC-1, using exposures called INTFLATS. Flat fields in medium bandpass filters will be obtained using the sunlit earth (Target = EARTH-CALIB), as part of routine calibration, in order to provide an absolute reference for the internal calibrations (and remove the low frequency effects of variations in the OTA illumination pattern).

The Earth is an imperfect flat field target because it is too bright for the WFPC2 in the broad-band green and red filters. The rapid motion of the HST also creates streaks across the flat field images. The removal of the streaks requires the combination of multiple earth observations with the streaks at different angles on the

CCDs. An extensive discussion of the generation of earth flat fields is available in Chapter 6 of the IDT OV/SV Report.

The new flat field calibration system works by imaging an illuminated diffuser plate onto the WFPC2 exit pupil (relay secondary), by means of an MgF_2 lens. Two lamps provide optical and FUV illumination providing a flat field which should closely resemble the input beam from the OTA between 1600Å and 10000Å. During SLTV, flat fields will be obtained using both the flat field calibration module and the WFPC2 optical stimulus (HST simulator) to generate a database of ratio images which link the internal flats to external flats. The external stimulus flats will be verified by comparison against on-orbit streak flats, obtained for a small subset of filters. While streak flats are still required, it is anticipated that they will be obtained during the initial in-flight calibration of the instrument, for verification of the internal flat-fielding procedure, and only used thereafter for periodic calibration checks.

Flat fields will be obtained for all filters used by observers by combining information from SLTV test flats (which should be good for all but the lowest spatial frequencies), the calibration channel (which can monitor for time dependent changes in the flat fields), and earth flats in a limited number of filters (which will fix the low frequency terms). Some redundancy is provided by the internal flat channel, but it does not form a part of the baseline calibration plan.

7.4. DARK FRAMES

Dark frames are long exposures that are taken with no light incident on the CCDs. They are used to detect CCD counts (the dark current) caused by thermal generation (at the interfaces between the silicon and oxide layers) as well as the rate of charged particle and secondary radiation events. Estimated dark current and cosmic ray event rates are given in Sections 4.3.7 and 4.3.8 respectively.

7.5. BIAS FRAMES

Bias frames are readouts of the CCDs without an exposure (so the dark current is negligible). They are used to measure the DC offset built into the signal chain to ensure that the ADC input is above zero. They fix the constant that is subtracted from the raw data prior to dark subtraction and flat fielding in Routine Science Data Processing (RSDP).

7.6. DATA REDUCTION AND DATA PRODUCTS

The routine processing of WFPC2 science data consists of the pipeline functions described below. The resulting images will be available on magnetic tape in FITS format, and as photographic prints. The reformatted raw data will also be available, along with the relevant calibration data. The STSDAS Calibration Guide should be consulted for a more complete description than the summary presented here.

7.7. PIPELINE PROCESSING

The pipeline processing of WFPC2 data sets reformats the telemetry received from HST into STSDAS format images, generates headers containing a large number of keywords taken from both the HST and WFPC2 telemetry streams in addition to various STScI ground system databases, and applies the calibration described below. This calibration is done with a module known as "CALWFP2" which is written in the IRAF SPP language and is available, in identical form, to users of the STSDAS system. Therefore, off-line recalibration of observations is fairly easy and will use the same program as the PODOPS system.

CALWFP2 will perform the following operations if required by the observation:

- Bias level removal
- Bias image subtraction (depending on the gain channel in use)
- Dark image scaling and subtraction
- Flat field image correction
- Population of various photometric calibration keywords

In addition, the following conditions are flagged in the Data Quality File (DQF):

- Transmission failures and possible failures
- Known bad pixels (e.g. blocked columns)
- Pixels at the maximum A/D converter level (i.e. saturated)
- Bad pixels in reference images

7.8. DATA FORMATS

The following data will be supplied to observers on FITS tapes:

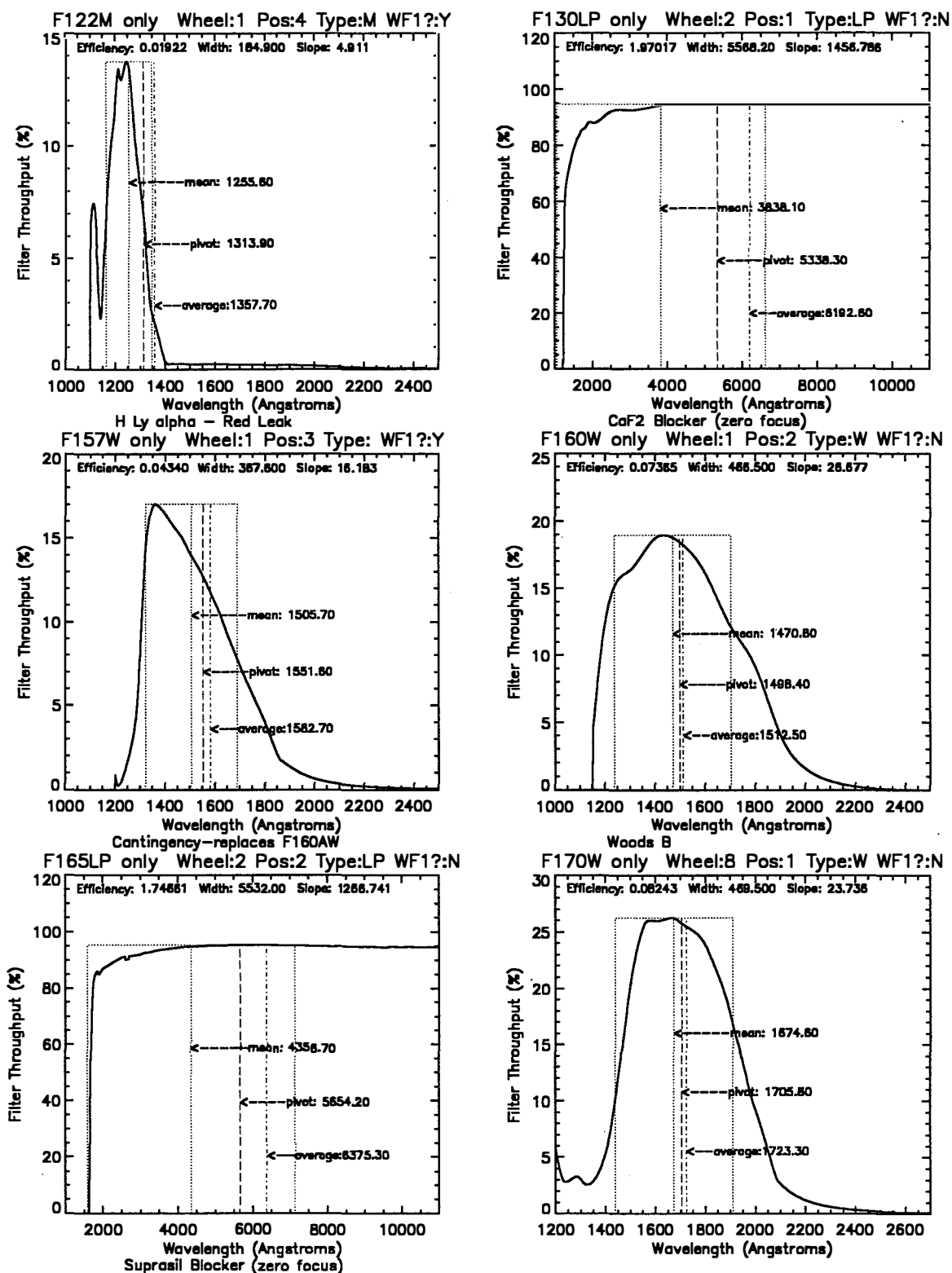
- Edited Image and DQF (uncalibrated) .d0h,.q0h
- Standard Header Packet .shh
- Extracted Engineering Data and DQF .x0h,.q1h
- Trailer File (ASCII file) .trl
- Calibrated Image and DQF .c0h,.c1h

In addition, a histogram file used for monitoring of the signal chain, and a calibration file which gives the throughput curve used in populating the photometric keywords may be included.

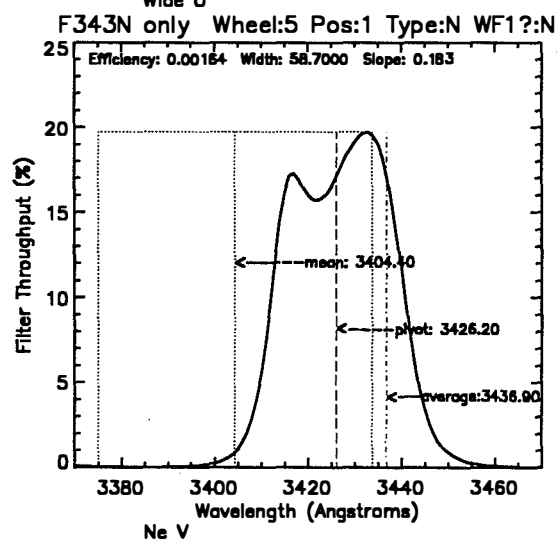
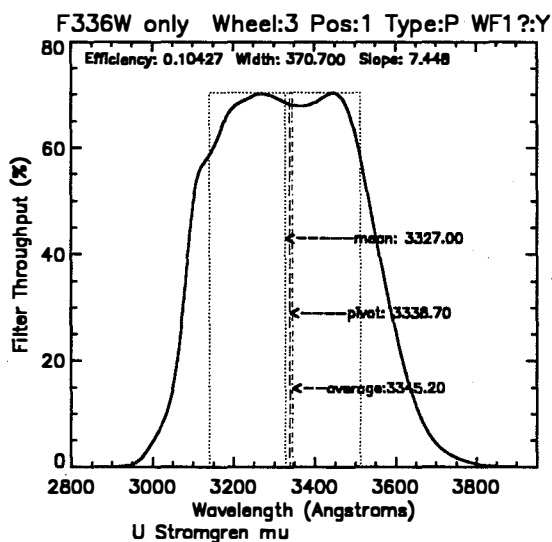
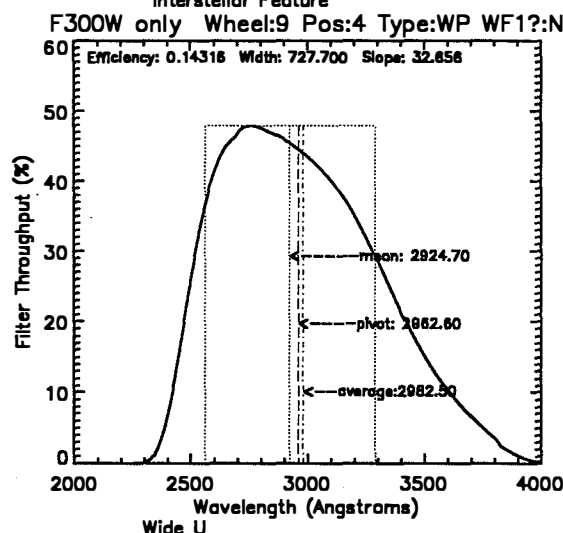
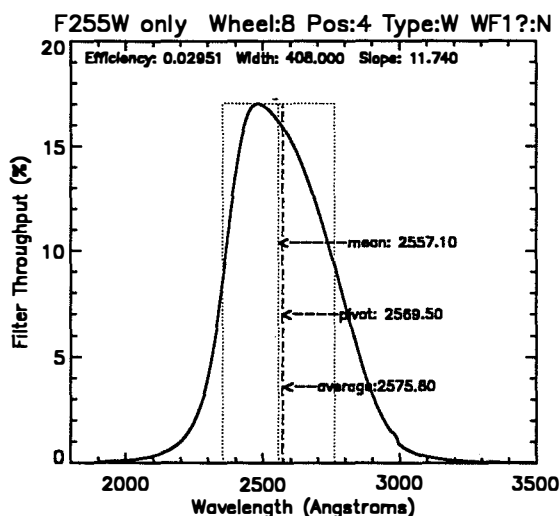
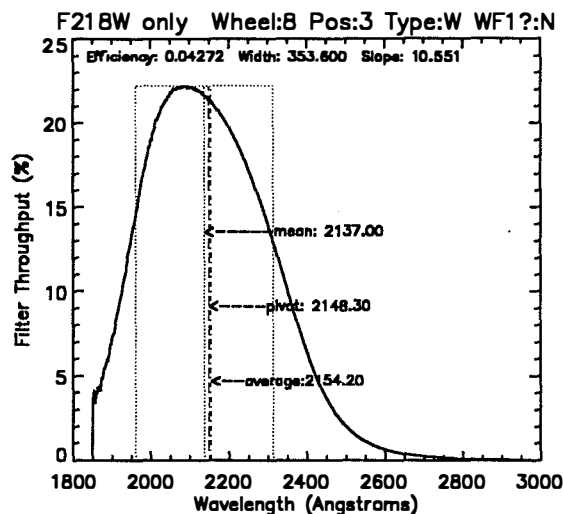
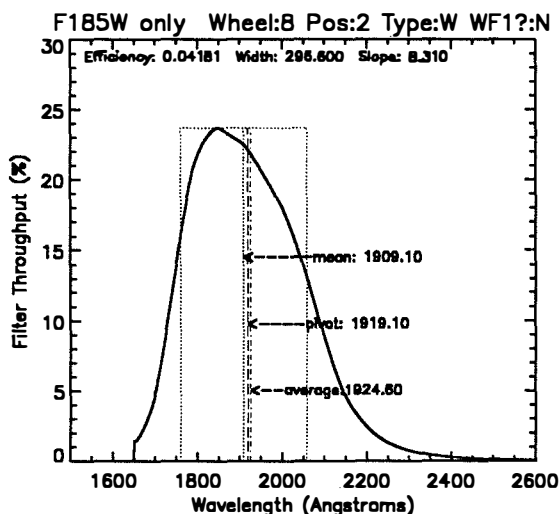
Further data reduction and analysis can be performed under the STScI's science data analysis software system (STSDAS). Standard routines are or will be available, operating under IRAF, for the analysis of data for image photometry, spectral analysis, astrometry, and the generation of the calibration data files.

8. APPENDIX

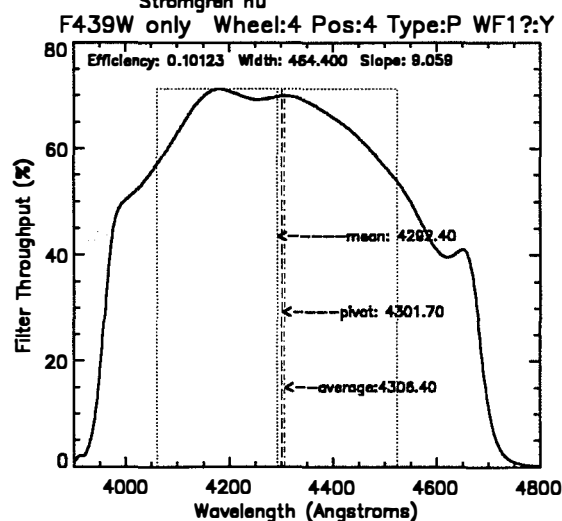
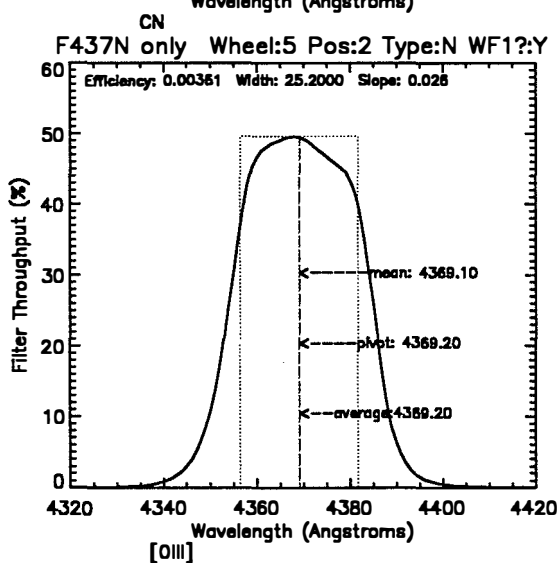
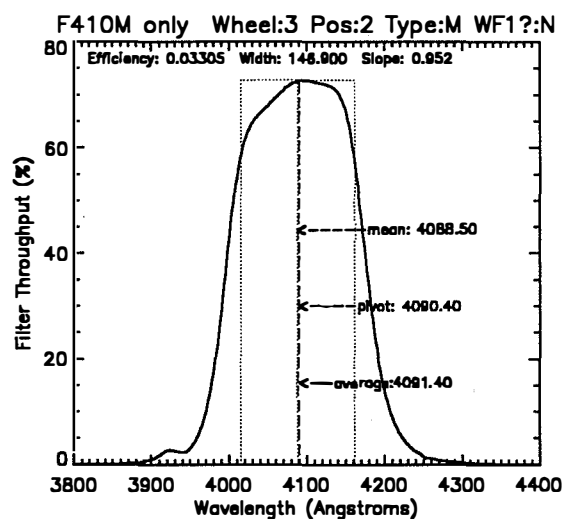
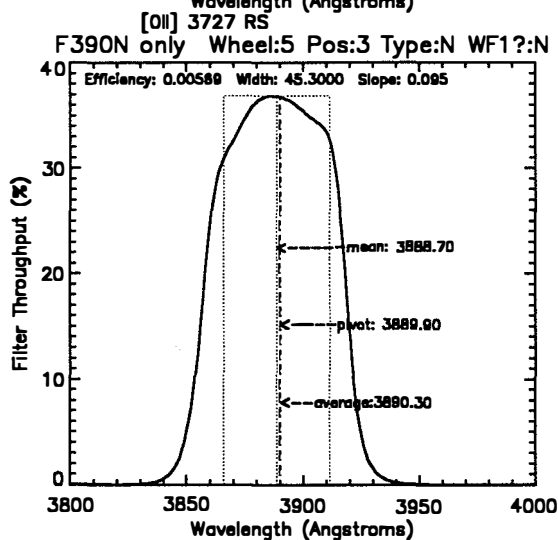
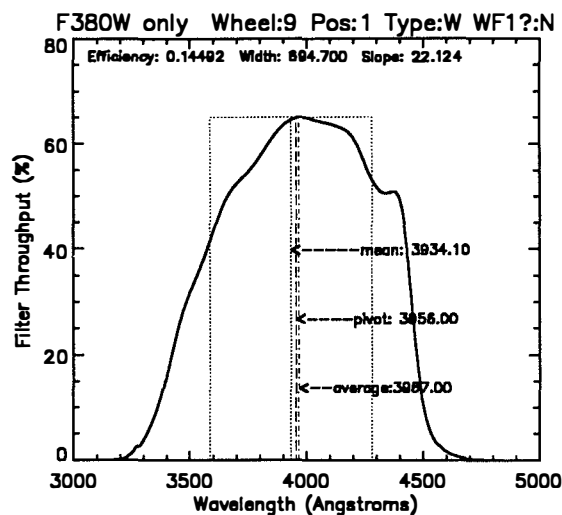
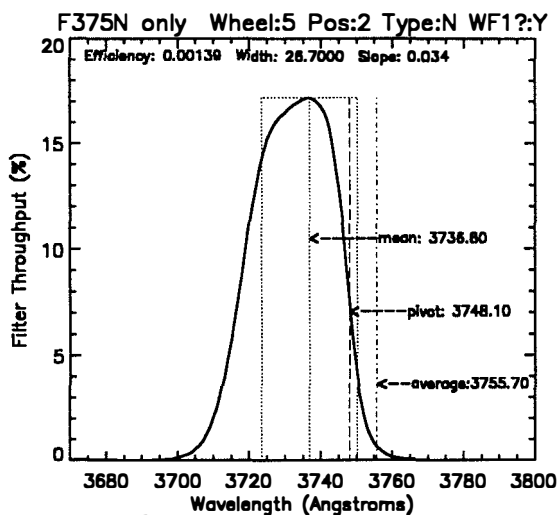
8.1. PASSBANDS FOR EACH FILTER IN ISOLATION



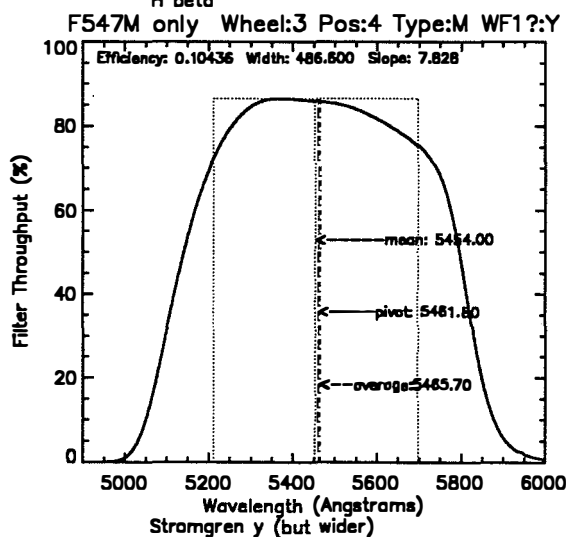
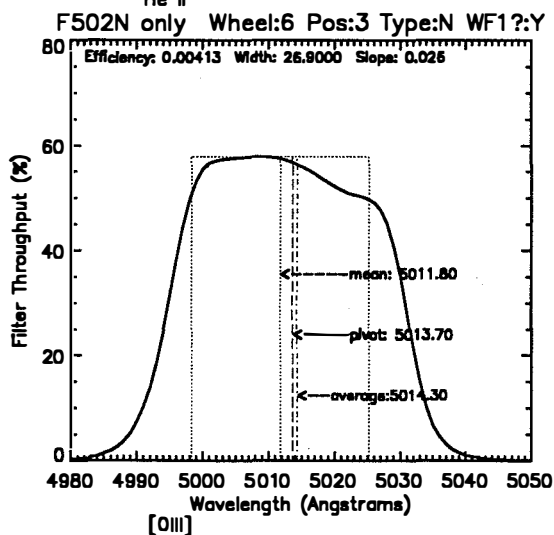
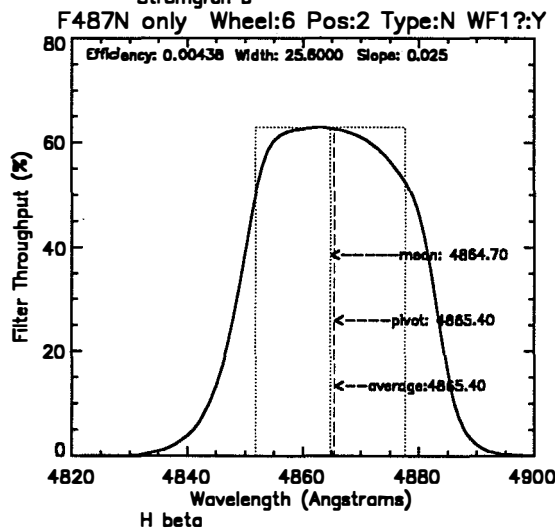
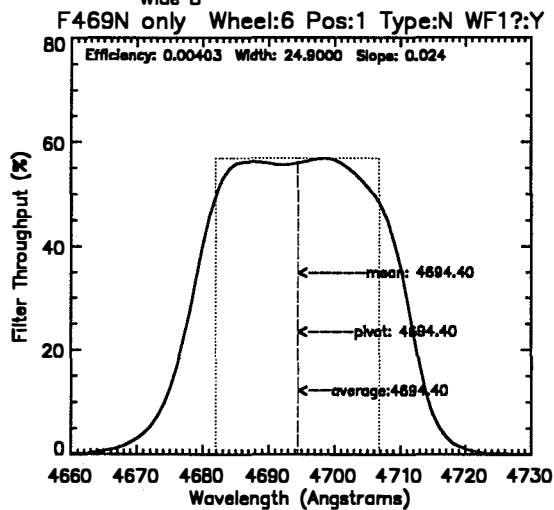
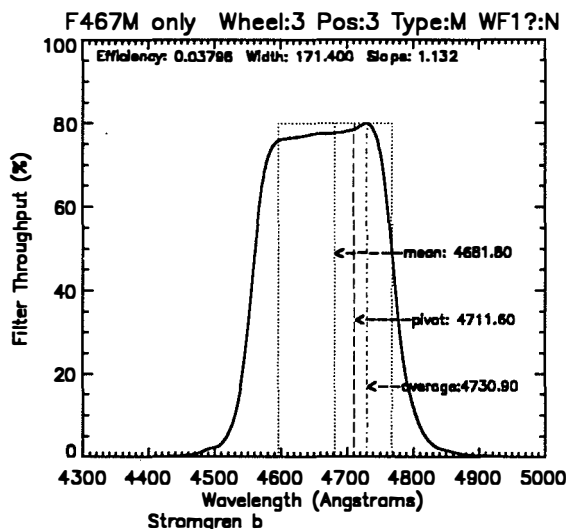
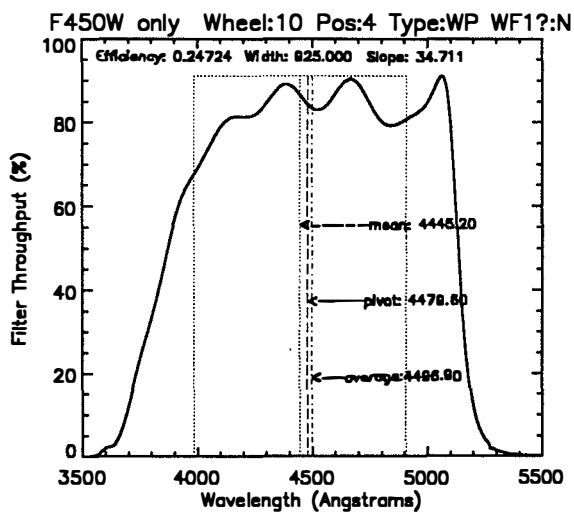
8.1 PASSBANDS FOR EACH FILTER IN ISOLATION (CONTINUED)



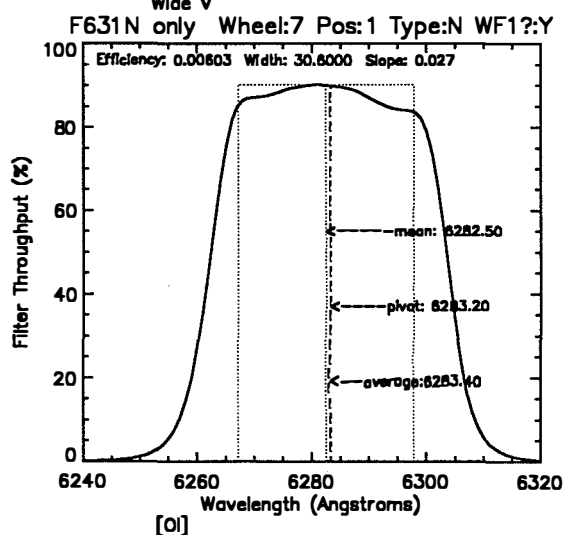
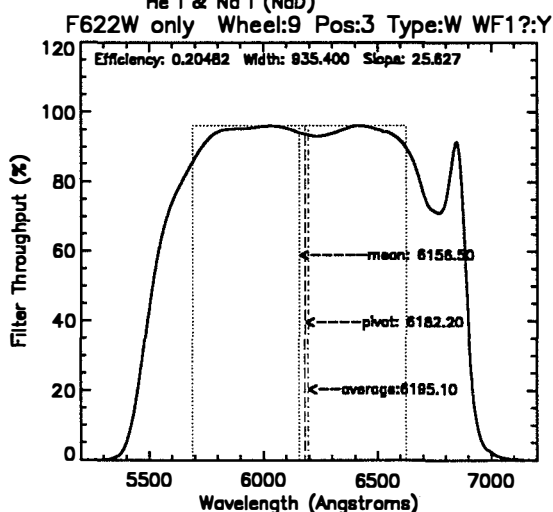
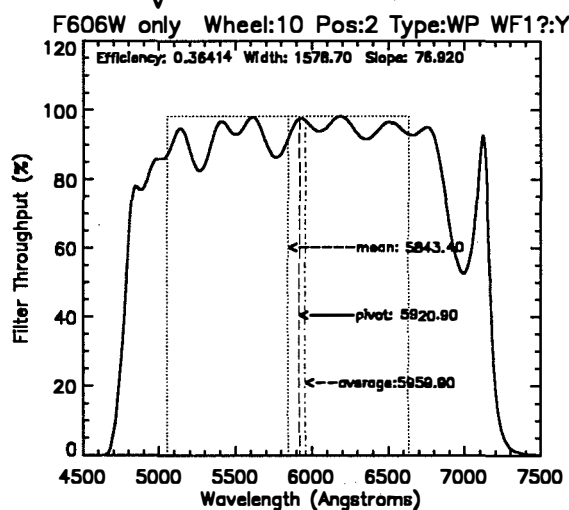
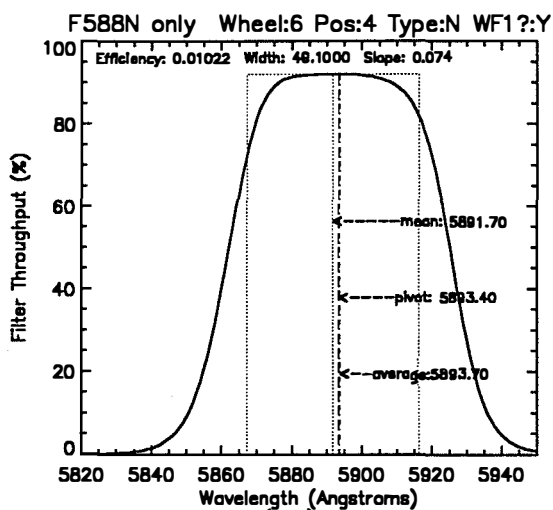
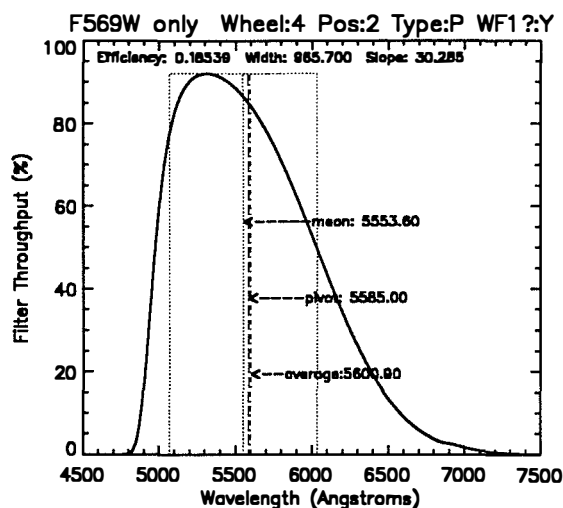
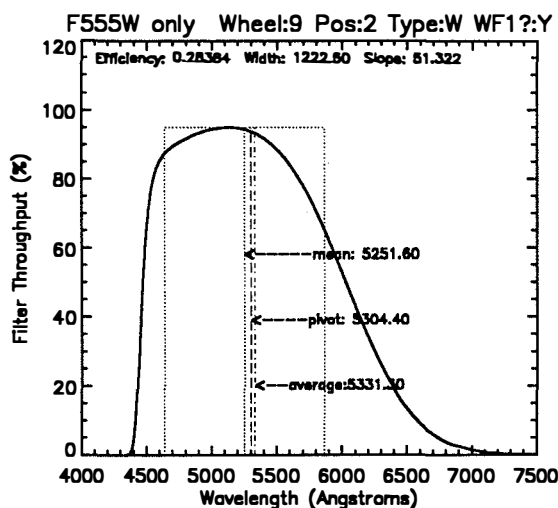
8.1 PASSBANDS FOR EACH FILTER IN ISOLATION (CONTINUED)



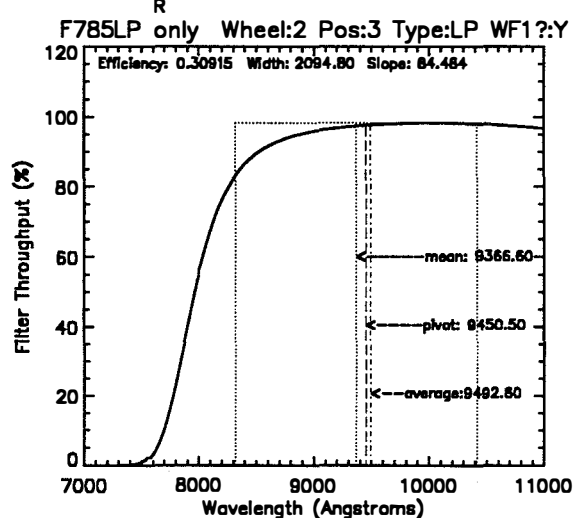
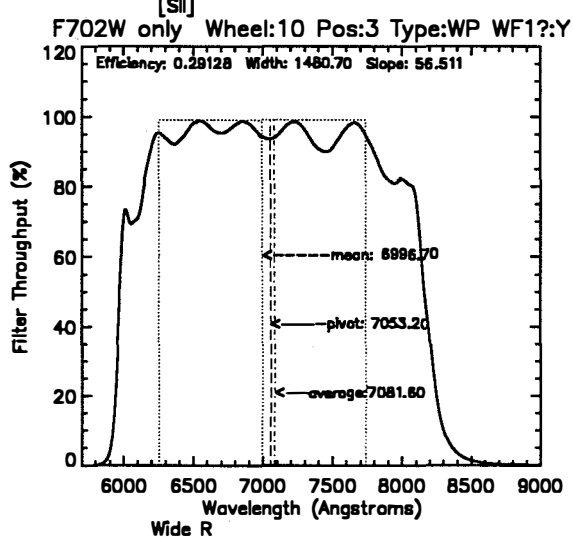
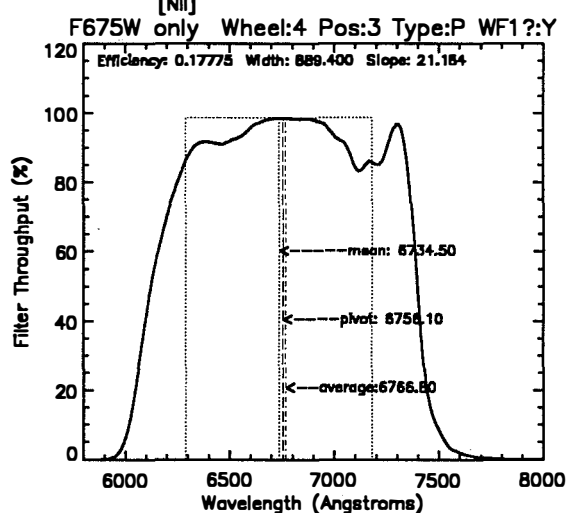
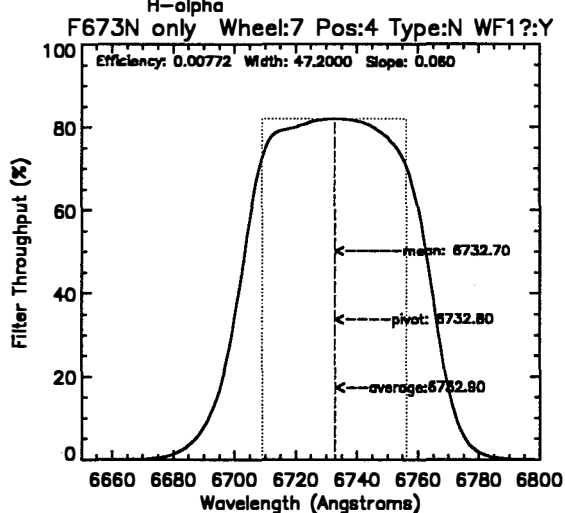
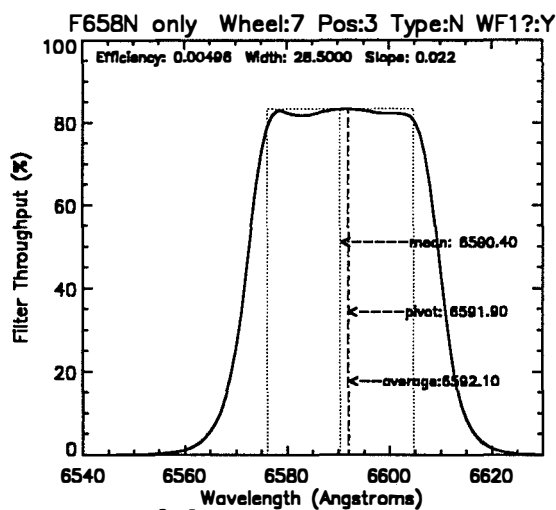
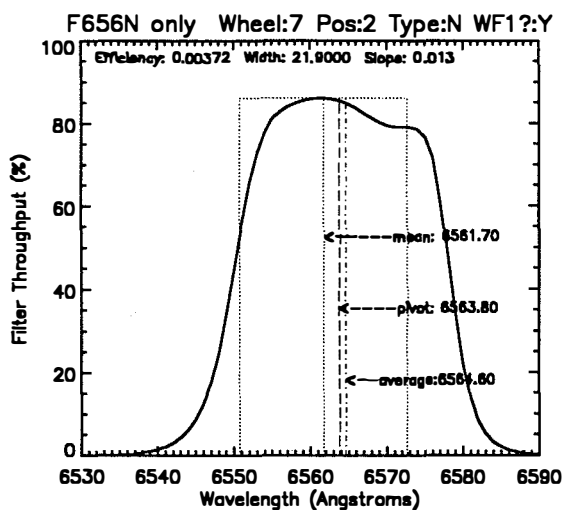
8.1 PASSBANDS FOR EACH FILTER IN ISOLATION (CONTINUED)



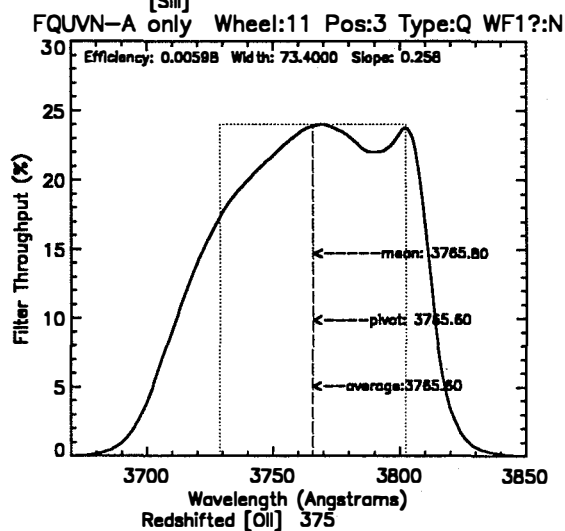
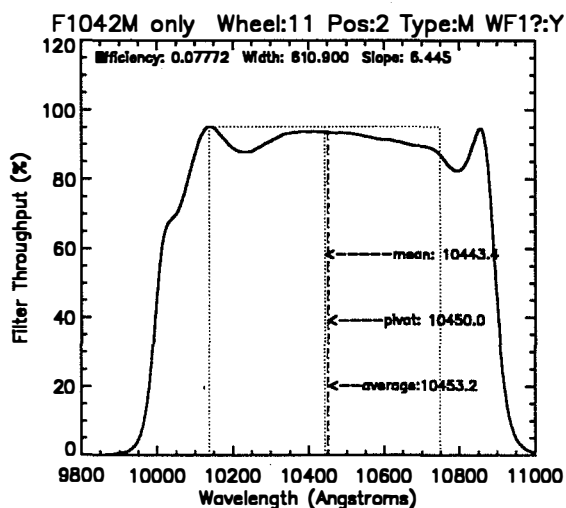
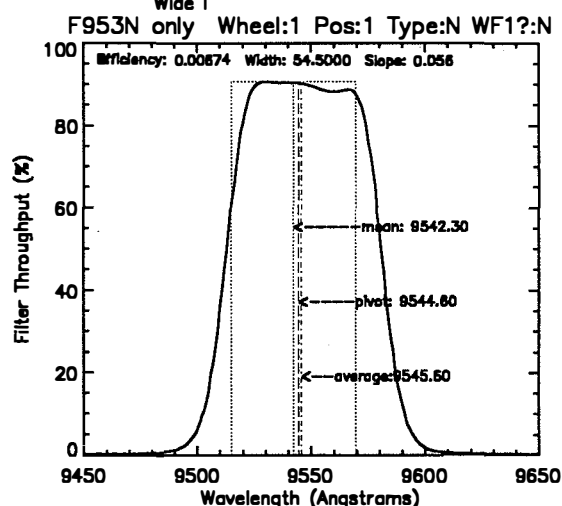
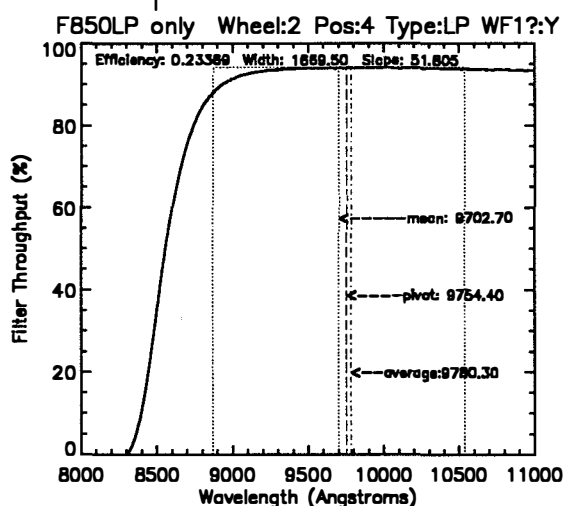
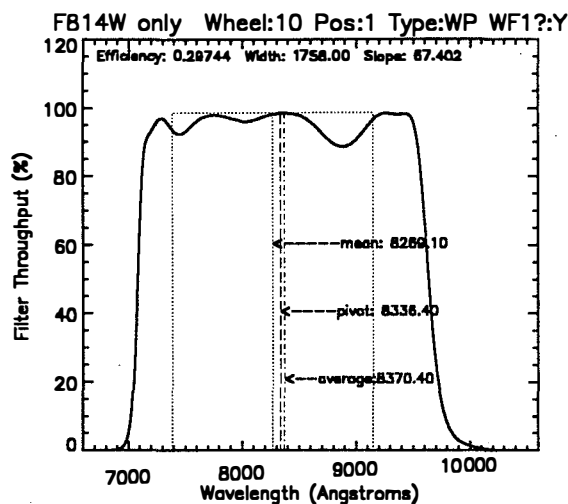
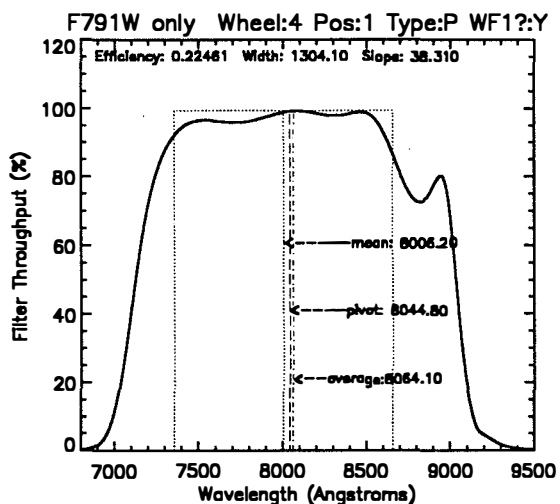
8.1 PASSBANDS FOR EACH FILTER IN ISOLATION (CONTINUED)



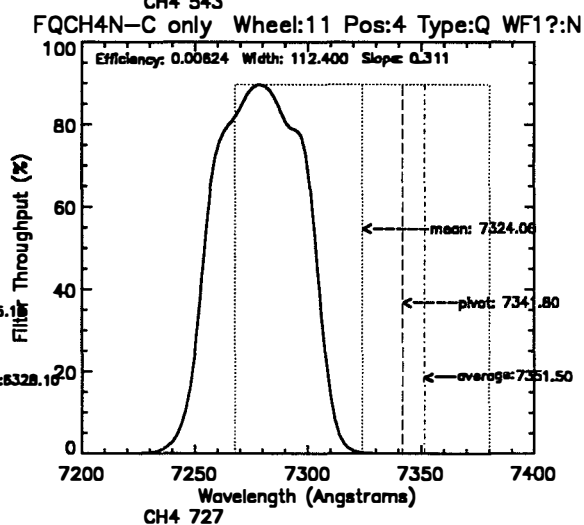
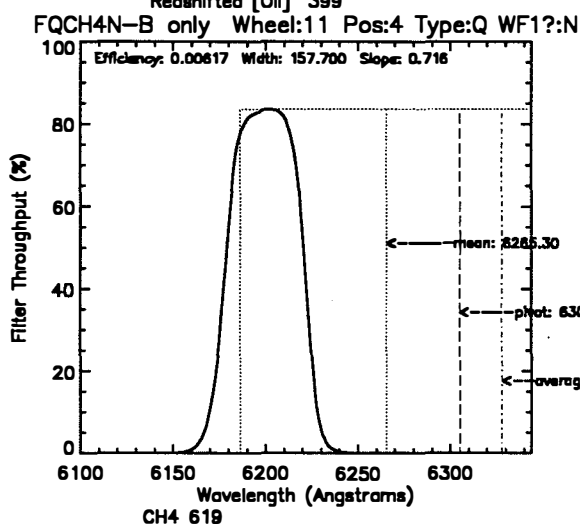
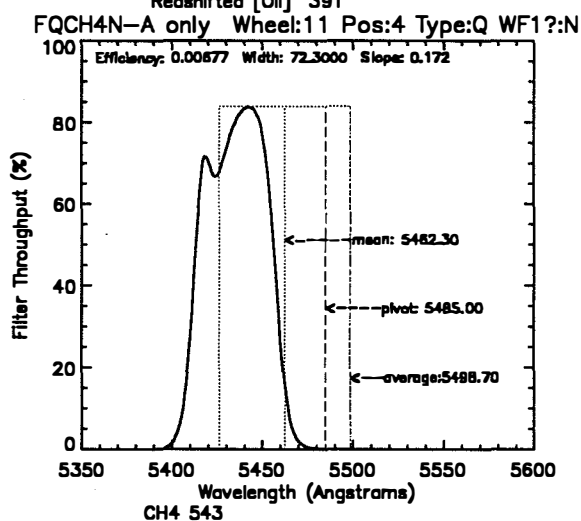
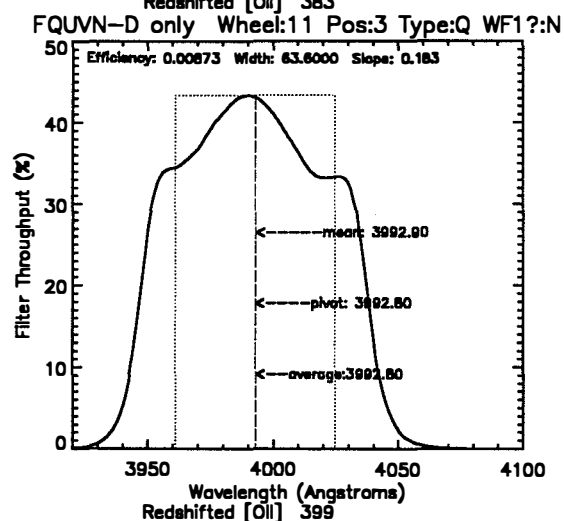
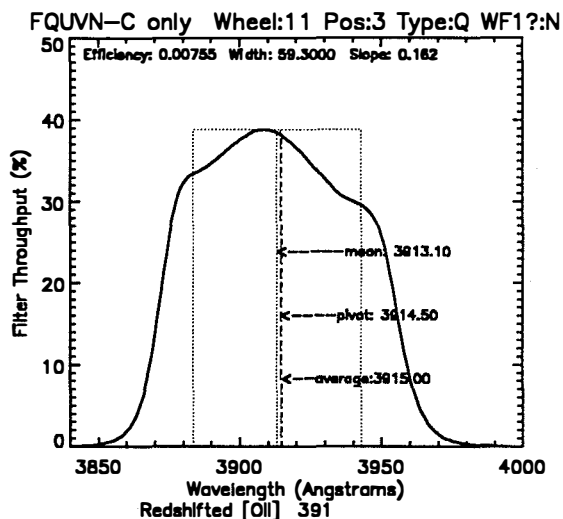
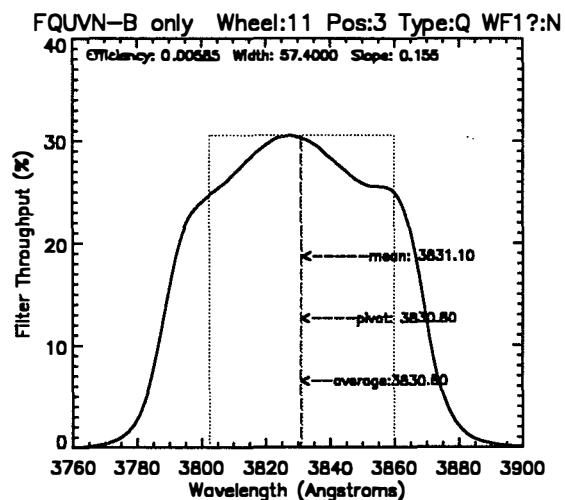
8.1 PASSBANDS FOR EACH FILTER IN ISOLATION (CONTINUED)



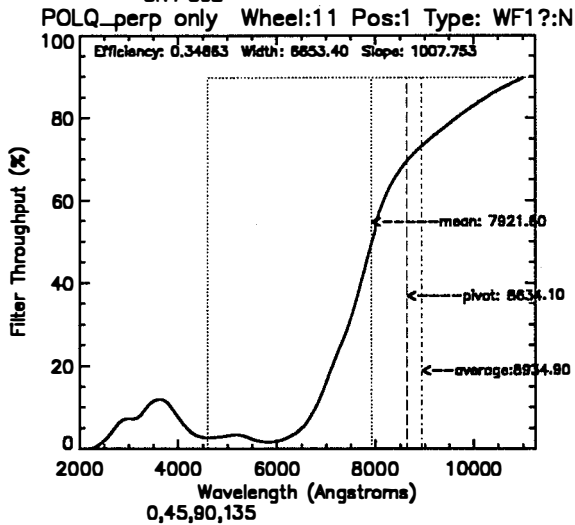
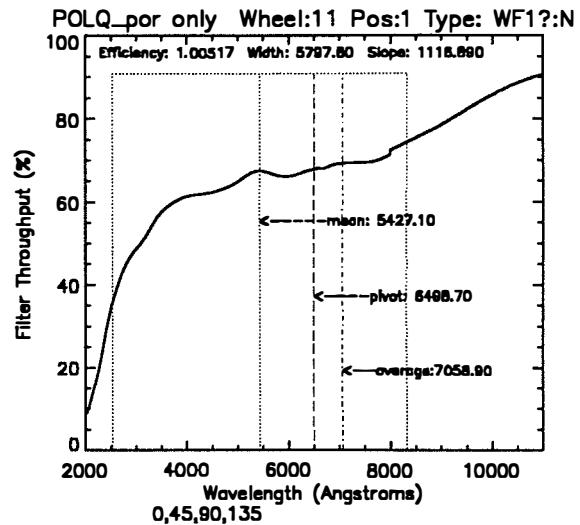
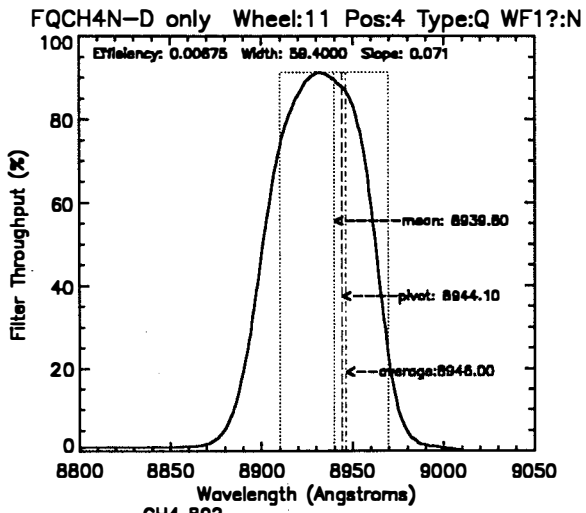
8.1 PASSBANDS FOR EACH FILTER IN ISOLATION (CONTINUED)



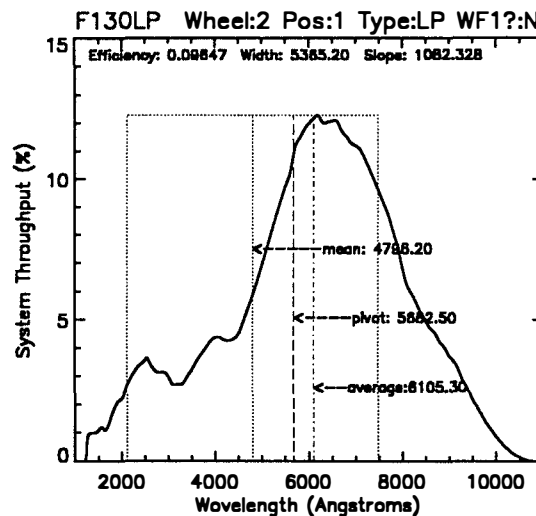
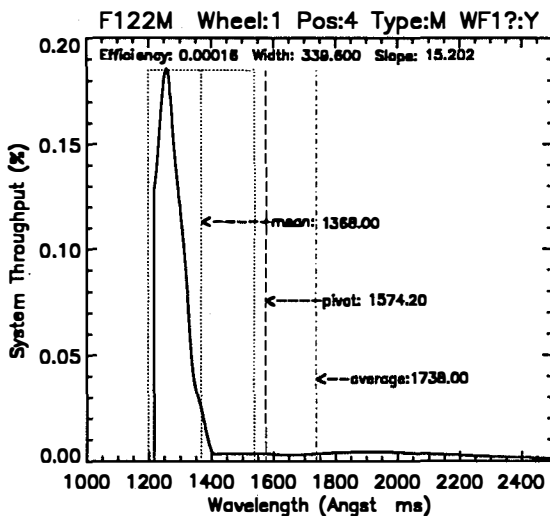
8.1 PASSBANDS FOR EACH FILTER IN ISOLATION (CONTINUED)



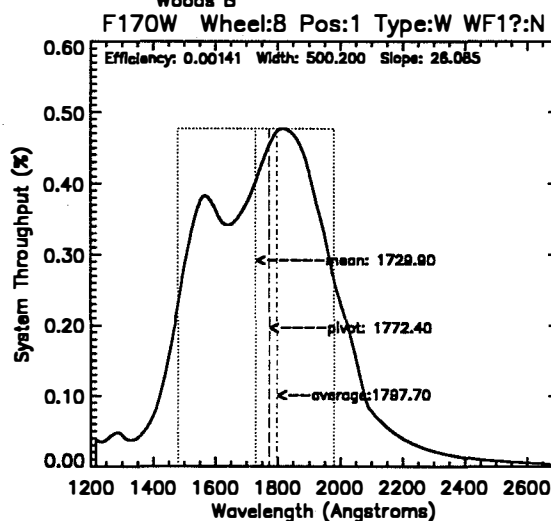
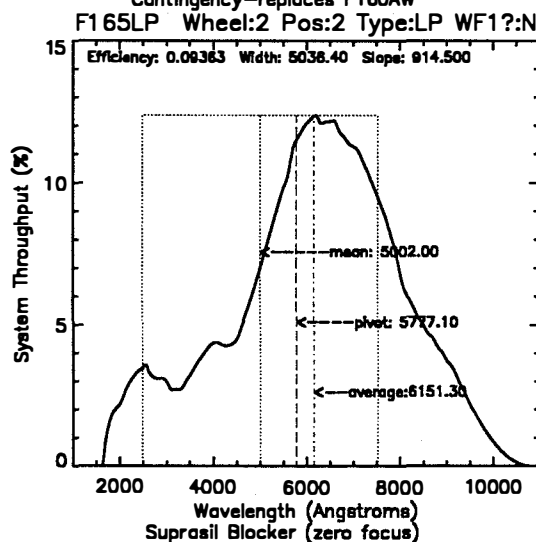
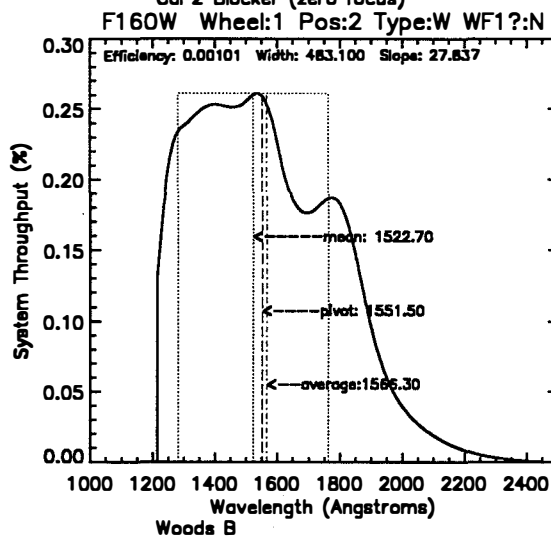
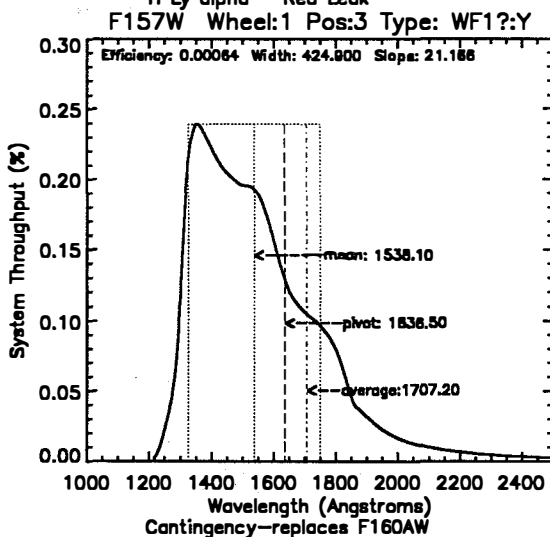
8.1 PASSBANDS FOR EACH FILTER IN ISOLATION (CONTINUED)



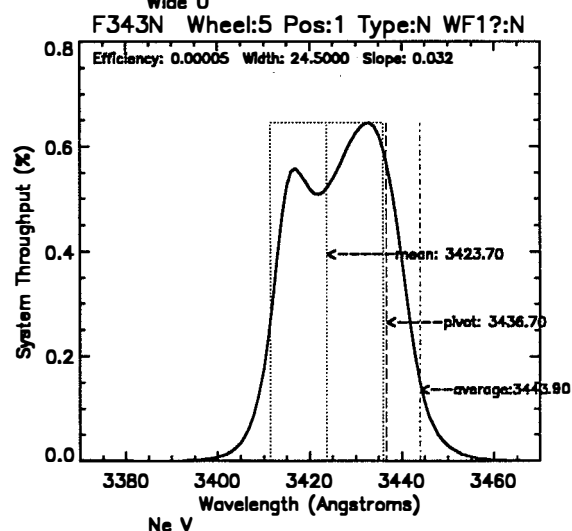
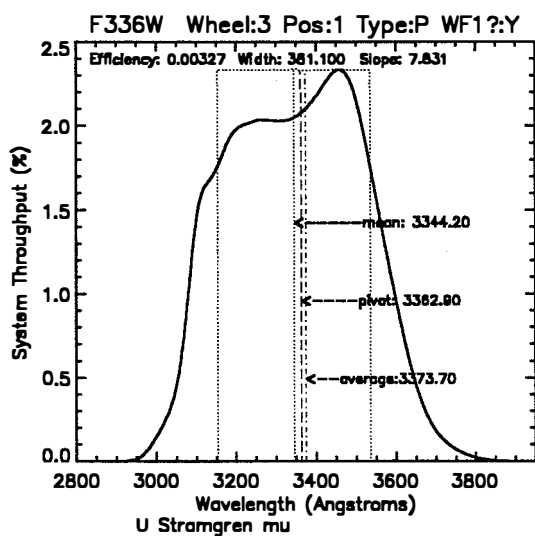
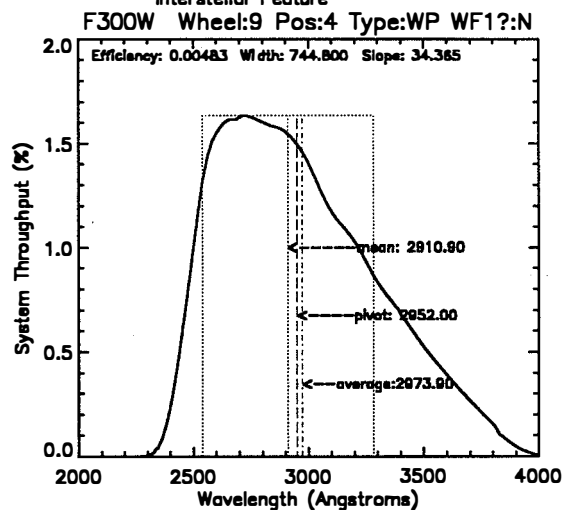
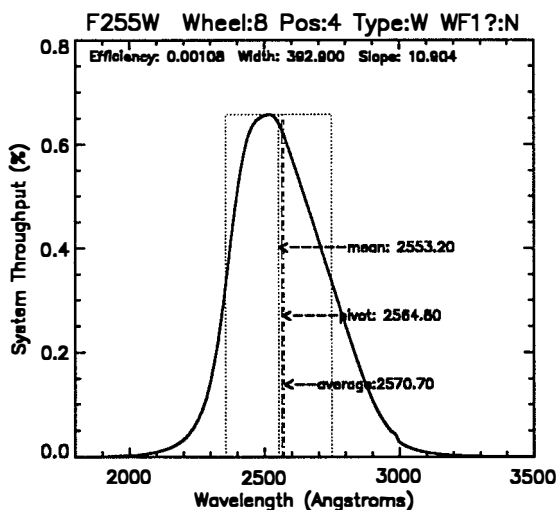
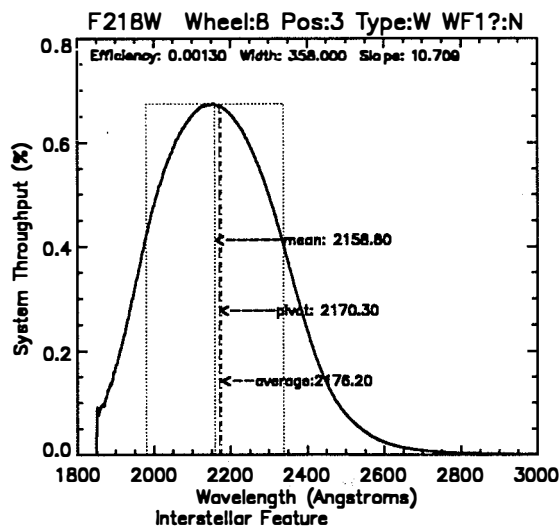
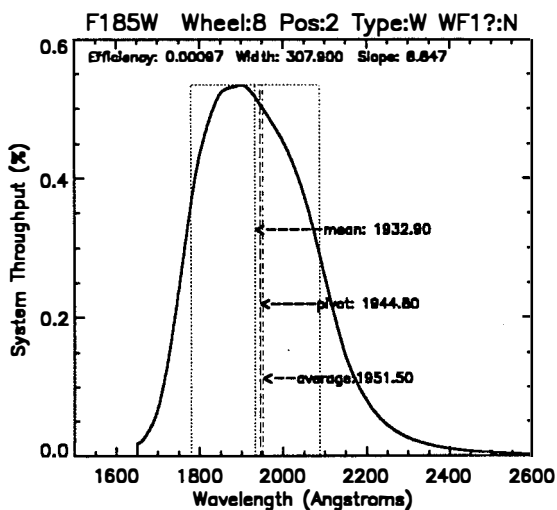
8.2. PASSBANDS INCLUDING THE SYSTEM RESPONSE



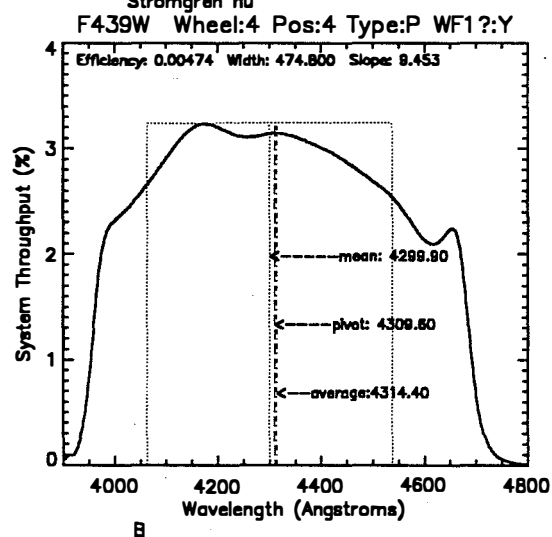
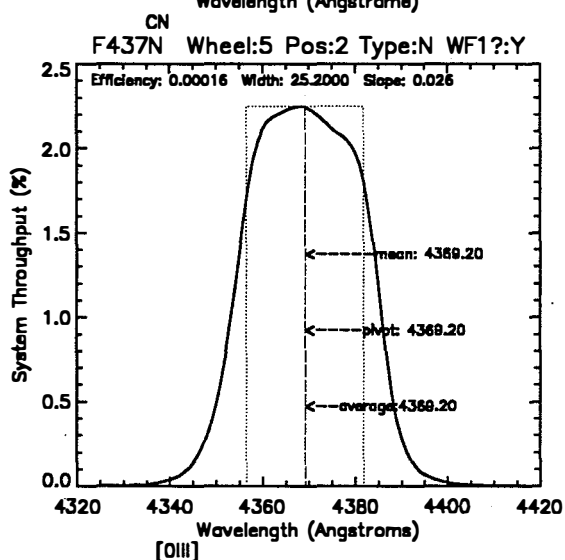
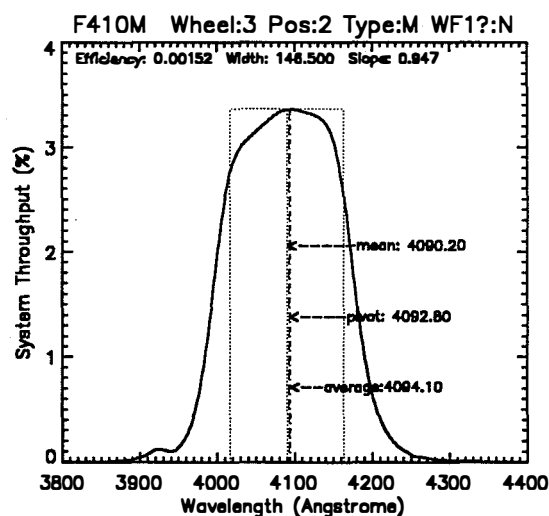
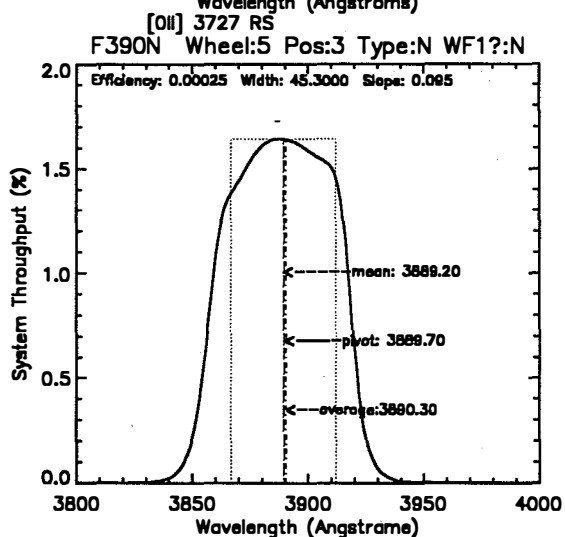
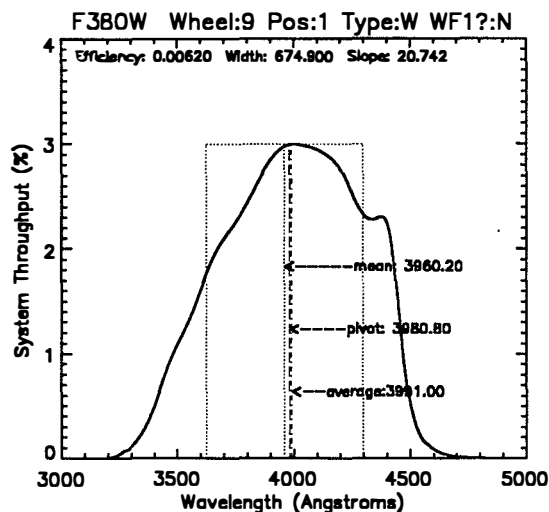
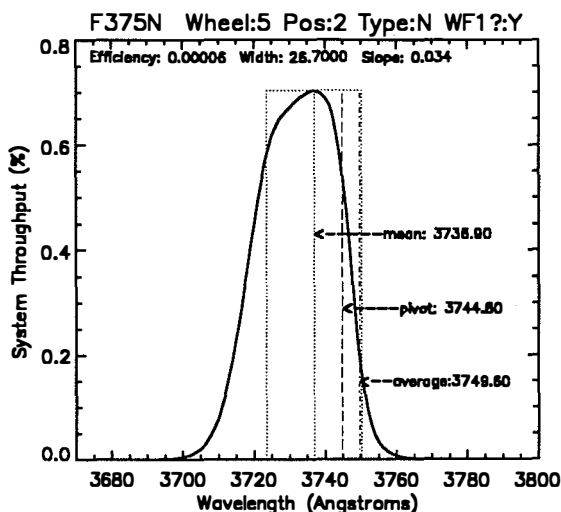
0.27
0.2679%
m m



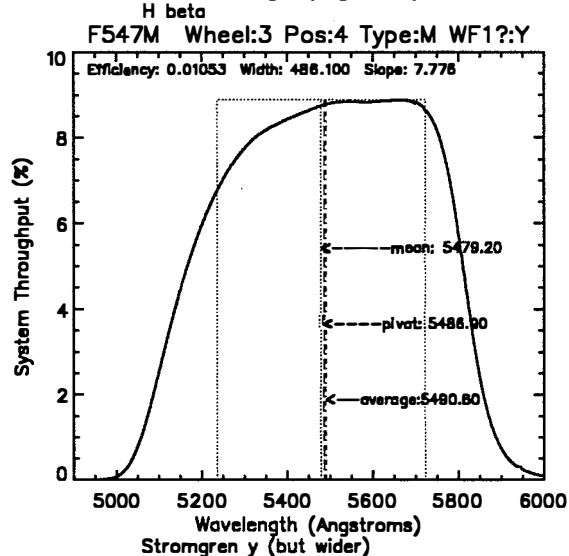
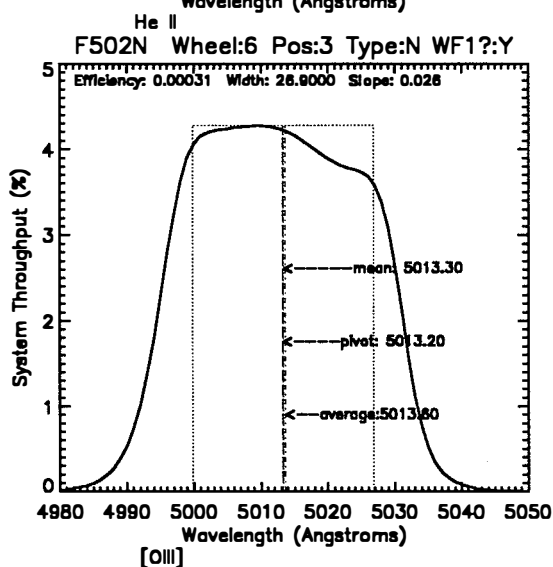
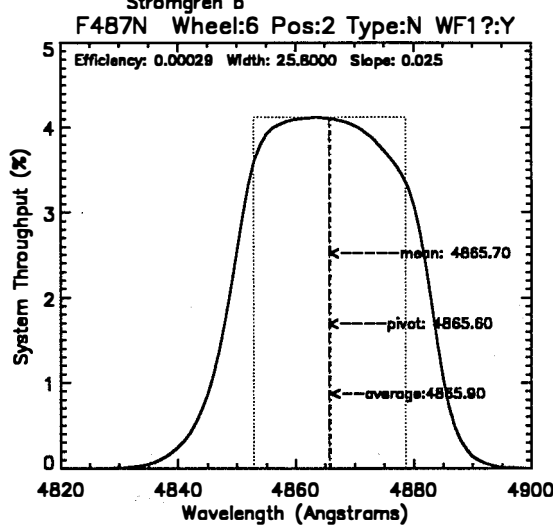
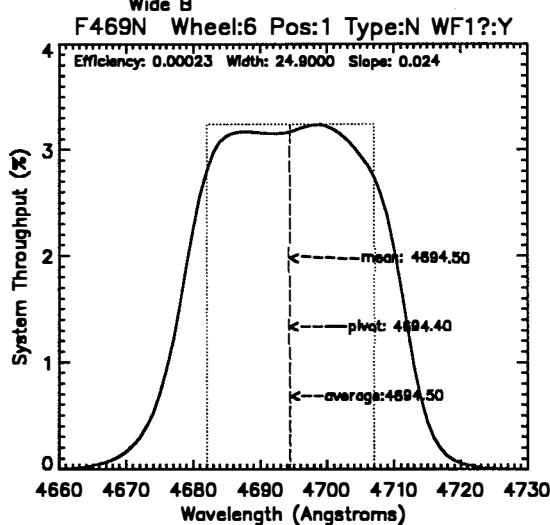
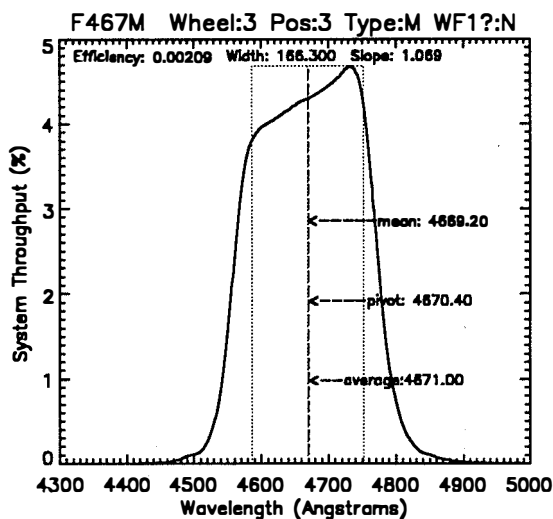
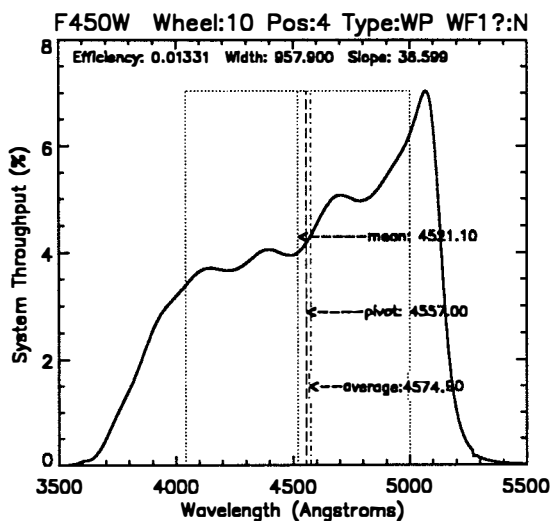
8.2 PASSBANDS INCLUDING THE SYSTEM RESPONSE (CONTINUED)



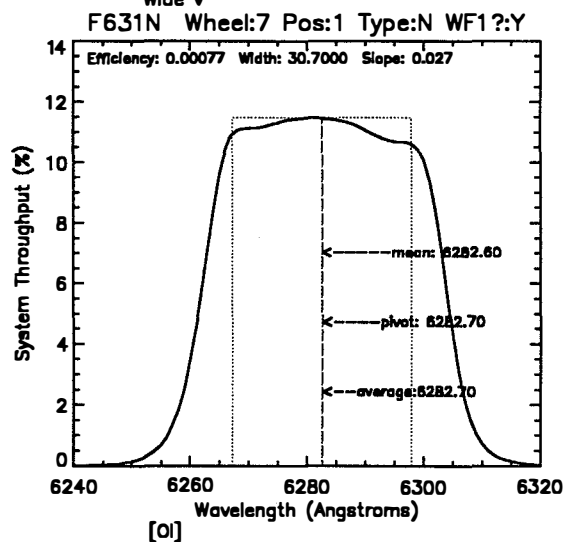
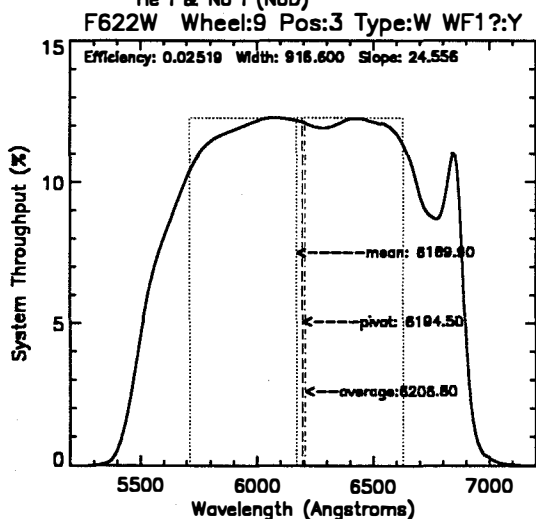
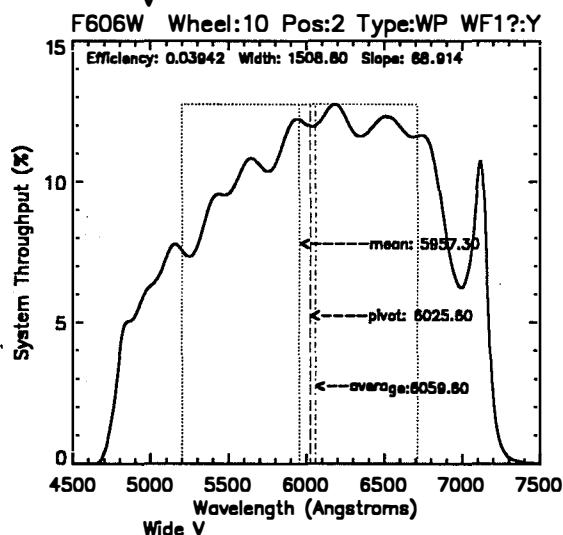
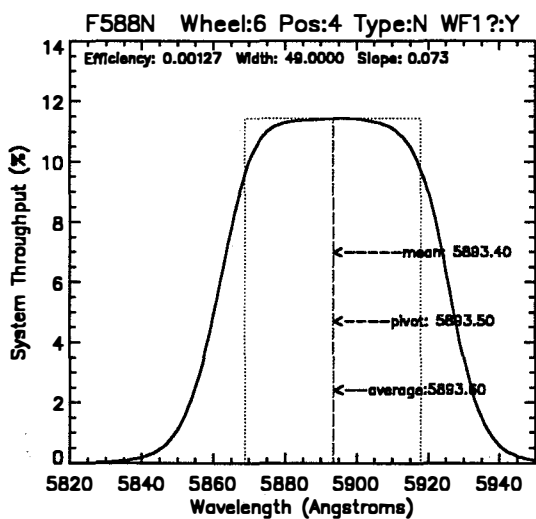
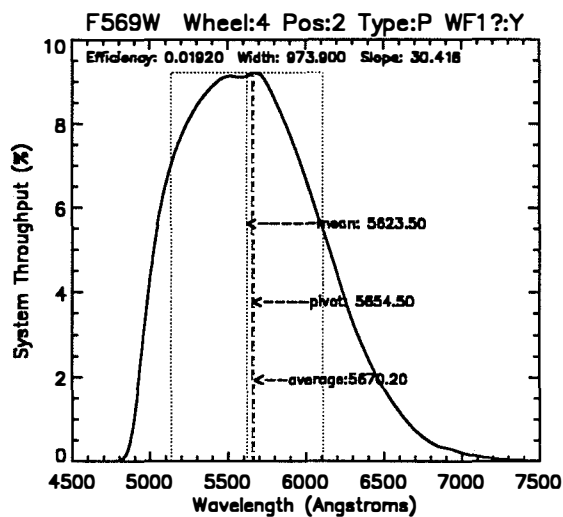
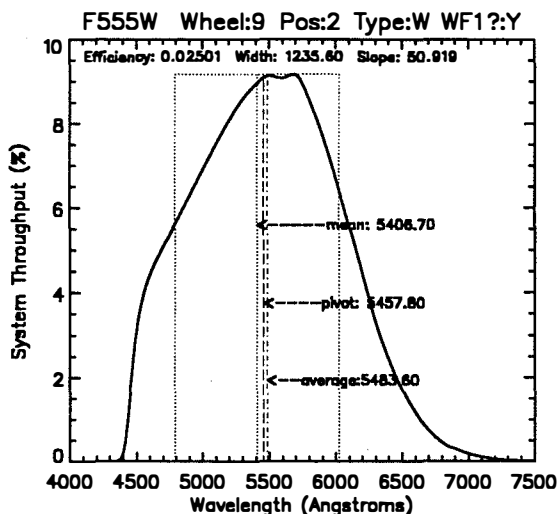
8.2 PASSBANDS INCLUDING THE SYSTEM RESPONSE (CONTINUED)



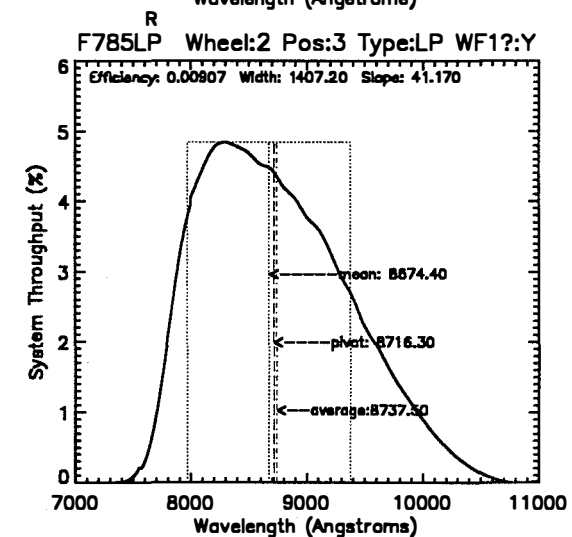
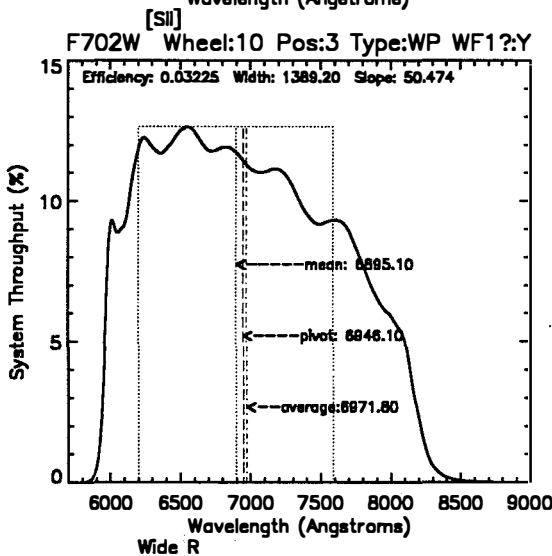
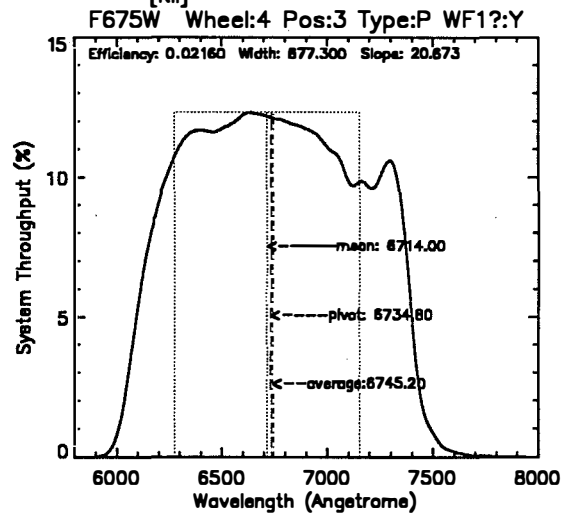
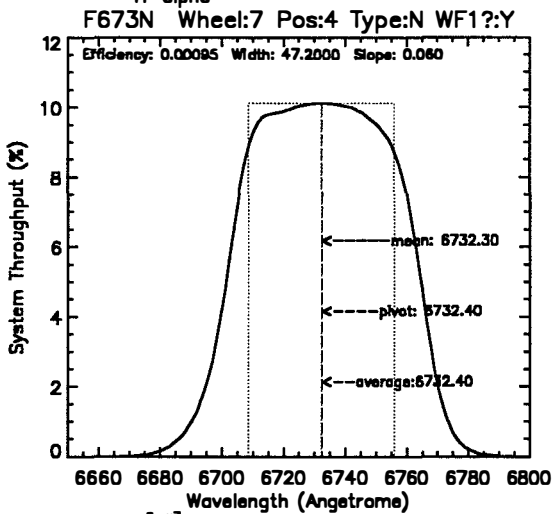
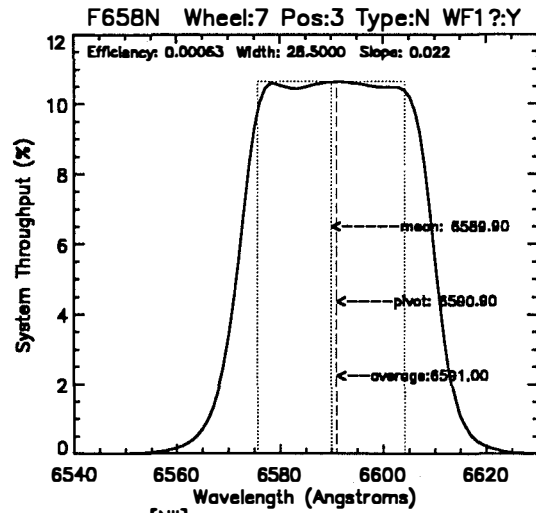
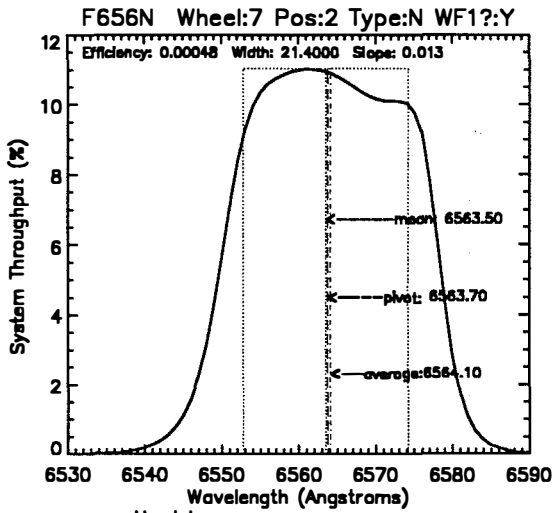
8.2 PASSBANDS INCLUDING THE SYSTEM RESPONSE (CONTINUED)



8.2 PASSBANDS INCLUDING THE SYSTEM RESPONSE (CONTINUED)

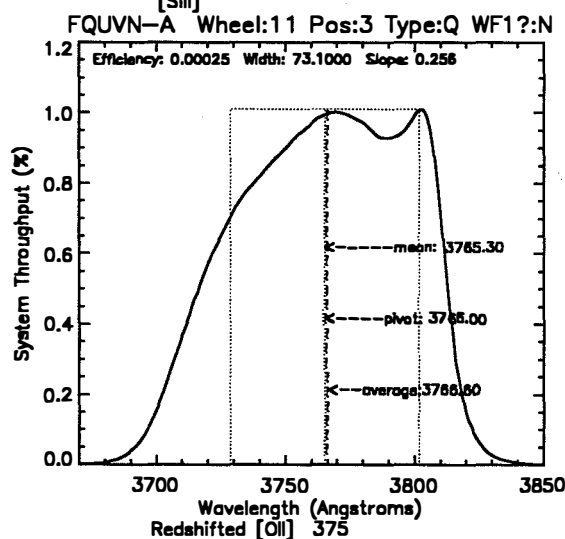
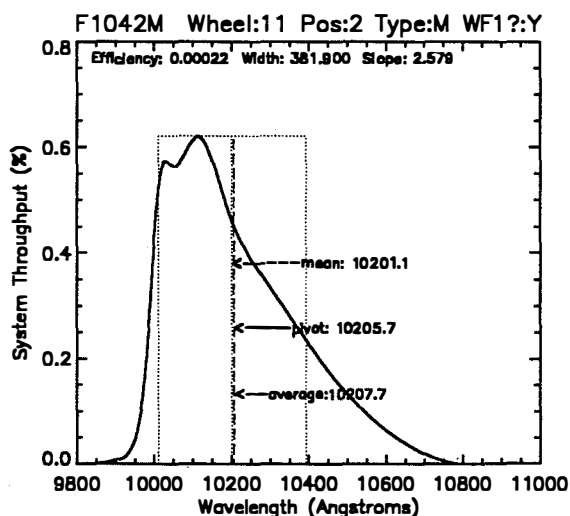
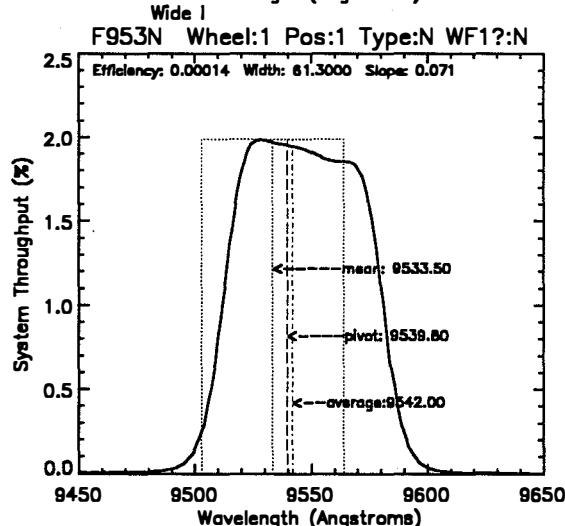
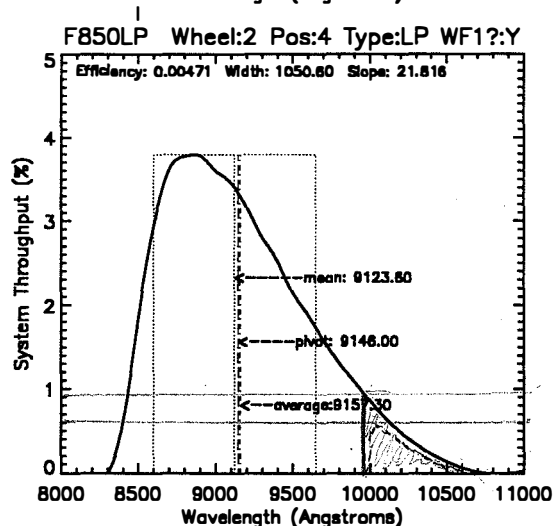
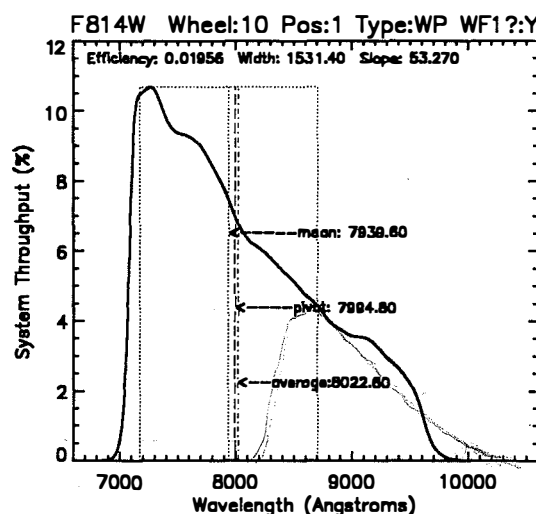
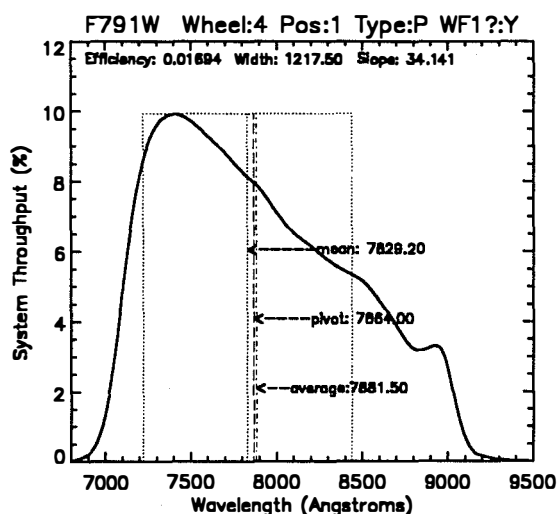


8.2 PASSBANDS INCLUDING THE SYSTEM RESPONSE (CONTINUED)

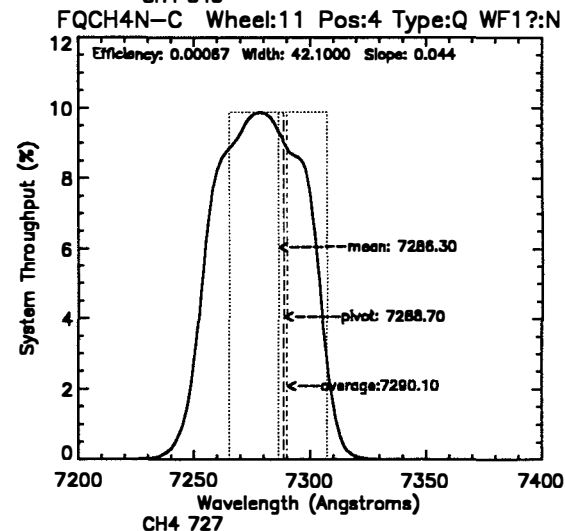
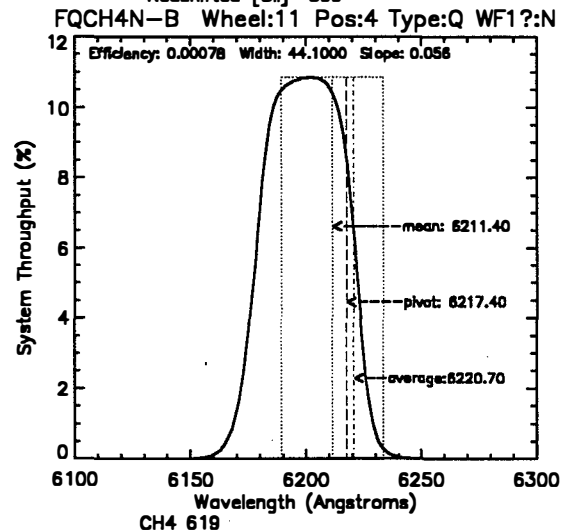
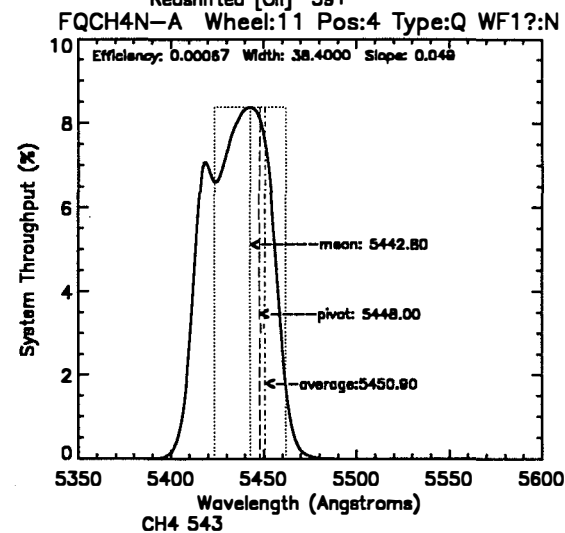
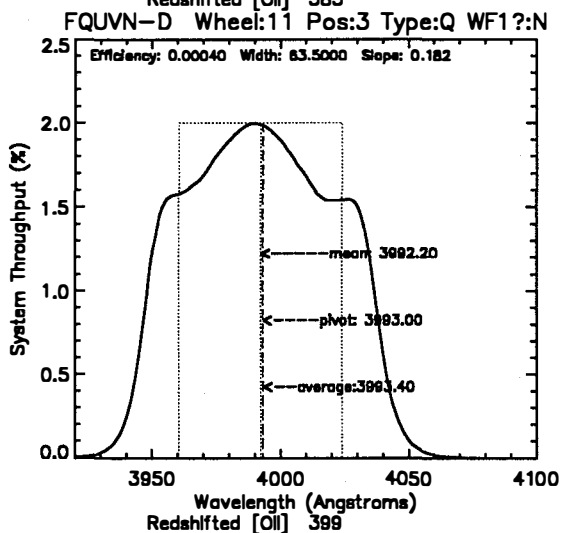
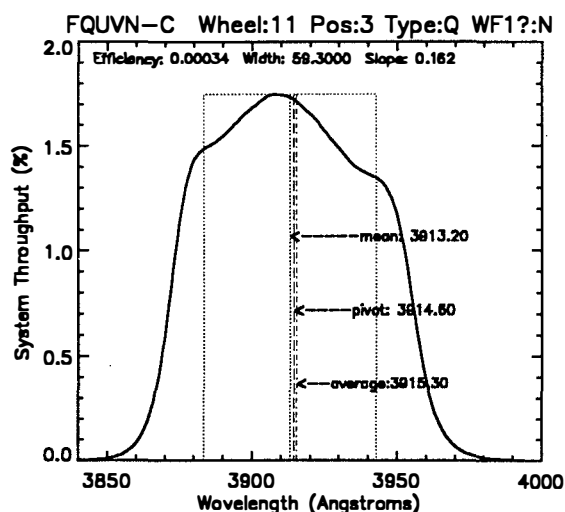
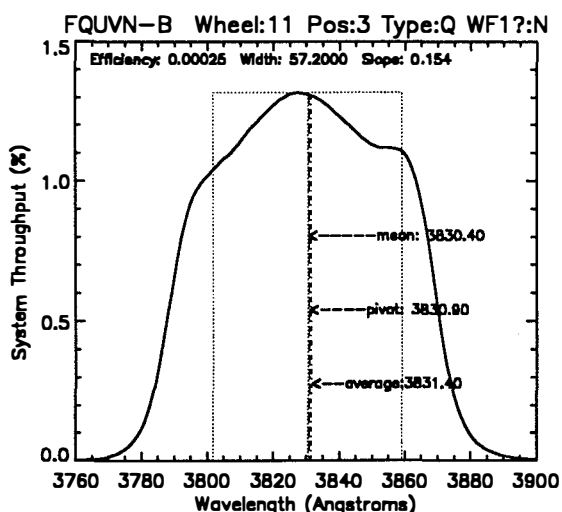


3000k → 1 μm peak

8.2 PASSBANDS INCLUDING THE SYSTEM RESPONSE (CONTINUED)



8.2 PASSBANDS INCLUDING THE SYSTEM RESPONSE (CONTINUED)



8.2 PASSBANDS INCLUDING THE SYSTEM RESPONSE (CONTINUED)

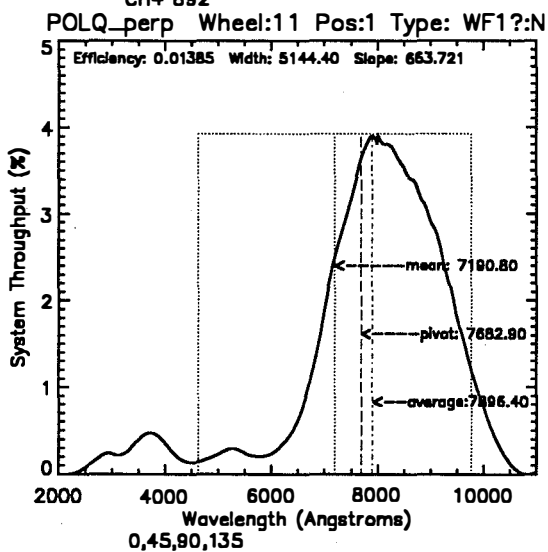
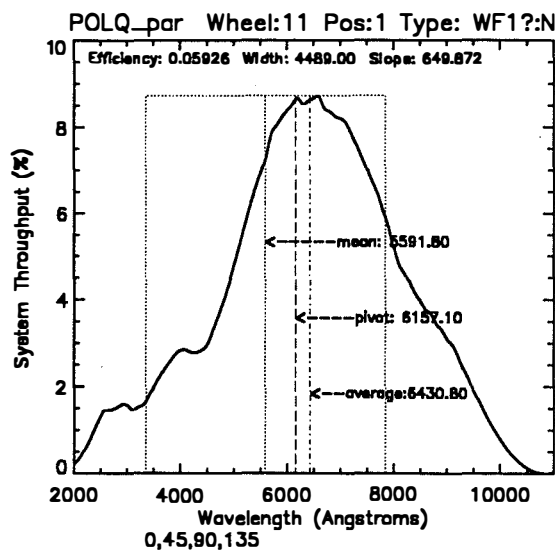
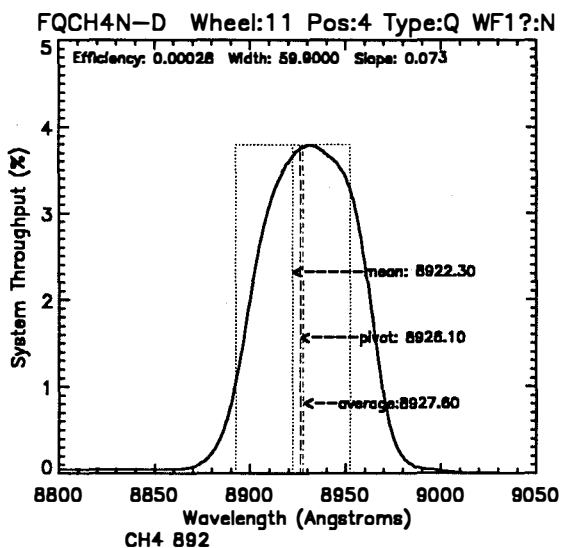


Figure 1 displays six panels showing the normalized system response versus wavelength (Angstroms) for various filter sets. The y-axis represents the Normalized Response (0 to 100), and the x-axis represents Wavelength (Angstroms) (1000 to 11000).

- Long Pass Filters + System Response:** Shows the response of long-pass filters. The legend includes F130, F160, F435, F438, F555, F606, F814, and F850.
- Wide Filters + System Response:** Shows the response of wide filters. The legend includes F130W, F160W, F435W, F438W, F555W, F606W, F814W, and F850W.
- Wide UBVRI Filters + System Response:** Shows the response of wide UBVRI filters. The legend includes F300W, F336W, F435W, F438W, F555W, F606W, F814W, and F850W.
- J-C UBVRI Filters + System Response:** Shows the response of J-C UBVRI filters. The legend includes F336W, F435W, F438W, F555W, F606W, F814W, and F850W.
- Medium Filters + System Response:** Shows the response of medium filters. The legend includes F122M, F438M, F555M, F606M, and F814M.
- Narrow Filters + System Response:** Shows the response of narrow filters. The legend includes F122N, F438N, F555N, F606N, F814N, F850N, F122M, F438M, F555M, F606M, and F814M.
- Quad Filters + System Response:** Shows the response of quad filters. The legend includes F122M, F438M, F555M, F606M, F814M, F122N, F438N, F555N, F606N, and F814N.

WFPC2 SIAF UPDATE

The WFPC2 aperture locations have been initially based on measurements taken with WFPC plus Thermal Vac ground measurements. Post SM images now provide some data for an update to the SIAF file in PDB.

We have used the fits supplied by the WFPC2 group which analyzed one chip at a time to establish the initial individual scales. The solution for chip 1 was very poor and we took a scale calculated separately by John Krist. We still found that the pyramid vertex did not align well. It should fall at the same V2V3 position on all chips but we found discrepancies of up to 8 arcsec.

We have generated an overall solution by forcing the pyramid vertex to be at a fixed V2V3 and assuming all four chips are aligned with each other. We have kept the relative chip-to-chip scales. The pyramid pixel positions on each chip were extracted from images by John Krist.

Pyramid Vertex			
	pixel x	pixel y	Scale
PC1	43	54	0.0455
WF2	47	23	0.099715
WF3	30	45	0.099544
WF4	41	47	0.099096

We have fitted 3 sets of data each corresponding to a complete chip set. Initially we avoided combining these sets so as not to introduce effects from variation of guide star positions within the FGSs. We obtained good fits with the 1st and 3rd sets, (RMS deviation 0.7 arcsec) but the second set which was in conjunction with the FOS observation gave a very poor result (RMS deviation 5 arcsec). We discarded the FOS set, and since the other two agreed so well, finally combined the data from sets 1 and 3.

The solution provides a new value for the WF3 scale while maintaining the inter-chip scale ratios fixed. The angle is measured from V3 to WF3 y-axis and the other chips are assumed to be at multiples of 90 degrees from this. For comparison, the principle results from the first, third and combined sets are given.